RICE UNIVERSITY

Infrared Spectroscopy of Graphene in Ultrahigh Magnetic Fields

by

Layla Goli Booshehri

A Thesis Submitted
in Partial Fulfillment of the
Requirements for the Degree

Doctor of Philosophy

Approved, Thesis Committee:

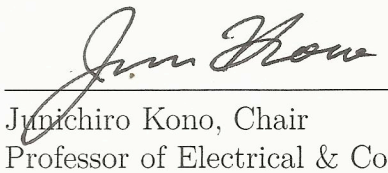

Junichiro Kono, Chair
Professor of Electrical & Computer Engineering and Physics & Astronomy

Emilia Morosan
Assistant Professor of Physics & Astronomy

Daniel M. Mittleman
Professor of Electrical & Computer Engineering

Charles H. Mielke
Ph.D., NHMFL-Pulsed Field Facility Director

Houston, Texas

April, 2012

ABSTRACT

Infrared Spectroscopy of Graphene in Ultrahigh Magnetic Fields

by

Layla Goli Booshehri

Graphene – a two-dimensional honeycomb lattice of sp^2-bonded carbon atoms – possesses unusual zero-gap band structure with linear band dispersions, accommodating photon-like, massless electrons that have exhibited a variety of surprising phenomena, primarily in DC transport, in the last several years. In this thesis dissertation, we investigate graphene's AC or infrared properties in the presence of an ultrahigh magnetic field, produced by a destructive pulsed method. The linear dispersions of graphene lead to unequally spaced Landau levels in a magnetic field, which we probe through cyclotron resonance (CR) spectroscopy in the *magnetic quantum limit*. Specifically, using magnetic fields up to 170 T and polarized midinfrared radiation with tunable wavelengths from 9.22 to 10.67 μm, we experimentally investigated CR in large-area graphene grown by chemical vapor deposition. Circular-polarization-dependent studies revealed strong p-type doping for as-grown graphene, and the dependence of the CR fields on the radiation wavelength allowed

for an accurate determination of the Fermi energy. Upon annealing the sample to remove physisorbed molecules, which shifts the Fermi energy closer to the Dirac point, we made the unusual observation that hole *and* electron CR emerges in the magnetic quantum limit, even though the sample is still p-type. We theoretically show that this non-intuitive phenomenon is a direct consequence of the unusual Landau level structure of graphene. Namely, if the Fermi energy lies in the $n = 0$ Landau level, then CR is present for both electron-active and hole-active circular polarizations. Furthermore, if the Fermi level lies in the $n = 0$ Landau level, the ratio of CR absorption between the electron-active and hole-active peaks allows one to accurately determine the Fermi level and carrier density. Hence, high-field CR studies allow not only for fundamental studies but also for characterization of large-area, low-mobility graphene samples.

Acknowledgments

This thesis dissertation is dedicated to my mother, my father, and my sister, for throughout my journey on this road less traveled, they have walked right by my side.

I recall my graduate school recruitment experience many years ago, and the struggle I faced in choosing a Ph.D. program solely on the basis of working for one particular advisor. Although the general consensus throughout recruitment was to strictly avoid such a singular decision, after meeting Professor Junichiro Kono, I happily walked down that proverbial road less traveled. And I can honestly say that I have never once looked back.

I would like to express my sincerest gratitude to my advisor, Professor Kono. His support and guidance these many years have left a deep impression not only on my academic career, but also on my life. He has allowed me to pursue academic adventures all across the world, which ultimately expanded my scientific and collaborative proficiency and greatly enhanced my worldview. I am grateful for his constant patience with both teaching me experimental physics and guiding me throughout the many projects that have led to the completion of my Ph.D. The knowledge I have gained from Professor Kono has truly been invaluable.

One of the most influential academic adventures I experienced during my Ph.D. was my extended visit to the National High Magnetic Field Laboratory in Los Alamos, NM. Here, I was fortunate to work under the mentorship of Dr. Charles (Chuck) Mielke, where I learned the subtle details of an extremely complicated and exciting Single-Turn Coil magnet system. I am grateful for the extensive amount of time Chuck spent personally working with me, even when his time constraints as deputy group leader made it practically impossible to do so. It was only through his patience and kindness that I successfully completed the experiments in this thesis dissertation.

I am also indebted to all the Kono group members that have made my graduate experience memorable. In particular, I would like to thank Dr. Thomas Searles and Dr. Darius Morris for truly welcoming me into the Kono group during the Applied Physics recruitment weekend, and since then, supported me throughout this journey with kindness and respect. To Dr. Chanjuan Sun, Dr. Yan Li, and Dr. Ji-hee Kim, who not only taught me a great deal of experimental and theoretical techniques, but did so with inspirational girl-power. Additionally, I would like to thank Dr. Lei Ren for providing my samples and Tim Noe for sharing an office, his awesome Igor-created movies of science, and his family photos with me. Finally, I am grateful to Erik Haróz for his friendship and sample expertise throughout the years.

Thank you to my committee members Professor Emilia Morosan, Professor Daniel Mittleman, and Dr. Charles Mielke, for serving on my defense committee and helping me arrange my defense with such an early notice. I would like to also express my

gratitude to Dr. Scott Crooker, Dr. Dwight Rickel, and Dr. Ross McDonald for their knowledge and expertise that aided my experiments at Los Alamos. For the theoretical portion of my work, I would like to thank Professor Christopher Stanton at the University of Florida.

Lastly, I am forever indebted to Ms. Sarah Phillips, Ms. Julie Gallegos, and Ms. Angie Willow for always helping me no matter the request and for their never-ending support. They have truly been like family to me.

Contents

Illustrations

Tables

Chapter 1

Introduction

Graphene, a monolayer of carbon atoms arranged in a two-dimensional (2D) honeycomb lattice, has earned considerable attention for its unusual band structure and corresponding electronic properties. Unlike conventional two-dimensional electron gas (2DEG) systems such as GaAs 2DEGs, the band structure of graphene exhibits a zero-gap linear dispersion relation near each of the Dirac points, where the conduction and valence bands touch at the six corners of the hexagon-shaped Brilliouin zone [1]. In the vicinity of the Dirac points, the electron energy E depends linearly on its momentum $\hbar|\boldsymbol{k}|$,

$$E(\boldsymbol{k}) = v_F \hbar |\boldsymbol{k}| \tag{1.1}$$

and as a result, the free charge carriers in graphene are not governed by Schrödinger's equation, but by Dirac's equation for zero rest mass particles, where the speed of light is replaced with the effective velocity, $v_F \approx 10^6\,\mathrm{m/s}$ [2]. Furthermore, when a perpendicular magnetic field (B) is applied, the linear energy dispersion forms unequally spaced Landau levels (LL), given by

$$E = \mathrm{sgn}(n) v_F \sqrt{2\hbar |e| B |n|}, \tag{1.2}$$

which have a $\sqrt{B}$ dependence and an $n = 0$ LL with $E = 0$ regardless of magnetic field and a distinctive electron-hole degeneracy, which differs greatly from the equally

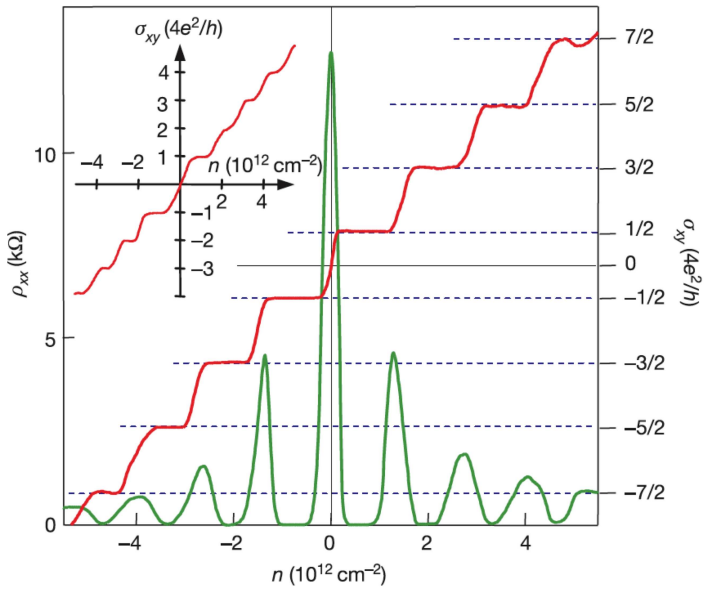

Figure 1.1 : Hall conductivity σ_{xy} and longitudinal resistivity ρ_{xy} of graphene as a function of concentration for B=14 T and T=4 K. Inset shows σ_{xy} of bilayer graphene for comparison. Bilayer graphene exhibits normal quantization sequence unlike monolayer graphene. [3]

spaced LLs of GaAs 2DEGs.

From the 2D Dirac nature of graphene, a variety of novel transport phenomena have been predicted and observed [3–6]. Figure 1.1 shows the anomalous quantum Hall effect (QHE) for massless Dirac fermions in graphene, where the Hall conductivity σ_{xy} and longitudinal resistivity ρ_{xy} are plotted as a function of electron and hole concentrations in $B = 14\,\mathrm{T}$ and temperature $T = 4\,\mathrm{K}$ [3]. The pronounced plateaus do not occur in the expected $\sigma_{xy} = (4e^2/h)N$ sequence (where N is an integer), and instead, correspond to half-integer ν that occurs at $(4e^2/h)(N + 1/2)$. This effect is a direct result of massless Dirac fermions in graphene, where the $n = 0$ LL exhibits an electron-hole degeneracy. In particular, the degeneracy of the $n = 0$ LL is shared

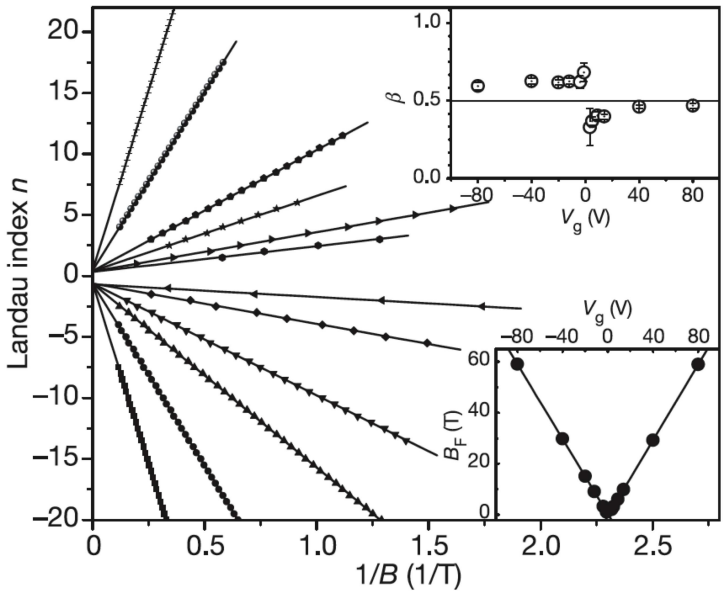

Figure 1.2 : A fan diagram for SdH oscillations at different gate voltages. The lines correspond to a linear fit where the slope indicates the frequency of the SdH oscillation, B_F shown in the lower inset and the n-axis intercept provides the Berry phase (upper inset) [4].

equally by both electron and hole carriers, which is unlike other Landau levels in graphene. Therefore, only the first Hall plateau occurs at half the normal filling, which shifts the standard sequence by 1/2 and results in the half-integer QHE with filling factor of $\nu = \pm 2, \pm 6, \pm 10, \ldots$ [3, 4, 7–9].

The electron-hole degeneracy of the $n = 0$ LL also explains the existence of the non-zero Berry phase (π) of Shubnikov-de Haas (SdH) oscillations [3, 4]. In Figure 1.2, a fan diagram of the SdH oscillations at different gate voltages shows a linear fit to the data with an n-axis intercept that directly yields Berry's phase [4]. Moreover, in strong magnetic fields up to 45 T, the half-integer QHE filling factor changes to $\nu = 0, \pm 1, \pm 2, \pm 4, \ldots$, as shown in Figure 1.3, where the presence of the

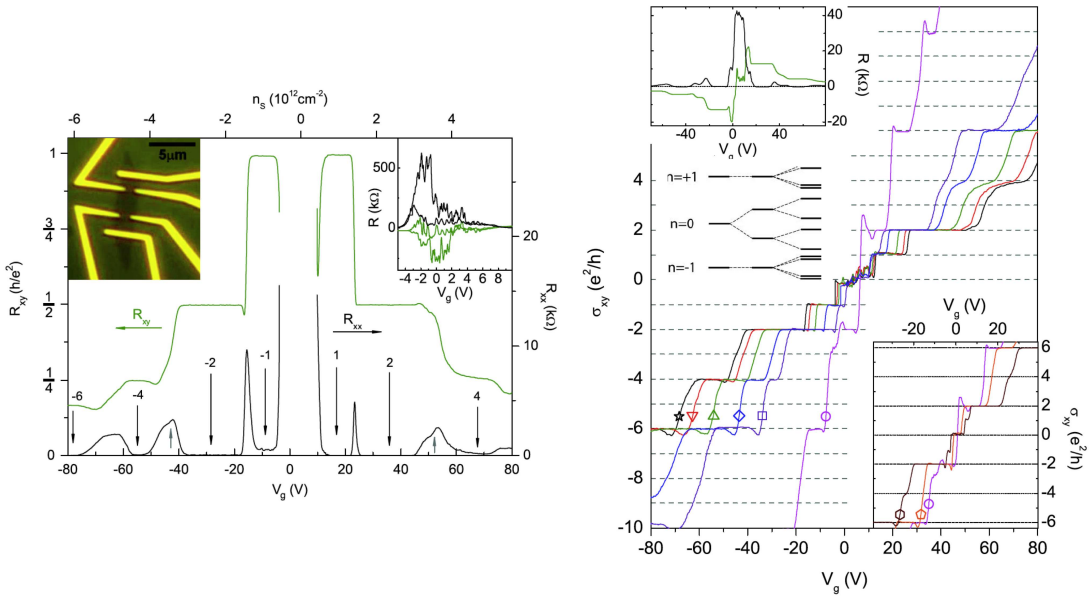

Figure 1.3 : (left) R_{xx} and R_{xy} measured in graphene as a function of V_g at $B = 45$ T and T=1.4 K. Filling factor sequence is indicated. (right) σ_{xy} as a function of V_g at different magnetic fields. The new set of QH plateaus are clearly resolved [6]

$\nu = 0, \pm 1$ QH plateaus indicates that the magnetic field lifts the four-fold degeneracy (two for spin and two for valley) of the $n = 0$ LL [6]. Many-body electron correlation effects within the LL or the opening of a gap at the Dirac point have been suggested as possible origins for the lifting of the degeneracy [6, 10–13].

The magneto-optical properties of graphene are also expected to be equally unusual [7, 14–23]. In the magnetic quantum limit, where the Fermi energy resides in the lowest LL, it is predicted that the $n = 0$ LL gives rise to an anomalous absorption peak in the optical conductivity that, unlike other LLs, never halves its intensity before disappearing as the chemical potential is varied [20]. Furthermore, due to the nonparabolicity of the energy dispersion, graphene is shown to be a nonlinear material that, when irradiated by a monochromatic wave, will scatter the radiation in a

broad frequency range, possibly explaining the broad cyclotron resonance linewidths observed experimentally [23–25].

Accordingly, the linear dispersion relation of graphene also evades the basic requirement for Kohn's theorem, which states that electron-electron interactions should not appear in cyclotron resonance (CR) [26]. More specifically, considering the Hamiltonian for an electron system with a parabolic dispersion in a magnetic field with a Coulomb potential included for electron-electron interactions,

$$\hat{H} = \frac{1}{2m}\sum_{i=1}^{N} P_i^2 + \sum_{i,j} u(\boldsymbol{r}_i - \boldsymbol{r}_j) \tag{1.3}$$

where

$$\boldsymbol{P}_i = \boldsymbol{p}_i + e\boldsymbol{A}_i, \quad \boldsymbol{P} = \sum_{i=1}^{N} \boldsymbol{P}_i, \tag{1.4}$$

the equation of motion for $\boldsymbol{P}$, as determined by the Ehrnfest theorem, becomes:

$$\frac{d\boldsymbol{P}}{dt} = \frac{i}{\hbar}[\hat{H}, \boldsymbol{P}] = -\frac{e}{m}\boldsymbol{P} \times \boldsymbol{B}, \tag{1.5}$$

which does not contain the Coulomb potential term [27]. Equation (1.5) implies that electron-electron interactions do not show up in CR because the effective mass does not depend on electron-electron interactions and incident electromagnetic radiation only couples with the center-of-mass motion of the system [27]. However, this only holds for electrons with a parabolic dispersion and perfect translational symmetry and can be violated if, for example, there is an impurity potential or two different kinds of carriers that can result in many-body effects in the magnetic quantum limit for traditional GaAs 2DEG systems [27–31]. Most importantly, the linear

dispersion relation of graphene automatically invalidates Kohn's theorem, motivating CR studies to explore many-body interactions in graphene.

A number of CR measurements have been performed on graphene [2, 24, 25, 32–39], successfully resolving the unusual LL structure, particularly when the graphene samples investigated have relatively high mobilities, such as exfoliated graphene or SiC-converted graphene. However, for technologically important applications requiring large area graphene films grown via chemical vapor deposition (CVD), we still face the current problem of low mobilities ($<10^3$ cm^{-2} V^{-1} s^{-1}), which severely broadens CR. Therefore, for these low-mobility samples, CR measurements must be explored within the regime of ultrahigh magnetic fields that makes the CR observability condition $\omega_c\tau > 1$ readily achievable (here, ω_c is the cyclotron frequency and τ is the carrier scattering time). Furthermore, a pulsed high-field magnet can be readily combined with an infrared laser to perform CR measurements with circularly-polarized radiation [40, 41], allowing us to distinguish between electron-like and hole-like CR transitions.

This dissertation presents an experimental study of CR in CVD-grown graphene at ultrahigh magnetic fields. We begin with Chapter 2 by providing a background review of classical and quantum mechanical dynamics of free electrons in high magnetic fields as well as cyclotron resonance. In Chapter 3, we describe the generation of high magnetic fields, including steady fields, nondestructive pulsed fields, and destructive pulsed fields. Chapter 4 extends our background discussion from Chapter 2 to graphene in high magnetic fields and includes a detailed review of the previ-

ous CR experiments mentioned in this chapter. The experimental parameters for the sample investigated and the generation of ultra-high magnetic fields with the National High Magnetic Field Laboratory (NHMFL) Single-Turn Coil system are discussed in Chapter 5. Finally, in Chapter 6, we present our experimental results and theoretical analysis for polarization dependent cyclotron resonance of graphene at ultrahigh magnetic fields.

Chapter 2

Electrons in Magnetic Fields

2.1 Classical Dynamics

We first begin by addressing the influence of electric and magnetic fields on spinless, free electrons with classical dynamics [42]. The kinetic equation for electrons moving with velocity $\boldsymbol{v}$ in an electric field $\boldsymbol{E}$ and magnetic field $\boldsymbol{B}$, also known as the Lorentz Force, is given by

$$\boldsymbol{F} = -e\boldsymbol{E} - e(\boldsymbol{v} \times \boldsymbol{B}). \tag{2.1}$$

To derive the Lagrangian for this problem, we first need to express the electric and magnetic fields in terms of a scalar potential, ϕ, and a vector potential, $\boldsymbol{A}$, as

$$\boldsymbol{E} = -\nabla\phi - \frac{\partial \boldsymbol{A}}{\partial t}, \tag{2.2}$$

$$\boldsymbol{B} = \nabla \times \boldsymbol{A}. \tag{2.3}$$

Substituting Eqs. (2.2) and (2.3) in the Lorentz force [Eq. (2.1)], we have

$$\boldsymbol{F} = -e\left[-\nabla\phi - \frac{\partial \boldsymbol{A}}{\partial t} + (\boldsymbol{v} \times (\nabla \times \boldsymbol{A}))\right]. \tag{2.4}$$

If we expand the last term of Eq. (2.4) in terms of its vector identity and note that $\frac{d\boldsymbol{A}}{dt} = \frac{\partial \boldsymbol{A}}{\partial t} + (\boldsymbol{v} \cdot \nabla)\boldsymbol{A}$, the Lorentz force now becomes

$$\boldsymbol{F} = -e\left[-\nabla\phi + \nabla(\boldsymbol{v} \cdot \boldsymbol{A}) - \frac{d\boldsymbol{A}}{dt}\right]. \tag{2.5}$$

Considering a single component of the Lorentz force, for example, the z-component, where

$$F_z = -e\left[-\frac{\partial}{\partial z}(\phi - \boldsymbol{v}\cdot\boldsymbol{A}) - \frac{dA_z}{dt}\right], \tag{2.6}$$

we can write F_z into a form that corresponds to Lagrange's equation for the specific case of a velocity-dependent potential U, i.e., $F_i = -\frac{\partial U}{\partial q_i} + \frac{d}{dt}\frac{\partial U}{\dot{q}_i}$ [43]. More specifically, Eq. (2.6) becomes

$$F_z = -e\left[-\frac{\partial}{\partial z}(\phi - \boldsymbol{v}\cdot\boldsymbol{A}) + \frac{d}{dt}\frac{\partial}{\partial v_z}(\phi - \boldsymbol{v}\cdot\boldsymbol{A})\right], \tag{2.7}$$

with U defined as

$$U = e(\boldsymbol{v}\cdot\boldsymbol{A}) - e\phi. \tag{2.8}$$

As a result, it becomes straightforward to derive the Lagrangian, $\mathcal{L} = T - U$, as

$$\mathcal{L} = \frac{1}{2}m\boldsymbol{v}^{\boldsymbol{2}} - e(\boldsymbol{v}\cdot\boldsymbol{A}) + e\phi. \tag{2.9}$$

With the Lagrangian now defined, we can generate the Hamiltonian, where

$$H = \boldsymbol{p}\cdot\boldsymbol{v} - \mathcal{L}. \tag{2.10}$$

Calculating the generalized momentum,

$$\boldsymbol{p} = \frac{\partial\mathcal{L}}{\partial\boldsymbol{v}} = m\boldsymbol{v} - e\boldsymbol{A}, \tag{2.11}$$

we note that the momentum has an additional term, $-e\boldsymbol{A}$, that is unlike the mechanical momentum, $\boldsymbol{p} = m\boldsymbol{v}$, of systems with forces derived from a potential energy [44]. This, however, is expected as $U = e(\boldsymbol{v}\cdot\boldsymbol{A}) - e\phi$ determined for the Lorentz force is not the potential energy of a charged particle. Nevertheless, it is easy to show

that the Lagrangian derived from the Lorentz force produces the correct dynamics for the Hamiltonian, where $H = T + V$. Replacing Eq. (2.11) into the Hamiltonian, we have

$$\begin{aligned} H &= m\boldsymbol{v}\cdot\boldsymbol{v} - e(\boldsymbol{v}\cdot\boldsymbol{A}) - \frac{1}{2}m\boldsymbol{v}\cdot\boldsymbol{v} - e\phi + e(\boldsymbol{v}\cdot\boldsymbol{A}) \\ &= \frac{1}{2}m\boldsymbol{v^2} - e\phi = T - e\phi. \end{aligned} \tag{2.12}$$

Rewriting $\boldsymbol{v}$ in terms of the generalized momentum, we finally derive the Hamiltonian for a free, spinless electron in a magnetic field:

$$H = \frac{[\boldsymbol{p} + e\boldsymbol{A}]^2}{2m} - e\phi. \tag{2.13}$$

Let us now consider a 2-D free electron system in the x-y plane with a magnetic field oriented in the $\hat{z}$-direction and with no electric field. We choose a Landau gauge $\boldsymbol{A} = Bx\hat{y}$, such that $\boldsymbol{B} = \nabla \times \boldsymbol{A} = B\hat{z}$. Expanding Eq. (2.13) as

$$\begin{aligned} H &= \frac{1}{2m}(\boldsymbol{p} + e\boldsymbol{A})(\boldsymbol{p} + e\boldsymbol{A}) \\ &= \frac{1}{2m}(\boldsymbol{p}^2 + e\boldsymbol{A}\cdot\boldsymbol{p} + e\boldsymbol{p}\cdot\boldsymbol{A} + e^2\boldsymbol{A}^2) \\ &= \frac{1}{2m}(p_x^2 + p_y^2 + eBxp_y + eBp_yx + e^2B^2x^2), \end{aligned} \tag{2.14}$$

we can solve Hamilton's Equations such that

$$\dot{x} = \frac{\partial H}{\partial p_x} = \frac{p_x}{m} \tag{2.15}$$

$$\dot{y} = \frac{\partial H}{\partial p_y} = \frac{eB}{m}\left(x + \frac{p_y}{eB}\right) \tag{2.16}$$

$$\dot{p_x} = -\frac{\partial H}{\partial x} = -\frac{e^2B^2}{m}\left(x + \frac{p_y}{eB}\right) \tag{2.17}$$

$$\dot{p_y} = -\frac{\partial H}{\partial y} = 0. \tag{2.18}$$

If we define $x' = x + \frac{p_y}{eB}$ and combine Eqs. (2.15) and (2.17), we obtain

$$\ddot{x'} = \frac{\dot{p_{x'}}}{m} = -\frac{e^2B^2}{m^2}x' \quad \Rightarrow \quad \ddot{x'} = -\omega^2 x' \tag{2.19}$$

$$\dot{y'} = \frac{eB}{m}x' \quad \Rightarrow \quad \dot{y'} = \omega x', \tag{2.20}$$

where $\omega = eB/m$. Solving for the general solution of Eqs. (2.19) and (2.20), we have

$$\begin{aligned} x(t) &= X + r_c \cos\omega_c(t - t_0) \\ y(t) &= Y + r_c \sin\omega_c(t - t_0), \end{aligned} \tag{2.21}$$

where Eq. (2.21) describes the circular motion centered at (X, Y) of electrons in a magnetic field with radius $r_c = mv/eB$ and cyclotron frequency $\omega_c = eB/m$ [42].

2.2 Landau Quantization

Let us now expand the Hamiltonian from Eq. (2.13) with the quantum mechanical operator of the momentum, $\hat{\boldsymbol{p}} = -i\hbar\nabla$, such that

$$\begin{aligned} \hat{H} &= \frac{1}{2m}\left[\hat{\boldsymbol{p}} + e\hat{\boldsymbol{A}}\right]^2 \\ &= \left[\frac{-\hbar^2\nabla^2}{2m} - \frac{ie\hbar Bx}{m}\frac{\partial}{\partial y} + \frac{e^2B^2x^2}{2m}\right]. \end{aligned} \tag{2.22}$$

As the Hamiltonian does not explicitly depend on the y coordinate [42, 45], we can write the wave function as

$$\Psi = e^{ik_y y}\varphi(x). \tag{2.23}$$

We can write the Schrödinger equation, $\hat{H}\Psi = E\Psi$, as

$$\left[\frac{-\hbar^2\nabla^2}{2m} - \frac{ie\hbar Bx}{m}\frac{\partial}{\partial y} + \frac{e^2B^2x^2}{2m}\right] e^{i(k_y y)}\varphi(x) = E\, e^{i(k_y y)}\varphi(x)$$

$$\left[\frac{\hbar^2 k_y^2}{2m} - \frac{\hbar^2}{2m}\frac{\partial^2}{\partial x^2} + \frac{e\hbar Bk_y x}{m} + \frac{e^2B^2x^2}{2m}\right]\varphi(x) = E\,\varphi(x). \tag{2.24}$$

Let us now define $x = x' - x_0$, such that

$$x_0 = k_y l_B^2 = \frac{\hbar k_y}{m\omega_c}, \tag{2.25}$$

where the magnetic length, l_B, is given by $l_B = \sqrt{\hbar/eB}$ and the cyclotron frequency, ω_c, is given by $\omega_c = eB/m$. Replacing x into Eq. (2.24), the Schrödinger equation reduces to

$$\left[-\frac{\hbar^2}{2m}\frac{\partial^2}{\partial x'^2} + \frac{m\omega_c^2 x'^2}{2}\right]\varphi(x) = \varepsilon\,\varphi(x). \tag{2.26}$$

Examining Eq. (2.26), we notice that we have derived the Schrödinger equation for a 1-D simple harmonic oscillator with its center shifted by x_0. As a result, the eigenvalues, also known as Landau levels (LLs), are simply

$$\varepsilon_n = \left(n + \frac{1}{2}\right)\hbar\omega_c. \tag{2.27}$$

The eigenstates are determined by solving the one-dimensional differential equation of Eq. (2.26) [42] such that

$$\varphi(x) = \Phi_n\left(\frac{x + k_y l_B^2}{l_B}\right), \qquad n = 0,\, 1,\, 2\,... \tag{2.28}$$

where

$$\Phi_n(x) = C_n \exp\left(\frac{-x^2}{2}\right) H_n(x) \tag{2.29}$$

is a Harmonic oscillator function with the Hermite polynomials,

$$H_n(x) = (-1)^n e^{x^2} \frac{\partial n}{\partial x^n}(e^{-x^2}). \tag{2.30}$$

Alternatively, we can derive Eq. (2.27) by introducing the Landau raising and lowering operators [40, 42],

$$\hat{a} = \frac{l_B}{\sqrt{2}\hbar}(\hat{\pi}_x - i\hat{\pi}_y), \quad \hat{a}^\dagger = \frac{l_B}{\sqrt{2}\hbar}(\hat{\pi}_x + i\hat{\pi}_y), \quad [\hat{a}, \hat{a}^\dagger] = 1 \tag{2.31}$$

where $\hat{\pi}_{x,y}$ is defined using Peierls substitution

$$\hat{\boldsymbol{p}} \to \hat{\boldsymbol{p}} + e\hat{\boldsymbol{A}} = \hat{\boldsymbol{\pi}}. \tag{2.32}$$

and is written in terms of Eq. (2.31) as

$$\hat{\pi}_x = \frac{\hbar}{\sqrt{2}l_B}(\hat{a}^\dagger + \hat{a}), \quad \hat{\pi}_y = \frac{\hbar}{i\sqrt{2}l_B}(\hat{a}^\dagger - \hat{a}). \tag{2.33}$$

The Hamiltonian from Eq. (2.22) now becomes

$$\hat{H} = \frac{1}{2m}\left(\hat{\boldsymbol{p}} + e\hat{\boldsymbol{A}}\right)^2 = \frac{1}{2m}\left(\hat{\pi}_x^2 + \hat{\pi}_y^2\right). \tag{2.34}$$

Replacing Eq. (2.33) into the Hamiltonian of Eq. (2.34), we can show that the Hamiltonian reduces to

$$\hat{H} = \hbar\omega_c\left(\hat{a}^\dagger\hat{a} + \frac{1}{2}\right). \tag{2.35}$$

If we note that $\hat{a}^\dagger\hat{a}|n\rangle = n|n\rangle$, it becomes straightforward to derive the Landau levels:

$$\hat{H}\Psi = \hbar\omega_c\left(n + \frac{1}{2}\right)\Psi = \varepsilon\Psi$$

$$\varepsilon = \hbar\omega_c\left(n + \frac{1}{2}\right).$$

To determine the degeneracy of these LLs, let us consider the allowed electronic states in k-space before and after a perpendicular magnetic field is applied. When we apply periodic boundary conditions, Figure 2.1(a) shows electronic states that are uniformly spaced by $2\pi/L$ in the absence of a magnetic field. On the other hand, when a perpendicular magnetic field is applied [Figure 2.1(b)], LLs form that quantize an electron's orbit into certain allowed energies. Because the number of electronic states in k-space is conserved regardless of field, the degeneracy of each LL can be determined from the number of free electron wave-vector states with energies between adjacent LLs [46]:

$$\frac{\hbar^2}{2m}(k_x^2 + k_y^2) = \left(n + \frac{1}{2}\right)\hbar\omega_c. \tag{2.36}$$

From Eq. (2.36), we calculate the area between adjacent LLs:

$$A_n = \pi(k_x^2 + k_y^2) = \left(n + \frac{1}{2}\right)\frac{2\pi eB}{\hbar}$$

$$A_{n+1} = \left[(n+1) + \frac{1}{2}\right]\frac{2\pi eB}{\hbar}$$

$$A_{n+1} - A_n = \frac{2\pi eB}{\hbar}. \tag{2.37}$$

Noting that the number of states per unit area from Figure 2.1(a) is $(L/2\pi)^2$, we can calculate the total number of states, p, per LL:

$$p = \left(\frac{L}{2\pi}\right)^2\left(\frac{2\pi eB}{\hbar}\right), \tag{2.38}$$

and as a result, we see that the degeneracy per unit area of each LL is $eB/2\pi\hbar$.

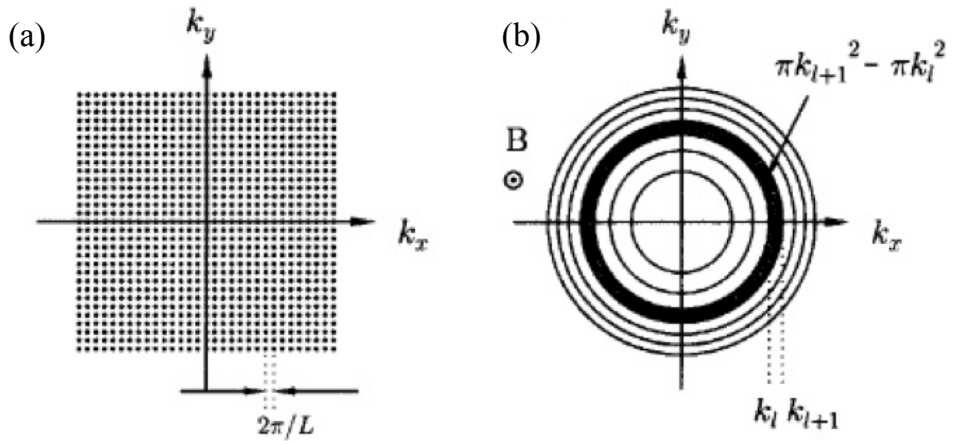

Figure 2.1 : (a) Electronic states in k-space when $B = 0$. (b) Formation of Landau levels in k-space when $B \neq 0$ [47].

2.3 Bloch Electrons in Magnetic Fields

We now consider the motion of electrons moving in a periodic lattice potential, where independent electrons (called Bloch electrons) obey a Schrödinger equation in a periodic lattice potential $U(\boldsymbol{r})$ with Bloch solutions [48]:

$$\psi_{m\boldsymbol{k}}(\boldsymbol{r}) = e^{i\boldsymbol{k}\cdot\boldsymbol{r}} u_{m\boldsymbol{k}}(\boldsymbol{r}), \tag{2.39}$$

$$\hat{H}\psi_{m\boldsymbol{k}}(\boldsymbol{r}) = \left(\frac{\hat{\boldsymbol{p}}^2}{2m} + U(\boldsymbol{r})\right) e^{i\boldsymbol{k}\cdot\boldsymbol{r}} u_{m\boldsymbol{k}}(\boldsymbol{r}) = E_m(\boldsymbol{k}) e^{i\boldsymbol{k}\cdot\boldsymbol{r}} u_{m\boldsymbol{k}}(\boldsymbol{r}), \tag{2.40}$$

where m is the band index. Considering Bloch electrons in the absence of a magnetic field, we can write $\hat{\boldsymbol{p}} = -i\hbar\nabla$ and expand the Hamiltonian such that

$$\left(\frac{\hat{\boldsymbol{p}}^2}{2m} + \frac{\hbar\boldsymbol{k}\cdot\hat{\boldsymbol{p}}}{m} + \frac{\hbar^2 k^2}{2m} + U(\boldsymbol{r})\right) u_{m\boldsymbol{k}}(\boldsymbol{r}) = E_m(\boldsymbol{k}) u_{m\boldsymbol{k}}(\boldsymbol{r}). \tag{2.41}$$

Following standard perturbation theory, let us arrange Eq. (2.41) as $\hat{H} = \hat{H}_0 + \hat{H}'_k$ where

$$\hat{H}_0 = \frac{\hat{\boldsymbol{p}}^2}{2m} + U(\boldsymbol{r}) \tag{2.42}$$

is the unperturbed term corresponding to the Hamiltonian at $\boldsymbol{k} = 0$ and

$$\hat{H}_k' = \frac{\hbar \boldsymbol{k} \cdot \hat{\boldsymbol{p}}}{m} + \frac{\hbar^2 k^2}{2m} \tag{2.43}$$

is the perturbation term, commonly referred to as the $\boldsymbol{k} \cdot \boldsymbol{p}$ perturbation. It follows then from $\boldsymbol{k} \cdot \boldsymbol{p}$ perturbation that if we know the solution to Eq. (2.41) for a point $\boldsymbol{k}_0$, then at a neighboring point $\boldsymbol{k}$ both $u_{m\boldsymbol{k}}$ and $E_{m\boldsymbol{k}}$ can be expanded to second order in terms of the unperturbed eigenfunctions $u_{m\boldsymbol{k}_0}$ and eigenvalues $E_{m\boldsymbol{k}_0}$ by treating terms involving $\boldsymbol{k}$ as perturbations [49].

For simplicity, we choose $\boldsymbol{k}_0 = 0$ and obtain the second order perturbation of the energy $E_{m\boldsymbol{k}}$,

$$E_m(\boldsymbol{k}) = E_m(0) + \frac{\hbar^2 k^2}{2m} + \frac{\hbar^2}{m^2} \sum_{p \neq m} \frac{|\langle u_{m0} | \boldsymbol{k} \cdot \hat{\boldsymbol{p}} | u_{p0} \rangle|^2}{E_m(0) - E_p(0)}, \tag{2.44}$$

which can be written more simply as

$$E_m(\boldsymbol{k}) = E_m(0) + \frac{\hbar^2 k^2}{2\overleftrightarrow{m}^*} \tag{2.45}$$

where

$$(\overleftrightarrow{m}^*)^{-1} = \frac{1}{m} + \frac{2}{m^2 k^2} \sum_{p \neq m} \frac{|\langle u_{m0} | \boldsymbol{k} \cdot \hat{\boldsymbol{p}} | u_{p0} \rangle|^2}{E_m(0) - E_p(0)} \tag{2.46}$$

is the reciprocal effective mass tensor. As a result, we have essentially replaced the effect of the periodic lattice potential on electron motion by an effective mass tensor with matrix elements determined by the unperturbed band structure [40]. This method, called the Effective Mass Approximation (EMA), can now be extended to Bloch electrons in magnetic fields.

If the unperturbed energy-momentum relation $E_m(\boldsymbol{p})$ is known, then the allowed energies of a system perturbed by $\boldsymbol{B}$ are given by solving the effective Schrödinger

equation [40]:

$$\hat{H}F_m(\boldsymbol{r}) = \hat{E}_m(-i\hbar\nabla + e\boldsymbol{A})F_m(\boldsymbol{r}) = EF_m(\boldsymbol{r}), \tag{2.47}$$

where $F_m(\boldsymbol{r})$ is an envelope function given by

$$\Psi(\boldsymbol{r}) = \sum_m F_m(\boldsymbol{r})\psi_{m0}(\boldsymbol{r}). \tag{2.48}$$

For the case when E_m has a parabolic and isotropic dispersion $E_m(\boldsymbol{p}) = |\boldsymbol{p}|^2/2m^*$, then

$$\hat{H}_0 = \frac{1}{2m^*}\left(\hat{\pi}_x^2 + \hat{\pi}_y^2\right), \tag{2.49}$$

which is the same as Eq. (2.34) from Section 2.2 and has eigenvalues

$$\varepsilon = \left(n + \frac{1}{2}\right)\hbar\omega_c,$$

where $\omega_c = eB/m^*$. Therefore, we obtain the same energy for Bloch electrons as free electrons except the free electron mass is replaced by the effective mass [42].

We can alternatively derive the effective mass for nondegenerate bands from the semiclassical equations of motion [48, 50]:

$$\hbar\dot{\boldsymbol{r}} = \hbar\boldsymbol{v}_m(\boldsymbol{k}) = \frac{\partial E_m(\boldsymbol{k})}{\partial \boldsymbol{k}} \tag{2.50}$$

$$\hbar\dot{\boldsymbol{k}} = -e[\boldsymbol{E}(\boldsymbol{r},t) + \boldsymbol{v}_m(\boldsymbol{k}) \times \boldsymbol{B}(\boldsymbol{r},t)] = m^*\ddot{\boldsymbol{r}}. \tag{2.51}$$

Combining Eqs. (2.50) and (2.51) [46], we have

$$\ddot{\boldsymbol{r}} = \frac{1}{\hbar}\frac{\partial}{\partial t}\frac{\partial E_m(\boldsymbol{k})}{\partial \boldsymbol{k}} = \frac{1}{\hbar}\frac{\partial^2 E_m(\boldsymbol{k})}{\partial \boldsymbol{k}^2}\frac{d\boldsymbol{k}}{dt} = \frac{1}{\hbar^2}\frac{\partial^2 E_m(\boldsymbol{k})}{\partial \boldsymbol{k}^2}m^*\ddot{\boldsymbol{r}}. \tag{2.52}$$

where the effective mass is defined by

$$m^* = \hbar^2\left(\frac{\partial^2 E_m(\boldsymbol{k})}{\partial \boldsymbol{k}^2}\right)^{-1}. \tag{2.53}$$

2.4 Cyclotron resonance

In the following section, we reference the detailed review of cyclotron resonance (CR) by J. Kono and N. Miura and their corresponding references [27, 40, 50]. The simplest description for CR is as follows: in a DC magnetic field $\boldsymbol{B}$, particles with effective mass m^* and charge e will spiral around the magnetic field with frequency

$$\omega_c = \frac{eB}{m^*} \tag{2.54}$$

known as the cyclotron frequency, as derived in Section 2.1. If we simultaneously apply an AC electric field with $\omega = \omega_c$, the particle will resonantly absorb energy until collision with scatterers. Therefore, in order to observe CR, the time between collisions τ must satisfy

$$\tau > \frac{T_c}{2\pi} = \frac{1}{\omega_c} \quad \text{or} \quad \omega_c\tau = \frac{eB}{m^*}\tau = \mu B > 1, \tag{2.55}$$

where T_c is the period of cyclotron motion and $\mu = e\tau/m^*$ is the DC mobility. One primary purpose of CR measurements is to determine the components of the effective mass tensor at the extrema of the conduction and valence bands or the Fermi surface. As $\boldsymbol{B}$ or ω can be swept through the resonance and are both known quantities in an experiment, the effective mass can then be calculated from Eq. (2.54). Secondly, CR can be used to study carrier scattering in solids by measuring the temperature dependence of the scattering lifetime τ, as determined from the linewidth of the CR peak. Finally, for real solids, their band dispersions are generally not given by a simple parabolic relation. To obtain their LLs, one can compare CR experimental results to the various theoretical approximation models to test the band theory.

We now review the basic physics of CR via the semiclassical Drude description and the quantum mechanical description for CR. In the semiclassical Drude description, the motion of electrons in a magnetic field $\boldsymbol{B}$ and electric field $\boldsymbol{E}$ follow the equation of motion

$$\overleftrightarrow{m}^* \cdot \frac{d\boldsymbol{v}}{dt} + \overleftrightarrow{m}^* \cdot \frac{\boldsymbol{v}}{\tau} = e(\boldsymbol{E} + \boldsymbol{v} \times \boldsymbol{B}), \tag{2.56}$$

where $\boldsymbol{v}$ is the drift velocity, τ the scattering lifetime, and e is negative for electrons. Let us define $\boldsymbol{E}$ and $\boldsymbol{v}$ such that

$$\boldsymbol{E}(t) = \boldsymbol{E}_0 \exp(-i\omega t) \tag{2.57}$$

$$\boldsymbol{v}(t) = \boldsymbol{v}_0 \exp(-i\omega t). \tag{2.58}$$

As the current is given by $\boldsymbol{J} = ne\boldsymbol{v} = \overleftrightarrow{\sigma} \cdot \boldsymbol{E}$, we can write out the components of the complex conductivity tensor for the case when $\boldsymbol{B} \parallel \hat{z}$ and $\boldsymbol{E} \perp \hat{z}$:

$$\overleftrightarrow{\sigma} = \begin{pmatrix} \sigma_{xx} & \sigma_{xy} & 0 \\ \sigma_{yx} & \sigma_{yy} & 0 \\ 0 & 0 & \sigma_{zz} \end{pmatrix} \tag{2.59}$$

$$\sigma_{xx} = \sigma_{yy} = \sigma_0 \frac{i\omega\tau + 1}{(i\omega\tau + 1)^2 + \omega_c^2\tau^2} \tag{2.60}$$

$$\sigma_{xy} = -\sigma_{yx} = \sigma_0 \frac{\omega_c^2\tau^2}{(i\omega\tau + 1)^2 + \omega_c^2\tau^2} \tag{2.61}$$

$$\sigma_{zz} = \sigma_0 \frac{1}{(i\omega\tau + 1)} \tag{2.62}$$

$$\sigma_0 = ne\mu = \frac{ne^2\tau}{m^*}, \tag{2.63}$$

where σ_0 is the DC conductivity. We can now derive the power absorption of the radiation by the carriers, $P = \langle \boldsymbol{J}(t) \cdot \boldsymbol{E}(t) \rangle$, when $\boldsymbol{E}$ is linearly polarized in the

$\hat{x}$-direction:

$$P = \frac{1}{2}|E_0|^2 \Re(\sigma_{xx}). \tag{2.64}$$

Combining Eqs. (2.60) and (2.64), we obtain

$$P(\omega) = \frac{1}{4}|E_0|^2 \sigma_0 \left[\frac{1}{(\omega - \omega_c)^2\tau^2 + 1} + \frac{1}{(\omega + \omega_c)^2\tau^2 + 1} \right]. \tag{2.65}$$

Figure 2.2 plots the CR absorption power as a function of ω_c/ω. We first note that Eq. (2.65) has two resonances, $\omega = \pm\omega_c$, that correspond to right ($+\omega_c$) and left ($-\omega_c$) circular polarizations. When $\omega_c/\omega = \pm 1$ (or $\omega = \pm\omega_c$), we see absorption peaks with widths that decrease as $\omega_c\tau$ increases. Moreover, the peaks are only visible when $\omega_c\tau > 1$, the condition described in Eq. (2.55) for observing CR. If we fix the photon energy and sweep the magnetic field, experimental considerations relevant to pulsed field magnets, CR occurs at a magnetic field $\boldsymbol{B}_c$ such that $\omega_c = eB_c/m^*$. As the CR peaks in Figure 2.2 have a Lorentzian shape with half width half maximum ΔB_c such that

$$\omega_c\tau = \frac{B_c}{\Delta B_c} = \mu B, \tag{2.66}$$

we can also obtain information about the carrier scatting or mobility μ from ΔB_c and B_c. Finally, from the sign of the polarization, we can determine the carrier type (electrons or holes).

Given that CR is regarded as a transition of electrons between LLs absorbing the energy of the photons of radiation, we now consider the quantum mechanical description of CR. In the Faraday geometry, in which $\boldsymbol{q} \| \boldsymbol{B} \| \hat{z}$, where $\boldsymbol{q}$ is the wavevector of

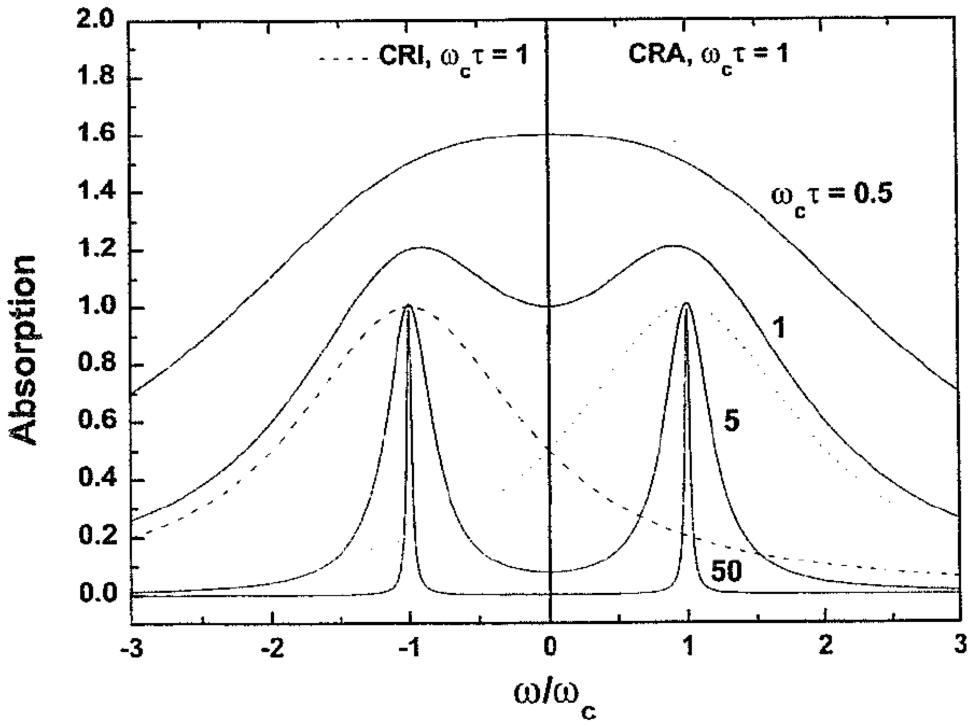

Figure 2.2 : The CR absorption power versus ω for different values of $\omega_c\tau$ [40].

the EM wave, the AC electric field becomes

$$\boldsymbol{E}_{\pm} = E_0 \frac{1}{\sqrt{2}}(\hat{x} \pm i\hat{y}) \exp([i(q_{\pm}z - \omega t)]). \tag{2.67}$$

If we treat $\boldsymbol{E}_{\pm}$ as a perturbation, where

$$\boldsymbol{A}_{\pm} = \frac{E_0}{\sqrt{2}i\omega}(\hat{x} \pm i\hat{y}) \exp([i(q_{\pm}z - \omega t)]). \tag{2.68}$$

$$\hat{H} = \frac{1}{2m^*} \left[\hat{\boldsymbol{p}} + e(\boldsymbol{A} + \boldsymbol{A}_{\pm})\right]^2, \tag{2.69}$$

then in the electric dipole approximation, the Hamiltonian reduces to

$$\hat{H} = \frac{1}{2m^*}(\hat{\boldsymbol{\pi}})^2 + \frac{e}{m^*} \cdot \boldsymbol{A}_{\pm} = \hat{H}_0 + \hat{H}'. \tag{2.70}$$

Recalling the LL raising and lowering operators $\hat{a}^{\dagger}, \hat{a}$ from Section 2.2, $\hat{H}'$ becomes

$$\begin{aligned} \hat{H}' &= \frac{e}{m^*} \left(\hat{\pi}_x A_{\pm x} + \hat{\pi}_y A_{\pm y}\right) \\ &= -\frac{eE_0}{\sqrt{2}i\omega m^*} \left(\hat{\pi}_x \pm i\hat{\pi}_y\right) \exp(-i\omega\tau) \\ &= -\frac{e\hbar E_0}{i\omega m^* l_B} \hat{a}_{\pm} \exp(-i\omega\tau). \end{aligned} \tag{2.71}$$

As the perturbation of Eq. (2.71) contains the raising and lowering operators, we immediately see that the perturbation gives rise to the transition between LLs, with a sharp absorption at $\omega = \omega_c$.

Chapter 3

Generation of High Magnetic Fields

3.1 Steady magnetic fields

Today, steady-state high magnetic fields up to 35 T can be generated by two types of electromagnets, those built using superconducting wires (superconducting magnets) and those built using conductors with normal resistivity (resistive magnets) [51]. Among the two types, superconducting magnets have an advantage over resistive magnets in that it can generate intense magnetic fields without Joule heating loss, as superconducting magnets can sustain very high current densities with zero resistance [52]. For operation, the superconducting magnet must be cooled cryogenically below its critical temperature to transition from a normal state to a superconducting state. As depicted in Figure 3.1, the primary components of the superconducting magnet are devoted to cryogenic cooling, with a liquid nitrogen outer jacket surrounding a liquid helium filled cryostat that contains the magnet.

For most superconducting materials, the boiling point of liquid helium is much less than their critical temperatures, which provides an added advantage of maintaining their superconducting states with higher currents and magnetic fields. However, it is also these critical currents and upper critical fields that can limit the maximum magnetic fields achieved with a superconducting magnet. Table 3.1 lists the

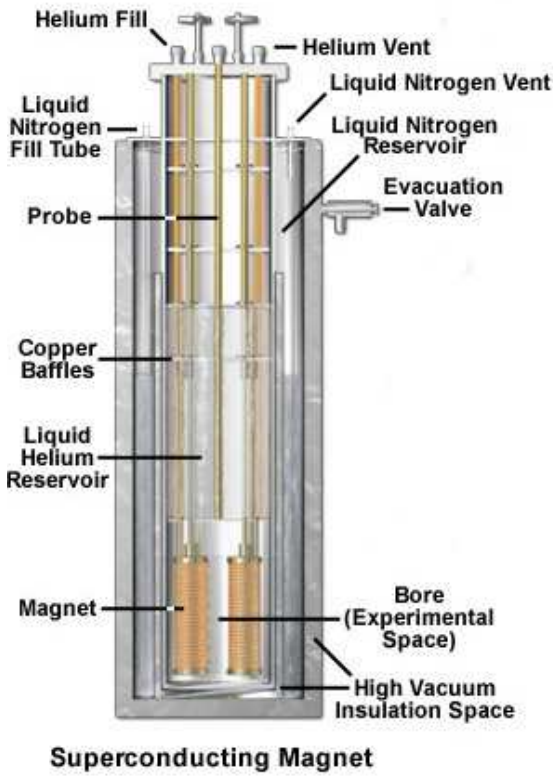

Figure 3.1 : Schematic of a Superconducting Magnet [53].

Table 3.1 : Type II superconducting alloys listing critical temperatures and upper critical magnetic fields [54].

Material	T_c	B_{c2}
Nb-Ti	10.2	12
Nb-Zr	10.8	11
V_3Ga	16.5	22
V_3Si	17.0	
Nb_3Sn	18.3	22
Nb_3Al	18.9	32
Nb_3(Al,B,Be)	20.0	
Nb_3Ga	20.3	34
Nb_3(Al,Ge)	20.5	41
Nb_3Ge	23	30
NbCN	16	25
V_2(Hf,Zr)	10.1	24
$PbMo_6S_8$	14	45

critical temperatures and magnetic fields for type II superconducting alloys. Among the list, most superconducting magnets are typically made from niobium-titanium, Nb-Ti, where filaments of this superconductor are embedded in a copper matrix, as shown in Figure 3.2. The copper matrix aids in absorbing any heat generated that could result in temperatures rising above the critical temperature. Superconducting magnets composed of Nb-Ti produce maximum magnetic fields of $\sim$15 T. To access higher magnetic fields, a combination of Nb-Ti for lower magnetic fields and Nb_3Sn for higher magnetic fields or various high temperature superconductors are used [54]. Currently, the National Institute for Materials Science in Japan holds the record of 24 T for the highest magnetic field generated with a fabricated GdBCO thin film wire, which is an oxide high temperature superconducting wire material [55].

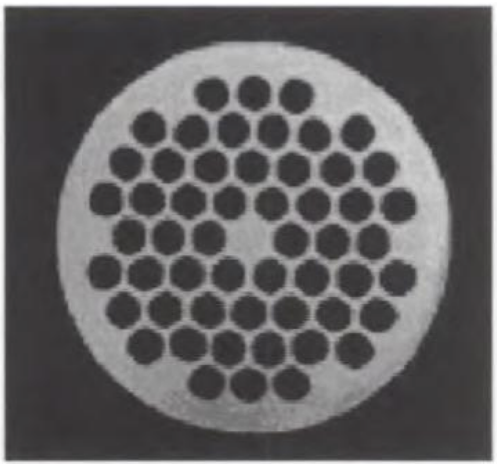

Figure 3.2 : An example of a multifilamentary Nb-Ti superconductor embedded in a copper matrix [54].

Unlike superconducting magnets, resistive magnets are not limited in their performance by critical currents, fields, and temperatures. Ideally, it is possible to generate an infinitely high magnetic field with resistive magnets. However, because resistive magnets require electrical power and efficient cooling, the generation of very high magnetic fields becomes only a question of economics [51]. Figure 3.3 shows a typical Bitter magnet configuration for most resistive magnets. The Bitter magnet, invented by Francis Bitter at Massachusetts Institute of Technology in the 1930s, consists of a series of plates with an array of round holes that transmit water under high pressure to form cooling channels for the magnet [56–59]. In 1938, Bitter successfully generated 10 T with this magnet design and in 1960, the Francis Bitter National Magnet Laboratory (FBNML) was established with 25 well equipped magnet stations that included many types of Bitter magnets operating up to 23.5 T and two hybrid magnets that were developed [60]. However, when the National High Magnetic Field

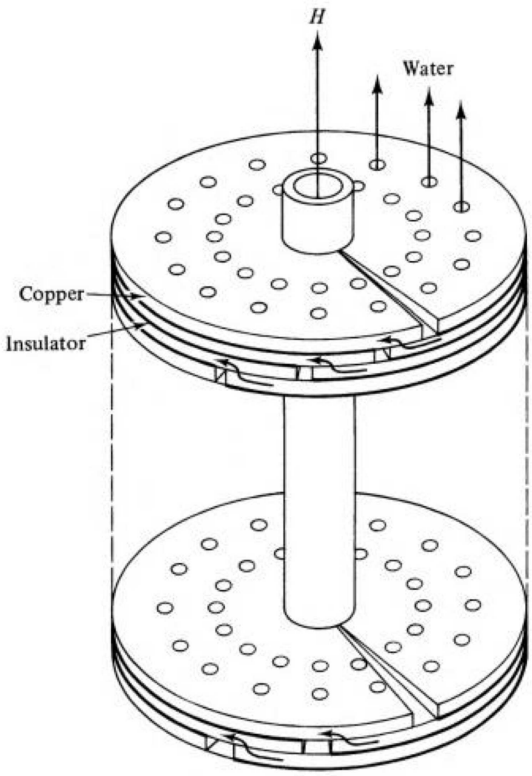

Figure 3.3 : Bitter Magnet [61].

Laboratory (NHMFL) at Tallahassee, Florida became fully operational, the 10 MW power supply closed down, leaving only the pulsed field installation in operation [60].

Although the typical Bitter magnet configuration regularly generates high magnetic fields of up to $\sim$ 20 T, it also generates current density strains on the magnet. Over the years, many improvements were made to remove these constraints, most notably, the Florida-Bitter magnet that uses staggered, elongated holes to withstand larger current densities and generate higher magnetic fields (Figure 3.4). To date, 36.2 T is the highest magnetic field generated by a resistive magnet, a record held by the NHMFL in Tallahassee [62].

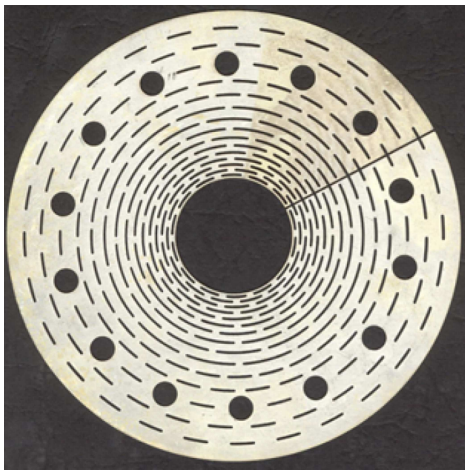

Figure 3.4 : Florida-Bitter plate that uses staggered, elongated holes to withstand larger current densities and improve upon the standard Bitter plate [63].

It should be emphasized that the highest magnetic fields generated solely by either a superconducting magnet or resistive magnet have been surpassed by hybrid magnet technology that consists of both resistive and superconducting magnets combined together [63]. More specifically, the hybrid magnets that produce the highest fields implement an outer coil using superconducting technology and an inner coil using resistive-magnet technology. Figure 3.5 diagrams a cross section of the hybrid magnet at the NHMFL in Tallahassee, Florida, where the world record of 45 T is held.

3.2 Non-destructive pulsed magnetic fields

To access magnetic fields higher than those generated using steady-state magnets, continuous field strength must be sacrificed for the shorter time duration of pulsed field magnets. However, even though higher fields are only generated during a smaller time duration, on the order of ms or μs, the current carrying conductors of pulsed

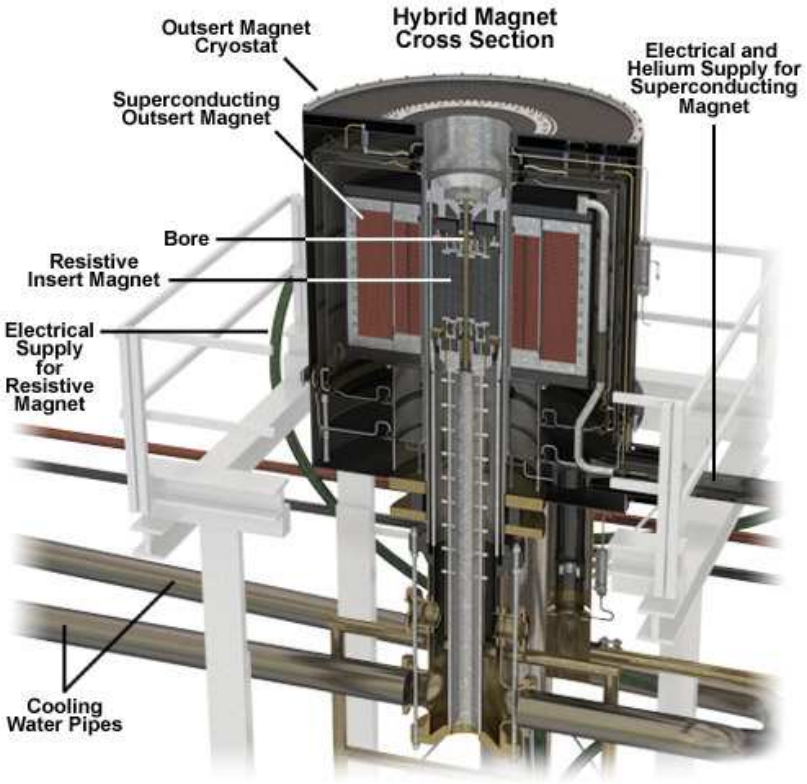

Figure 3.5 : The Hybrid magnet at the NHMFL combines an 11.5 T superconducting magnet with a 33.5 T resistive magnet to generate 45 T dc magnetic field [53].

field magnets are heated adiabatically, described by the action integral [64]:

$$J(T_0, T) = \int_{T_0}^{T} \frac{D\, c_p}{\rho} dT = \int_{t_0}^{t} j^2 dt \tag{3.1}$$

where D is the density, c_p the specific heat, ρ the resistivity, and j the current density, and are ultimately allowed to cool down after each run [65–67]. As a result, this removes the requirement of continuous cryogenic and/or water cooling.

Table 3.2 provides a list of international facilities for nondestructive pulsed high magnetic fields. Depending on the pulse duration, there are two types of nondestructive pulsed magnets: short-pulse magnets that are capacitor driven and long-pulse, controlled waveform magnets that are motor-generator driven. Irrespective of their power supplies, generation of magnetic fields B >40 T with either short-pulse magnets or long-pulse magnets is dominated by coil winding design that equally distributes the Maxwell stress $\frac{B^2}{2\mu_0}$ throughout the coil and provides reinforcement to avoid coil destruction [64, 66, 68].

Both internal reinforcement, implemented during the coil winding process, and external reinforcement, such as strong metals that encase the magnet winding, are optimized to ensure that Maxwell forces do not exceed the strength of the magnetic material and lead to destruction of the magnet. For most pulsed field magnets, a typical coil made from strong wire is wound around a bobbin, the spacing between the winding is impregnated with epoxy, and the coil is machined and mounted in a stainless steel cylinder, resulting in fields up to ∼60 T for ∼10 ms [68].

In general, there are two types of strong wires developed for successful nondestructive pulsed field generation: micro-filaments of niobium in copper and micro-

Table 3.2 : International nondestructive pulsed field laboratories [68].

	Cap. bank			User coil			Δt
Laboratory	W	V	I_m	W	B	i.d.	Duration
location	[kJ]	[kV]	[kA]	[kJ]	[T]	[mm]	[ms]
Berlin	42	2.5	20	42	51	10	3.5
	400	10	60	400	60	18	8.1
Dresden	1250	10	50	450	50	24	13
				1100	40	24	120
Frankfurt	800	7	100	800	36	22	600
				390	50	24	24
Kashiwa, Tokyo Univ.	900	5/10	50		50	22	50
	200	5	50	200	50	20	20
	200	4	50	200	50	20	18
Kobe	24	3	7.6	24	30	15.4	11
	100	3		34	36	16.5	9
Leuven	475	5	25	300	55	18	20
	600	10	50	260	70	10	8
Los Alamos	1600	10	50	565	60	15	35
				1400	50	15	350
Nijmegen	2000	16	40		55	23	
Osaka	1500	20	1000	240	60	18	7
					70	10	7
	1000	13	40	570	60	18	22
Oxford	800	7	20	150	60	12	10
				250	50	20	20
Sendai	100	5	35	70	40	17	10
				45	30	22	5
Sydney	800	7	60	400	60	22	25
Toulouse	14000	24	30	1250	61	11	150
				3300	58	26	285
Tsukuba	1600	5	100	500	48	16	20
	300	10	30	300	50	20	15
Vienna	75	2.5	50	20	40	25	10

W: stored energy, V: voltage, I_m: the maximum current, i.d.: the inner bore.

filaments of silver in copper [64]. The first type, developed by Foner [69] in 1986, produced fields up to 61 T at 10 ms pulse duration and offered the first breakthrough in the generation of modern long pulse fields [68]. The second type, developed at the National Research Institute for Metals in Tsukuba, Japan [70], has been utilized by Kindo [71] in Osaka, Japan, to make an 80 T coil. Outside of these primary materials, alternative treatments for internal and external reinforcements have been

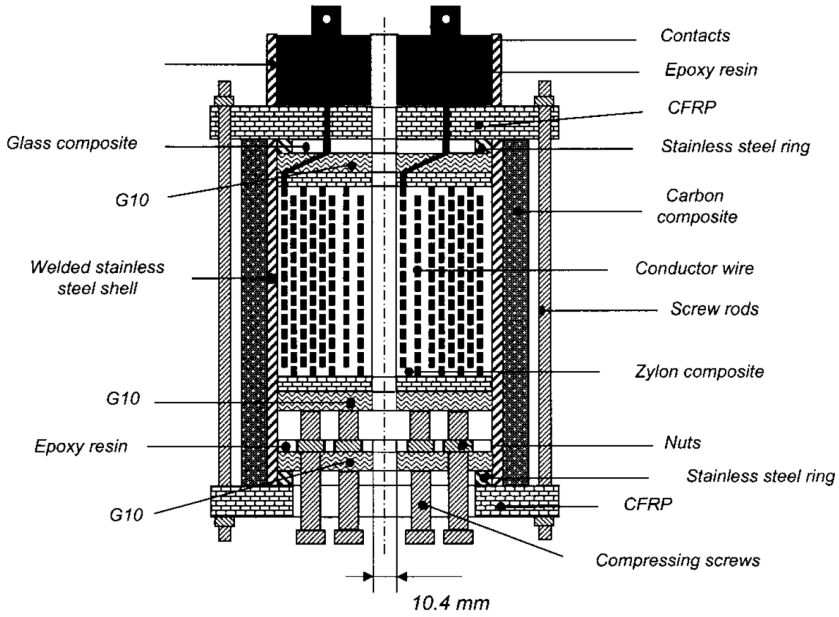

Figure 3.6 : Leuven magnet with internal fiber reinforcement [68, 75].

developed to create strong magnets. One primary example is the work by Herlach *et al*. at Leuven and their reinforcement of soft copper wires with glass fibers [72]. Winding the glass fibers in between the layers of soft copper, with careful consideration taken for the thickness of the glass fibers, allowed a uniform stress distribution throughout the coil due to the high tensile strength of glass fiber compared to the soft copper [68]. Figure 3.6 shows a cross-section of a Leuven magnet that accommodates both the internal fiber reinforcement and an external reinforcement for the magnet. Another notable method involves impregnating the coil with water that freezes when the magnet is cooled with liquid nitrogen and allows for the repetition of shots twice as fast as compared to standard magnets impregnated with epoxy [73, 74].

The combination of strongly reinforced coils with a capacitor bank as the power

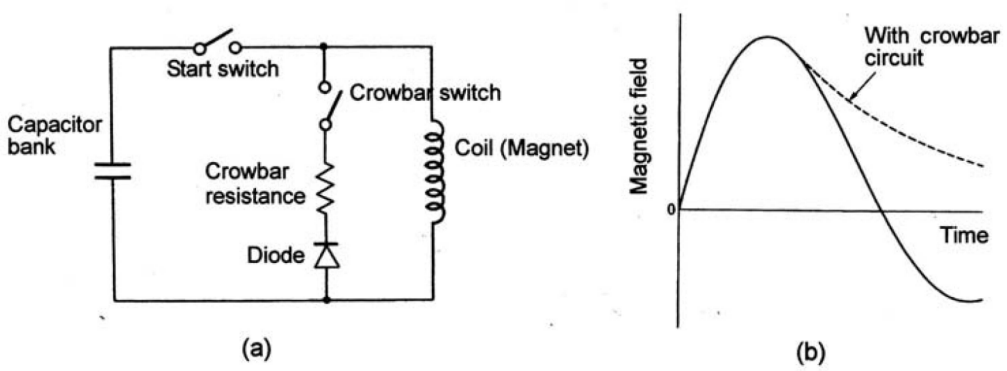

Figure 3.7 : (a) Pulsed magnetic field circuitry with crowbar circuit. (b) Current waveform with and without crowbar circuit [68].

supply produces pulsed fields with typically shorter pulse durations (10 - 50 ms) compared to long pulse magnets powered by large generators. Figure 3.7 shows a typical electric circuit and corresponding current waveforms of short-pulse magnets. Here, the diode in the crowbar circuit begins to conduct right after peak field, not only prolonging the field decay but also extending the life of a capacitor bank by preventing charge reversal [64].

As for long pulse magnets, large generators or city power lines are used to obtain longer pulse durations alongside the ability to generate various pulse shapes of the current such as flat-top or stair-like by using filters and thyristors [68]. One example of such a controlled waveform magnet system is the 60 T long pulse magnet at the NHMFL in Los Alamos, New Mexico, where a 1430 MVA, 24 kV, 60 Hz, 4 pole synchronous generator is used for pulsing and thyristor controlled rectifiers for power conditioning [77]. Figure 3.8 shows the various field profiles for the NHMFL 60 T long pulse magnet.

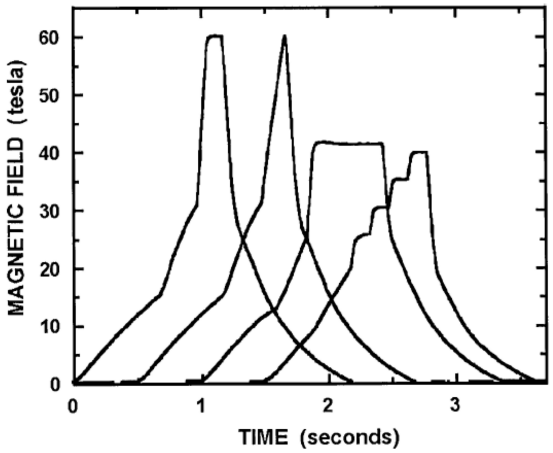

Figure 3.8 : Pulse profiles of the 60 T long pulse magnet, with user-defined pulse shapes [76].

Finally, although the user coils of most pulse field facilities operate up to 70 T, many of the large pulsed field facilities are implementing insert/outsert coil systems aimed at generating fields up to 100 T nondestructively. As the insert and outsert systems are each energized by separate power supplies, the larger outsert coil system provides a background field with a long pulse duration, while the smaller insert coil system adds to the background field with a shorter pulse duration [64]. Considerable effort has been made to reach 100 T from several facilities in the USA, Europe, and Japan, with the most recent achievements at Dresden to 94 T and at the NHMFL-Los Alamos, where they broke the 100 T record with 100.75 T generated nondestructively on March 22, 2012. The 100 T pulsed field magnet at the NHMFL-Los Alamos contains an outsert system consisting of seven coil sets connected in three circuits that is powered by the 1.4 GW generator, while a single coil insert system is powered by a 2 MJ capacitor bank [78].

3.3 Destructive pulsed magnetic fields

For the following discussion, we reference the work of N. Miura and F. Herlach for their detailed review of the generation of megagauss fields [68, 79]. Magnetic fields greater than 100 T (megagauss fields) must be generated destructively, where the metal of the magnet coil explodes violently when exposed to a combination of Joule heating and Maxwell stress. Three different techniques have been developed, each following basic principles for destructive pulsed field generation: as the megagauss pulse field is generated, the magnetic flux from a fast rising field pulse penetrates the inner wall of the coil, where simultaneous Joule heating and increased pressure at the inner surface results in a corresponding shock wave that compresses the coil outward and away from the magnetic field until vaporization of coil on μs timescales.

Table 3.3 lists the Megagauss field facilities for solid state experiments. The first method of megagauss field generation, the explosive-flux compression (EFC), was developed and operated mainly within the US and former USSR. There are two main types of explosive-flux compression techniques, the cylinder type and the bellows type (Figure 3.9), each utilizing an explosive-liner system for implosion/shock wave generation and an initial magnetic flux from a coil and pulsed power supply.

To understand the cylinder type EFC, we must first understand the idea of "flux trapping." Considering the cylindrical coil parameters shown in Figure 3.10, magnetic flux Φ can penetrate the cylinder within a time constant T_c, such that

$$\frac{1}{T_c} = \frac{R}{L} = \frac{2\rho}{\mu_0(r + \frac{d}{2})} = \left| \frac{1}{\Phi} \frac{d\Phi}{dt} \right|. \tag{3.2}$$

If the radius of the cylinder becomes smaller via an implosion within a time inter-

Table 3.3 : International megagauss field facilities for solid state experiments [68].

Laboratory	Country	Technique	Maximum field
Los Alamos	USA	Explosive (Cylindrical)	> 1000 T
		Explosive (Bellows)	200 T
		Single turn coil	∼300 T
Sarov	Russia	Explosive (Cylindrical, 3 cascades)	> 1000 T
ISSP	Japan	Electromagnetic flux compression	622 T
		Single turn coil	302 T
Berlin	Germany	Single turn coil	310 T

val smaller than T_c, the magnetic flux will become trapped and will subsequently compress, causing the magnetic flux density to increase as

$$\frac{B}{B_0} = \frac{r_0^2}{r^2}\frac{\Phi}{\Phi_0} = -\frac{2}{r}v_f, \tag{3.3}$$

where v_f is the flux diffusion speed.

As Figure 3.9(a) shows, for the cylinder type, a metal liner is surrounded by a chemical explosive that, when detonated, causes the liner to rapidly compress inwards. The magnetic flux previously injected into the cylinder is compressed inside the liner and increases proportionally to the inverse of the cross-sectional area of the liner, as described by Eq. (3.3). Magnetic fields over 1000 T have been produced and have been used in a variety of experiments on high T_c superconductors, magnetic transitions, and semiconductor research [81, 82].

Figure 3.9(b) shows the bellows type technique, where the initial magnetic flux

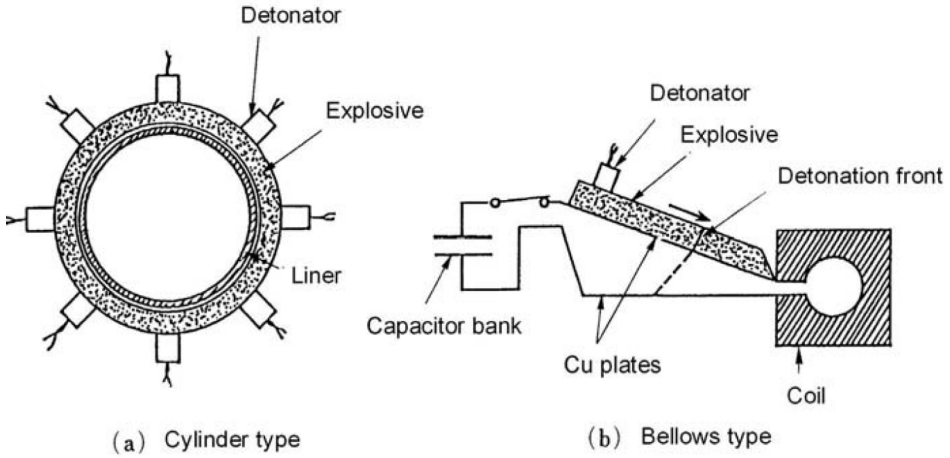

Figure 3.9 : Schematic sketch of explosive flux compression technique for (a) cylinder type and (b) bellows type [68].

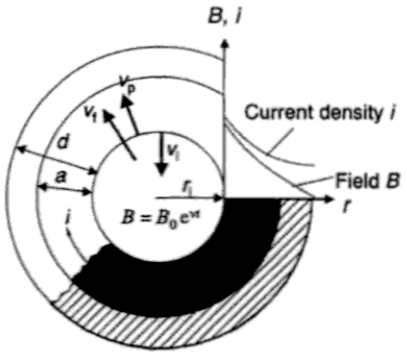

Figure 3.10 : Definition of parameters for a cylindrical implosion experiment [79].

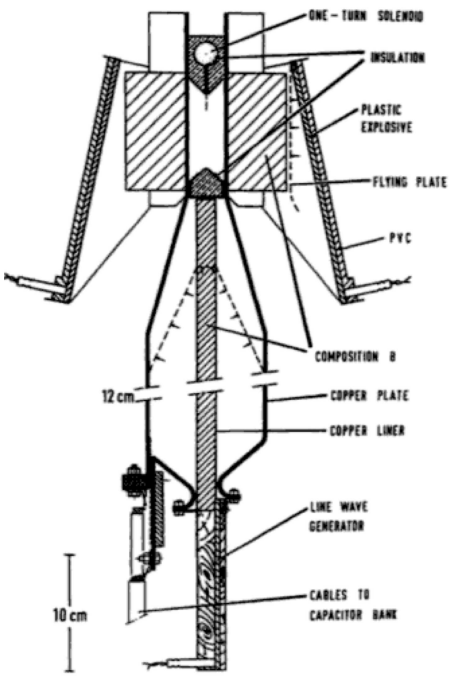

Figure 3.11 : Drawing to scale of a two-stage bellows device [80].

inside a larger loop with copper plates is generated by a capacitor discharge. Once the explosive detonates, it shorts the circuit on the left and causes a shock wave that travels to the right. This wavefront pushes the magnetic flux into the coil positioned on the right and instantly decreasing the cross-sectional area of the loop and increasing the magnetic field inside the coil. One stage bellow systems can produce ∼100 T, while a two-stage bellows system (Figure 3.11) can produce up to ∼200 T [43]. For both EFC techniques, the sample and probe are destroyed every shot.

The next technique, electromagnetic flux compression (EMFC), replaces the chemical explosive with an electromagnetic force to squeeze the liner. Invented by

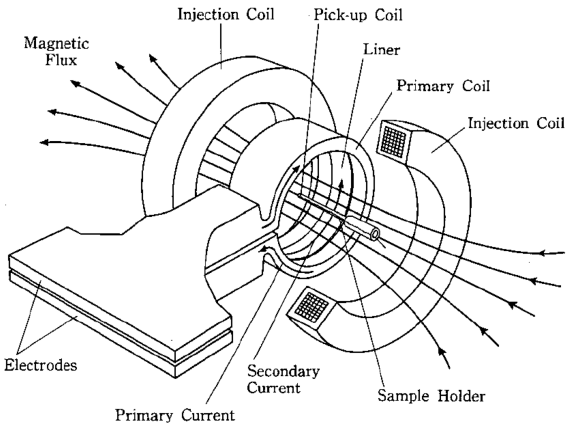

Figure 3.12 : Sketch of primary coil and liner for electromagnetic flux compression [83].

Cnare in 1968 and later developed at the Institute for Solid State Physics (ISSP), the EMFC utilizes a copper ring liner inside a primary coil, as shown in Figure 3.12. When a large pulse current (4-6 MA) is supplied to the primary coil, a secondary current is induced in the liner that flows in the opposite direction. As the two opposing currents repel each other, the liner is squeezed inwards. If a smaller seed magnetic field on the order of 2-3 T had been injected prior to supplying the primary coil current, the seed flux would compress with the implosion of the liner, generating ultra-high magnetic fields proportional to the inverse of the cross-sectional area of the liner. Figure 3.13 shows a sketch of the coil clamping system required for operation. A heavy steel block lined with wood surrounds the primary coil to absorb shock from the experiment.

Figure 3.13 shows a typical experimental trace of the magnetic field generated by EMFC. The peak field of 622 T is generated within a few μs and at the breakpoint,

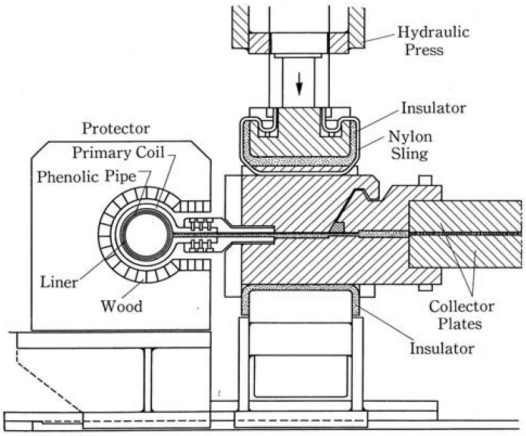

Figure 3.13 : Coil clamping system for EMFC [83].

the field probe and sample are destroyed by the impact of the liner. It should be mentioned that the EMFC technique experiences difficulty involving the feed gap of the coil, where in order to feed the current, there must be a feed gap in the coil, which causes the coil to not be an entire circle. As a result, the feed gap not only causes the magnetic field produced by the primary coil to be weaker at the edges, it also causes the acceleration of the liner to be weaker near the gap, which causes the liner to budge toward the feed gap and results in a dangerous plasma. However, this effect has been improved with the introduction of a feed gap compensator between the primary coil and the liner that improves the symmetry of the implosion.

One major disadvantage of both the EFC and the EMFC techniques is the destruction of the sample during each shot fired. To overcome this disadvantage while still generating ultra-high magnetic fields up to ∼300 T, the single-turn coil (STC) technique can be implemented. In the STC method, a 2-3 mm thick copper plate

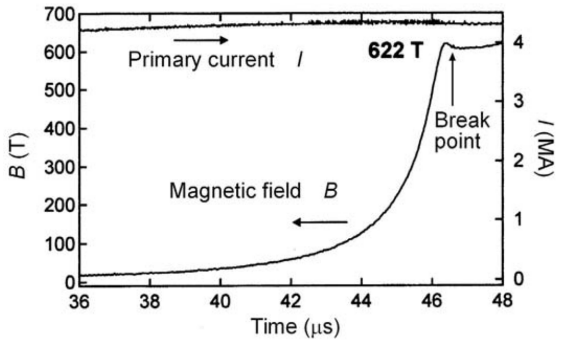

Figure 3.14 : Experimental trace of the 622 T peak magnetic field generated by EMFC [84].

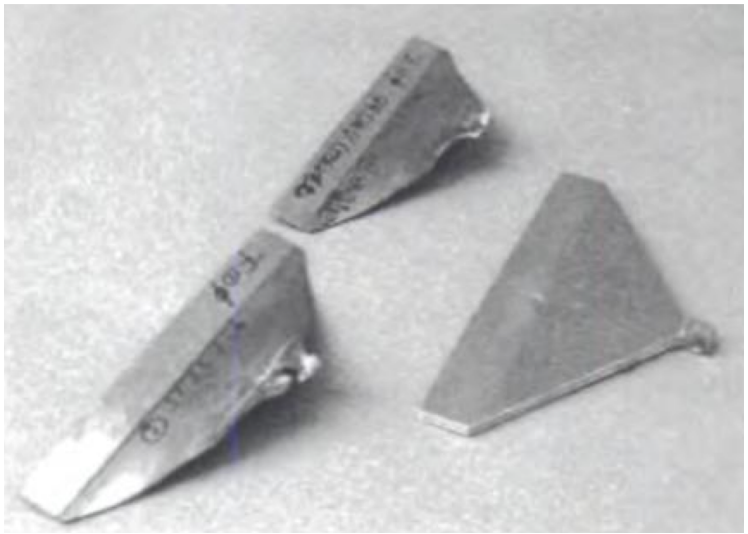

Figure 3.15 : Photograph of single-turn coils before and after a shot [79].

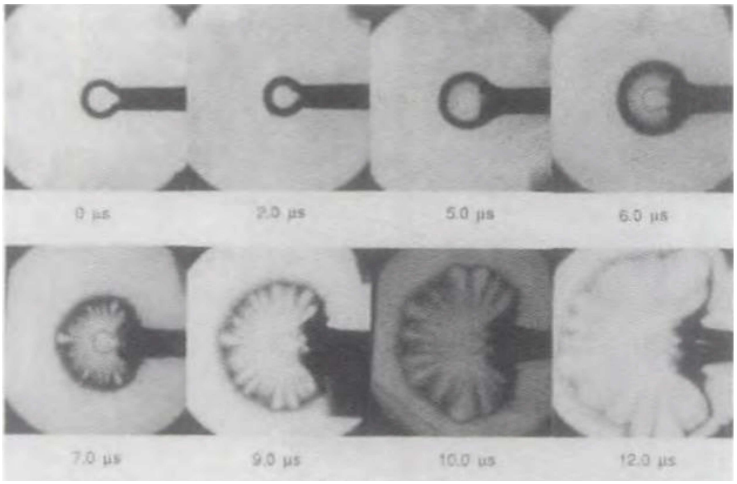

Figure 3.16 : Flash X-ray photographs of the STC during the explosion [79].

is bent to form a small single-turn coil at its end, as shown in Figure 3.15. The coil is clamped with a hydraulic press to collector plates connected to a fast condenser bank. A large pulse current of 2-3 MA is discharged into the small single-turn coil, where very high magnetic fields are subsequently generated. Due to the large Maxwell stress created, the coil is then destroyed as described in the beginning of this section. However, if the current discharge occurs on a fast enough timescale, the high magnetic fields can be generated before destruction of the coil. Figure 3.16 shows a series of high speed X-ray photographs of the coil, with a diameter that grows rapidly after the peak field is reached. The evolution of the coil to a liquid and plasma state can be clearly seen before the explosion of the coil. As the destruction of the coil occurs radially outward, the sample and probe are not destroyed. In Chapter 5 of this thesis, we detail more specifically the operation and generation of ultrahigh magnetic fields via the STC.

Chapter 4

Graphene in High Magnetic Fields

4.1 Electronic band structure

The crystal structure of graphene consists of a 2D honeycomb lattice of carbon atoms with a two-carbon atom (A, B) unit cell shown in Figure 4.1. The unit vectors $\vec{a}_1$ and $\vec{a}_2$ define the unit cell and in real space are defined by

$$\vec{a}_1 = \left(\frac{\sqrt{3}}{2}a, \frac{a}{2}\right), \vec{a}_2 = \left(\frac{\sqrt{3}}{2}a, -\frac{a}{2}\right) \tag{4.1}$$

where $a = |\vec{a}_1| = |\vec{a}_2| = 1.42 \times \sqrt{3} = 2.46$ Å is the lattice constant of graphene [85].

The suggested tight-binding (TB) approach to describe the electronic band structure of graphene dates back to 1947 with Wallace [1], where, considering only the atomic p-orbital and treating the crystal lattice as the perturbation, wavefunctions of graphene can be represented by a linear combination of Bloch functions for the two carbon atom basis (A, B) [86]:

$$\varphi_j(\vec{k}, \vec{r}) = \sum_{j,j'=A,B} C_{jj'}\phi_{j'}(\vec{k}, \vec{r}). \tag{4.2}$$

Considering only the nearest neighbor interactions and solving the coefficient equation $\det(\mathcal{H} - ES)C = 0$, where $H_{jj'} = \langle \varphi_j \mid H \mid \varphi_{j'} \rangle$ and $S_{jj'} = \langle \varphi_j \mid \varphi_{j'} \rangle$ $(j, j' = A, B)$ are the transfer and overlap integrals, respectively, the resulting 2D energy

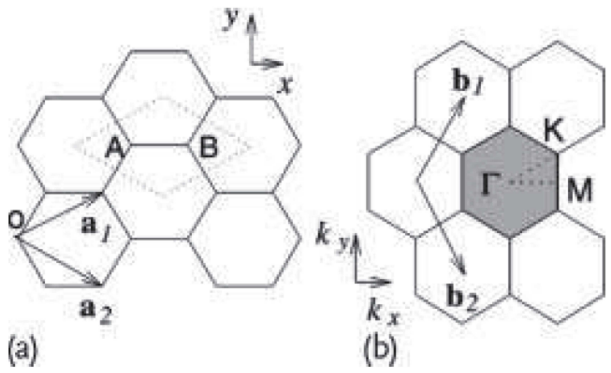

Figure 4.1 : (a) The unit cell and (b) Brillouin zone for monolayer graphene [85].

dispersion is

$$E(k_x, k_y) = \pm\gamma_0 \left\{ 1 + 4\cos\left(\frac{\sqrt{3}k_x a}{2}\right)\cos\left(\frac{k_y a}{2}\right) + 4\cos^2\left(\frac{k_y a}{2}\right) \right\}^{1/2} \tag{4.3}$$

where γ_0 is the transfer integral between nearest neighbor lattice points [85, 86].

Figure 4.2 shows a schematic view of graphene's band structure, with characteristic Dirac cones in the vicinity of high symmetry points K and K' [87]. Given that graphene is a zero-gap semiconductor, for undoped graphene, its Fermi energy lies at the Dirac point, where the two Dirac cones touch. Near these Dirac points, the electronic dispersion has a linear dependence, where expanding Eq. (4.3) around the K, K' points and taking the lowest order term yields,

$$E^{\pm}(\boldsymbol{k}) = \pm\hbar v_F |\boldsymbol{k}|, \tag{4.4}$$

where v_F is the Fermi velocity given by $v_F = \sqrt{3}(\gamma_0 a/2\hbar)$ [85]. As Eq. (4.4) is the

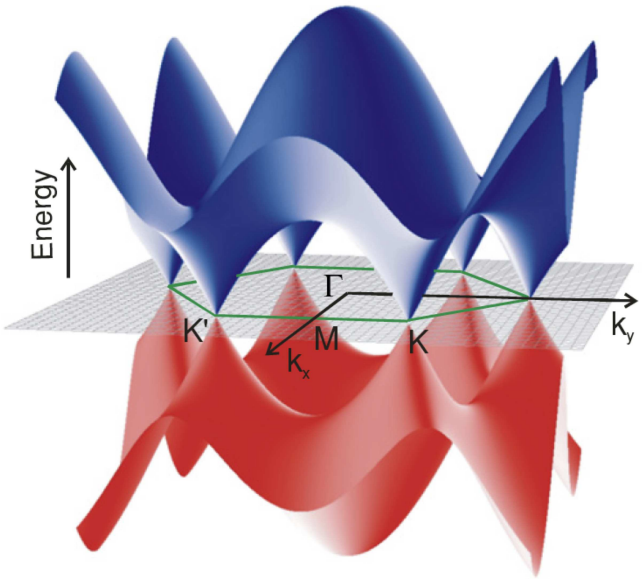

Figure 4.2 : Graphene band structure with characteristic Dirac cones near the K and K' points [87].

solution to the massless Dirac Hamiltonian at the K, K' points:

$$\hat{H} = \hbar v_F \begin{pmatrix} 0 & k_x - ik_y \\ k_x + ik_y & 0 \end{pmatrix} = \hbar v_F (\boldsymbol{\sigma} \cdot \boldsymbol{k}), \tag{4.5}$$

where $\boldsymbol{\sigma}$ are the Pauli matricies, this linear dispersion relation directly implies the relativistic nature of electrons in graphene, and as a result, has produced a variety of exotic properties of 2D Dirac fermions both with DC transport (Chapter 1) and AC infrared properties (refer to Section 4.4).

4.2 Landau quantization

Let us now consider the motion of relativistic charges in graphene when a perpendicular magnetic field is applied. We take a similar approach to Section 2.2 and choose the Landau gauge, $\boldsymbol{A} = Bx\hat{y}$. Using Eq. (4.5) for the effective Hamiltonian

and considering eigenstates of $\hat{H}$, such that

$$\hat{H}\Psi = E\Psi \tag{4.6}$$

$$\hat{H}\begin{pmatrix}\Psi_1\\ \\ \Psi_2\end{pmatrix} = v_F\begin{pmatrix}0 & p_x - ip_y\\ \\ p_x + ip_y & 0\end{pmatrix}\begin{pmatrix}\Psi_1\\ \\ \Psi_2\end{pmatrix} = E\begin{pmatrix}\Psi_1\\ \\ \Psi_2\end{pmatrix} \tag{4.7}$$

$$v_F(p_x - ip_y)\Psi_2 = E\Psi_1 \tag{4.8}$$

$$v_F(p_x + ip_y)\Psi_1 = E\Psi_2, \tag{4.9}$$

we can decouple Ψ_1 and Ψ_2 and get

$$E^2\Psi_2 = v_F^2(p_x + ip_y)(p_x - ip_y)\Psi_2. \tag{4.10}$$

Given the presence of an external magnetic field, we can use the Peierls substitution, $\boldsymbol{p} \to \boldsymbol{p} + e\boldsymbol{A}$, and try to find E for Ψ_2 [88]:

$$\begin{aligned}\frac{E^2}{v_F^2}\Psi_2 &= \left[(\hat{p}_x + eA_x) + i(\hat{p}_y + eA_y)\right]\left[(\hat{p}_x + eA_x) - i(\hat{p}_y + eA_y)\right]\Psi_2\\ &= \left[\hat{p}_x + i(\hat{p}_y + eB\hat{x})\right]\left[\hat{p}_x - i(\hat{p}_y + eB\hat{x})\right]\Psi_2\\ &= \left[\hat{p}_x^2 - i\left[\hat{p}_x,\, \hat{p}_y + eB\hat{x}\right] + (\hat{p}_y + eB\hat{x})^2\right]\Psi_2\\ &= \left[\hat{p}_x^2 - \hbar eB + (\hat{p}_y + eB\hat{x})^2\right]\Psi_2\\ &= \left[\hat{p}_x^2 - \hbar eB + e^2B^2(\hat{x} + x_0)^2\right]\Psi_2,\end{aligned} \tag{4.11}$$

where we let $x_0 = p_y/eB$. Rearranging Equation (4.11),

$$\frac{1}{2m}\left[\frac{E^2}{v_F^2} + \hbar eB\right]\Psi_2 = \left[\frac{\hat{p}_x^2}{2m} + \frac{e^2B^2}{2m}(\hat{x} + x_0)^2\right]\Psi_2, \tag{4.12}$$

we again have a form of the Schrödinger equation on the right side of Equation (4.12) that corresponds to a harmonic oscillator with a shifted center and eigenvalues

$\varepsilon = (n + \frac{1}{2})\hbar\omega_c$, where $\omega_c = eB/m$. As a result, the eigenvalues for our effective Hamiltonian are now

$$\frac{1}{2m}\left[\frac{E^2}{v_F^2} + \hbar eB\right] = \left(n + \frac{1}{2}\right)\frac{\hbar eB}{m}$$

$$\frac{E^2}{v_F^2} = \left(n + \frac{1}{2}\right)(2\hbar eB) - \hbar eB$$

$$\frac{E^2}{v_F^2} = \hbar eB(2n + 1 - 1)$$

$$E = \mathrm{sgn}(n) v_F \sqrt{2\hbar|e|B|n|}. \tag{4.13}$$

Therefore, as we have derived in Equation (4.13), the application of a magnetic field B perpendicular to the plane of graphene creates LLs that can be both positive and negative ($n = 0, \pm1, \pm2$ ...), and unlike typical 2DEG systems like GaAs, graphene's LLs are unequally spaced and have a $\sqrt{B}$-dependence that is a consequence of the linearity of its dispersion relation. Moreover, we also note that there exists an $n = 0$ LL with $E = 0$ regardless of the strength of the magnetic field. The $n = 0$ LL also has a distinctive electron-hole degeneracy, as the levels in $n = 0$ are shared by both electrons and holes, and is responsible for the unusual sequence of the quantum Hall effect in graphene [3, 4, 87].

Let us now calculate the LL degeneracy for graphene. Similar to the procedure in Section 2.2, we first calculate the number of electron wave-vectors with energies

between adjacent LLs in graphene:

$$v_F\hbar|\boldsymbol{k}| = v_F\sqrt{2\hbar|e|B|n|}$$

$$|\boldsymbol{k}|^2 = \frac{2neB}{\hbar} \tag{4.14}$$

Calculating the area between adjacent LLs:

$$A_n = \pi(k_x^2 + k_y^2) = \pi\left(\frac{2neB}{\hbar}\right)$$

$$A_{n+1} = \pi\left(\frac{2(n+1)eB}{\hbar}\right)$$

$$A_{n+1} - A_n = \frac{2\pi eB}{\hbar}. \tag{4.15}$$

and recalling that the number of states per unit area is $(L/2\pi)^2$, we can calculate the total number of states, p, per LL in graphene:

$$p = \left(\frac{L}{2\pi}\right)^2\left(\frac{2\pi eB}{\hbar}\right), \tag{4.16}$$

which results in a $eB/2\pi\hbar$ degeneracy per unit area of each LL ($\times$ 4 for valley and spin degeneracy in graphene). Figure 4.3 compares the band structure, LLs, and LL fan diagram of a traditional 2DEG to graphene.

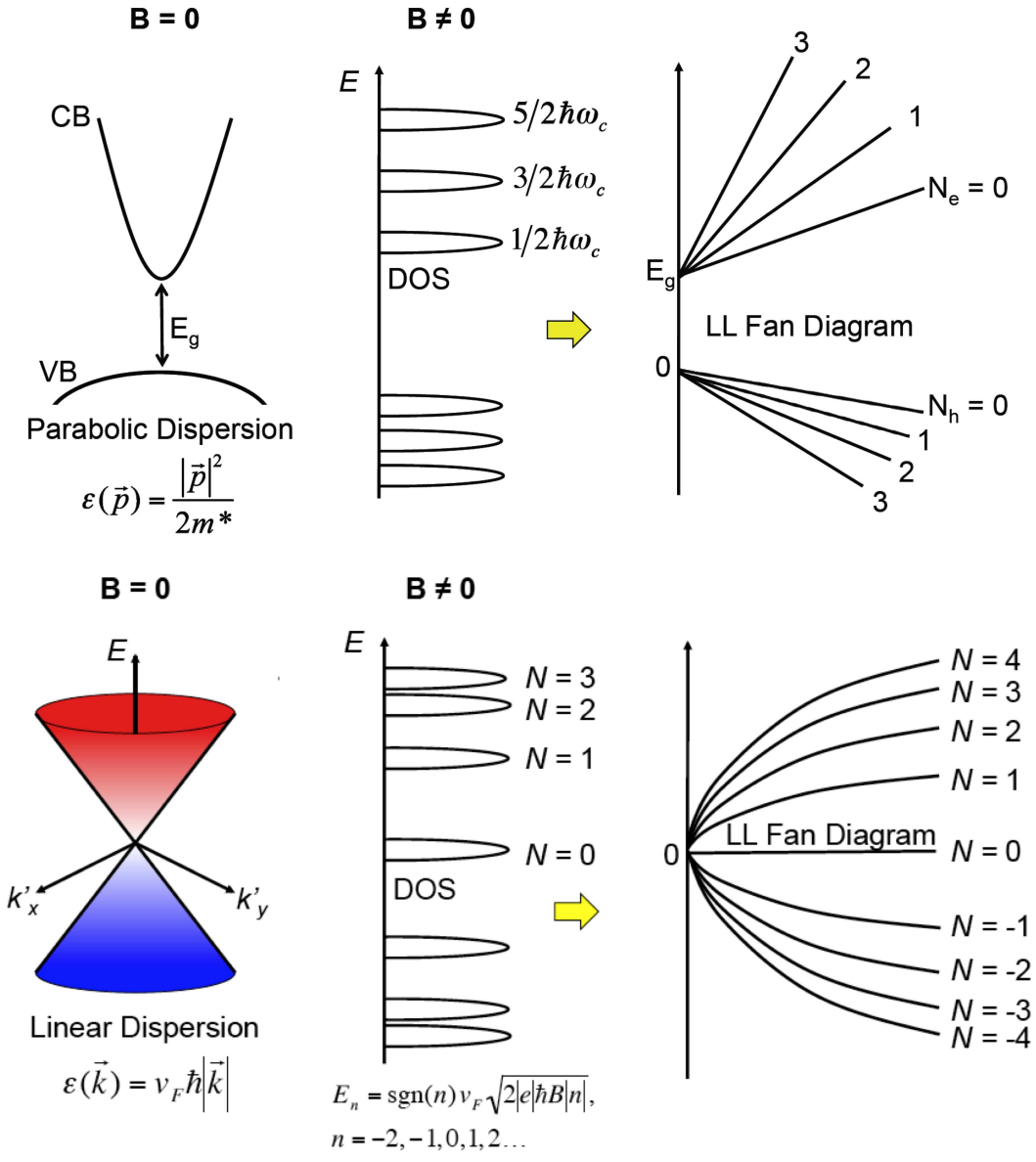

Figure 4.3 : Comparison of band structure, LLs, and LL fan diagram for a traditional 2DEG (top) and graphene (bottom).

4.3 Cyclotron Resonance

We first review the physics of CR in graphene via a semiclassical description, where below we provide a detailed summary of the work by Mikhailov [23]. In the semiclassical description, the equation of motion of a quasiparticle in graphene with spectrum,

$$\mathcal{E}_{\pm}(\boldsymbol{p}) = \pm V|\boldsymbol{p}|, \quad \boldsymbol{p} = (p_x, p_y) \tag{4.17}$$

in a uniform magnetic field $\boldsymbol{B}$=(0, 0, B) and in the presence of an external electric field $\boldsymbol{E}_0(t) = E_0(t)(\cos\omega t, \sin\omega t)$ with radiation frequency ω, is

$$\frac{d\boldsymbol{p}}{dt} = -\frac{e}{c}\boldsymbol{v} \times \boldsymbol{B} - e\boldsymbol{E}(t), \quad \boldsymbol{v} = V\frac{\boldsymbol{p}}{p} \tag{4.18}$$

with initial condition $\boldsymbol{p}|_{t=0} = \boldsymbol{p}_0$. Let us assume the external electric field E_0 is weak such that $\mathcal{F} \equiv eE_0/\omega p_0 \ll 1$ corresponds to the linear response regime where the energy absorbed during the oscillation by the particle is small compared to the particle's average energy.

The cyclotron frequency of a massless particle can be written as $\omega_c(\mathcal{E}) = eBV/pc = eBV^2/\mathcal{E}c$ and the time dependency of the momentum under this CR condition is shown in Figure 4.4. Unlike the results for a massive particle shown in Figure 4.4(a), where the massive particle is always in resonance with the external electric field and the value of its momentum grows linearly with time, the massless particle momentum instead oscillates in time (Figure 4.4(b)). Intially, the massless particle is in resonance with the external field, $\omega = \omega_c = eBV/p_0c$, and its energy grows. However, when $p > p_0$, the massless particle falls out of resonance causing its energy and

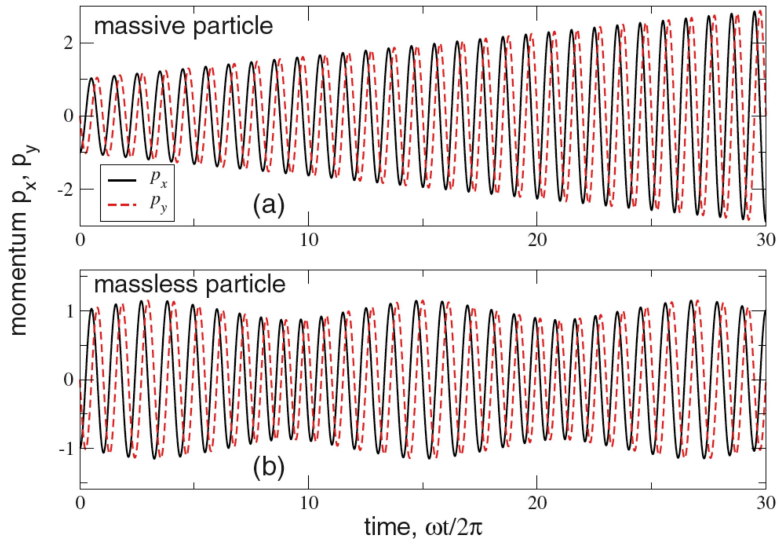

Figure 4.4 : Time dependency of momentum under CR conditions for (a) massive particle and (b) massless particle [23].

momentum to decrease until it enters resonance again.

We can now define this oscillatory behavior of the momentum such that

$$\begin{pmatrix} p_x(t) \\ p_y(t) \end{pmatrix} = p(t) \begin{pmatrix} -\sin[\omega t + \phi(t)] \\ \cos[\omega t + \phi(t)] \end{pmatrix}, \tag{4.19}$$

where $\phi(t)$ is the phase. Equation (4.18) now becomes

$$\dot{p}(t) = eE_0 \sin\phi(t), \tag{4.20}$$

$$p(t)\dot{\phi}(t) = -\omega p(t) + eVB/c + eE_0 \cos\phi(t), \tag{4.21}$$

with initial conditions $p|_{t=0} = p_0$ and $\phi|_{t=0} = \phi_0$. The velocity is then written as

$$\boldsymbol{v}(t) = V\frac{\boldsymbol{p}(t)}{p(t)} = V \begin{pmatrix} -\sin[\omega t + \phi(t)] \\ \cos[\omega t + \phi(t)] \end{pmatrix}. \tag{4.22}$$

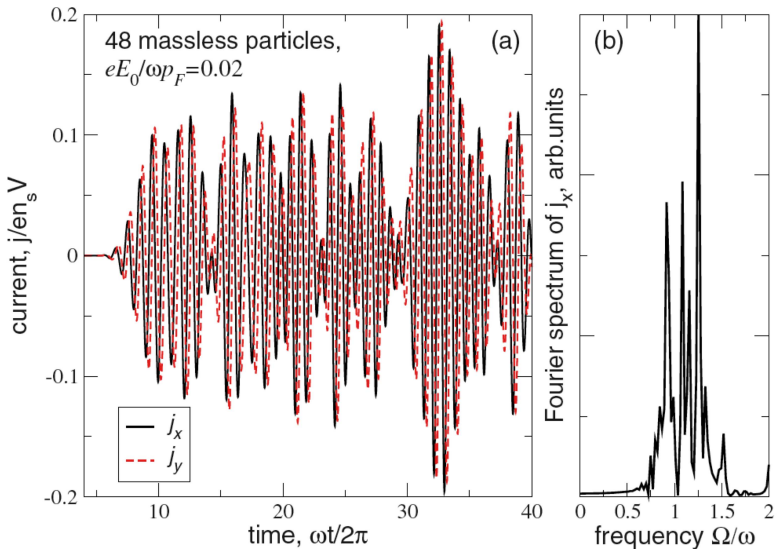

Figure 4.5 : (a) Time dependence of the current in a system of 48 massless particles and (b) the Fourier spectrum of the j_x component of the current [23].

Recalling that $\mathcal{F} \ll 1$, we can solve for the phase $\phi(t)$ analytically by substituting $p(t) = p_0[1 + q(t)]$ with $|q(t)| \ll 1$. We can rewrite Equation (4.20) and (4.21) as

$$\dot{q}(t) = \omega\mathcal{F}\sin\phi, \quad \dot{q}(t) = -\omega q + \omega\mathcal{F}\cos\phi. \tag{4.23}$$

Equation (4.23) reduces to the nonlinear pendulum equation:

$$\ddot{q}(t) = -\omega^2\mathcal{F}\sin\phi. \tag{4.24}$$

If the initial phase $\phi_0 \leq 1$, we get

$$\phi(t) = \phi_0\cos(\omega\sqrt{\mathcal{F}}t), \quad q(t) = \phi_0\sqrt{\mathcal{F}}\sin(\omega\sqrt{\mathcal{F}}t), \tag{4.25}$$

and we can replace Equation (4.25) into Equation (4.22) to calculate the Fourier spectrum of the velocity $\tilde{\boldsymbol{v}}(\Omega) = \int \boldsymbol{v}(t)e^{-i\Omega t}dt/2\pi$.

As graphene is a many-particle system, the electromagnetic response is shown in Figure 4.5 for a system of 48 massless particles, where the Fourier spectrum consists

of many narrow peaks distributed around $\Omega \sim \omega$, which results in a CR peak with a single broad peak. Therefore, from the semiclassical description, graphene behaves like a nonlinear material that, when irradiated by a monochromatic wave, scatters the radiation in a broad frequency, resulting in broad CR absorption peaks.

Next, we review the physics of CR in graphene via a quantum mechanical description, where below we provide the theoretical description given by A. Rustagi and C. J. Stanton (see the Appendix of [89]). Here, we calculate the circular polarization dependence of the cyclotron resonance absorption of graphene in a magnetic field. We use CGS units here as opposed to the text so that we can compare our expressions to others. In addition, we calculate the interband magneto-absorption (i.e., the valence band to conduction band transitions).

The Hamiltonian for graphene near the K point is given by

$$H = \hbar v_F \boldsymbol{\sigma} \cdot \mathbf{k} = \hbar v_F \begin{pmatrix} 0 & k_x - ik_y \\ k_x + ik_y & 0 \end{pmatrix}, \tag{4.26}$$

where v_F is the Fermi velocity (and slope of the linear dispersion), $\boldsymbol{\sigma}$ are the Pauli matrices and $\mathbf{k}$ is wavevector measured from the K point $\mathbf{k} = \mathbf{k_\Gamma} - \mathbf{K}$ ($\mathbf{k_\Gamma}$ is the wavevector measured from the Γ point). The energy eigenvalues for this Hamiltonian are

$$E^{\pm}(\boldsymbol{k}) = \pm \hbar v_F |\mathbf{k}|. \tag{4.27}$$

A similar Hamiltonian $H = \hbar v_F \boldsymbol{\sigma}^* \cdot \mathbf{k}'$ exists at the $\mathbf{K}'$ point, but we will focus only on the K point. In the results for our final expressions, we simply add a factor of four to account for both the spin degeneracy and the $\mathbf{K}, \mathbf{K}'$ degeneracy.

In the presence of an external field (DC magnetic or AC optical), one uses the Peierls substitution $\mathbf{k} \to \mathbf{k} + e\mathbf{A}/\hbar c$ (note the electron charge is $-e$), where A is the vector potential, to yield

$$H = \hbar v_F \boldsymbol{\sigma} \cdot \left(\mathbf{k} + \frac{e\mathbf{A}}{\hbar c} \right). \tag{4.28}$$

To determine the cyclotron resonance and absorption, we will consider the case of both a DC magnetic field and AC optical field so that the Hamiltonian becomes

$$H = \hbar v_F \boldsymbol{\sigma} \cdot \left(\mathbf{k} + \frac{e\mathbf{A}_B}{\hbar c} + \frac{e\mathbf{A}_{\text{opt}}}{\hbar c} \right). \tag{4.29}$$

The magnetic field will be oriented in the $\hat{z}$ direction (perpendicular to the graphene layer), and we will use the Landau gauge in the form

$$\mathbf{A}_B = (0, Bx, 0). \tag{4.30}$$

For the AC optical field, we will take plane waves propagating in the $\hat{z}$ direction (i.e., in the same direction as the magnetic field). The vector potential $\mathbf{A}_{\text{opt}}$ for the photon field can be related to the AC electric field by

$$\mathbf{E}_{\text{opt}} = \mathbf{E}_0 \exp\left[i \left(\mathbf{q} \cdot \mathbf{r} - \omega t \right) \right] \tag{4.31}$$

$$\mathbf{A}_{\text{opt}} = \frac{c\mathbf{E}_0}{i\omega} \exp\left[i \left(\mathbf{q} \cdot \mathbf{r} - \omega t \right) \right]. \tag{4.32}$$

Here $\mathbf{q}$ is in the $\hat{z}$ direction and $\mathbf{E}_0$ can be left or right circularly polarized in the x-y plane. We write the Hamiltonian [Eq. (4.29)] as a sum of an unperturbed term and a perturbation term

$$H = H_B + H^1, \tag{4.33}$$

where H_B is the unperturbed Hamiltonian with only a DC magnetic field. This can be solved exactly by replacing $\mathbf{k}$ with $\hbar\nabla/i$ in Eq. (4.29) and keeping only the

magnetic field term. The spectrum in the absence of the perturbation H^1 is simply the Landau level spectra

$$E_{n,\pm} = \pm\gamma\sqrt{n}, \tag{4.34}$$

where $\gamma = \frac{\sqrt{2}v_F\hbar}{l_B} = v_F\sqrt{\frac{2e\hbar B}{c}}$, $n = 0, 1, 2...$, and the magnetic length, l_B, is given by $l_B = \sqrt{\hbar c/eB}$. Note that the energies vary with $\sqrt{n}$ and also with $\sqrt{B}$ (through the magnetic length). Note also that there is an $n = 0$ level. We can also write Eq. (4.34) in a simplified form

$$E_{n,\pm} = \pm\hbar\omega_0\sqrt{n}\,, \tag{4.35}$$

with $\omega_0 = \sqrt{2}v_F/l_B$ being the characteristic frequency. The wavefunctions are two-component spinors given by

$$\langle x, y \mid n, \pm, k\rangle = \Psi_{n,\pm}(x, y) = b_n \begin{pmatrix} \Phi_{n-1,k} \\ \\ \pm i\ \Phi_{n,k} \end{pmatrix}. \tag{4.36}$$

We treat n as *positive* or *zero* and the $+$ sign corresponds to the positive energy solution and the $-$ sign corresponds to the negative energy solution. The normalization is given by

$$b_n = \begin{cases} 1 & \text{if } n = 0 \\ \\ \frac{1}{\sqrt{2}} & \text{if } n \neq 0 \end{cases} \tag{4.37}$$

and the component functions Φ_n are given by

$$\begin{aligned} \Phi_{n.k} = &\frac{1}{\sqrt{2^n n!\sqrt{\pi}}}\frac{1}{\sqrt{L_y l_B}} e^{i\,k\,y} \exp\left(-\frac{(x - kl_B^2)^2}{2l_B^2}\right) \\ &\times H_n\left(\frac{(x - kl_B^2)}{l_B}\right), \end{aligned} \tag{4.38}$$

with Φ_{-1}=0, H_n being the Hermite Polynomial of order n, and k the quantum number associated with the y motion in the Landau gauge. The wavefunctions in Eq. (4.38) are harmonic oscillator wavefunctions in the x direction and plane waves in the y direction.

We will treat the radiative Hamiltonian H^1 perturbatively using the spinor wavefunctions in Eq. (4.36). The perturbation term is

$$H^1 = v_F \boldsymbol{\sigma} \cdot \left(\frac{e\mathbf{A}_{\text{opt}}}{c} \right) = -\frac{iev_F}{\omega} \exp(i\,\mathbf{q}\cdot\mathbf{r}) \times \begin{pmatrix} 0 & E_x - iE_y \\ E_x + iE_y & 0 \end{pmatrix}. \tag{4.39}$$

This is not the usual $\mathbf{A}\cdot\mathbf{p}$ term that one uses in calculating the optical properties of conventional semiconductors. If we had used the entire Hamiltonian for graphene instead of the Dirac approximation for the $\mathbf{K}$ and $\mathbf{K}'$ points we could have used an $\mathbf{A}\cdot\mathbf{p}$ term in treating this interaction.

The optical matrix element corresponding to a transition caused by the perturbation term (for in-plane polarization, i.e., $\mathbf{q}$ is along the z-direction) from state n to m is calculated to be

$$\langle m,\alpha,k' \mid H^1 \mid n,\beta,k\rangle = -\iint d^2r \frac{i\,e\,v_F}{\omega} e^{(i\,q\,z)} b_m b_n \times (\Phi^*_{m-1,k'}, -\alpha i\Phi^*_{m,k'}) \begin{pmatrix} 0 & E_x - iE_y \\ E_x + iE_y & 0 \end{pmatrix} \begin{pmatrix} \Phi_{n-1,k} \\ \beta i\Phi_{n,k} \end{pmatrix}. \tag{4.40}$$

We note that n and m are ≥ 0 and that $\alpha,\beta = \pm$ depending on whether the state is the positive energy state (conduction band) or the negative energy state (valence

band). Cyclotron resonance absorption corresponds to $\alpha = \beta$ and the inter-band magneto-absorption to $\alpha \neq \beta$.

For positive circularly polarized light $\oplus$, we have $\mathbf{E_0} = E_0(\hat{x} + i\hat{y})/\sqrt{2}$ so that $E_x = E_0/\sqrt{2}$, $E_y = iE_0/\sqrt{2}$ and the matrix element becomes:

$$\langle m, \alpha, k' \mid H^1 \mid n, \beta, k\rangle_{\oplus} = -\iint d^2r \frac{i\ e\ v_F}{\omega} e^{(i\ q\ z)} b_m b_n$$
$$\times(\Phi^*_{m-1,k'}, -\alpha i\Phi^*_{m,k'}) \begin{pmatrix} \beta\ i\sqrt{2}E_0\Phi_{n,k} \\ \\ 0 \end{pmatrix}, \tag{4.41}$$

which integrates to

$$\langle m, \alpha, k' \mid H^1 \mid n, \beta, k\rangle_{\oplus} = \beta \frac{\sqrt{2}E_0\ e\ v_F}{\omega} e^{(i\ q\ z)}$$
$$\times\ b_m\ b_n\ \delta_{m-1,n}\ \delta_{k,k'}. \tag{4.42}$$

Using the Fermi Golden Rule, we can evaluate the transition rate W_{nm} for an electron in state n going to an unoccupied state m, $n \to m$

$$W_{nm} = \frac{2\pi}{\hbar} |\langle m, \alpha, k' \mid H^1 \mid n, \beta, k\rangle|^2 \delta(\hbar\omega - \Delta E^{m,\alpha}_{n,\beta}), \tag{4.43}$$

where $\Delta E^{m,\alpha}_{n,\beta} = E_{m,\alpha} - E_{n,\beta}$. Taking into account the probability $f_{n,\beta}$ that the state (n,β) is occupied and $(1 - f_{m,\alpha})$ that the state (m,α) is unoccupied, the transition rate *per unit volume* is

$$R_{n\to m} = \left(\frac{1}{V}\right) \frac{2\pi}{\hbar} |\langle m, \alpha, k' \mid H^1 \mid n, \beta, k\rangle|^2$$
$$\times\ f_{n,\beta}(1 - f_{m,\alpha})\delta(\hbar\omega - \Delta E^{m,\alpha}_{n,\beta}). \tag{4.44}$$

We must also take into account the inverse process (through emission of a photon), $m \to n$. The transition rate per unit volume is given by

$$R_{m\to n} = \left(\frac{1}{V}\right)\frac{2\pi}{\hbar}|\langle n,\beta,k' \mid H^1 \mid m,\alpha,k\rangle|^2$$
$$\times f_{m,\alpha}(1-f_{n,\beta})\delta(-\hbar\omega + \Delta E^{m,\alpha}_{n,\beta}). \tag{4.45}$$

The total *net* rate/volume is the difference between the two,

$$\begin{aligned} R_{nm} &= R_{n\to m} - R_{m\to n} \\ &= \left(\frac{1}{V}\right)\frac{2\pi}{\hbar}|\langle m,\alpha,k' \mid H^1 \mid n,\beta,k\rangle|^2 \\ &\quad \times (f_{n,\beta} - f_{m,\alpha})\delta(\hbar\omega - \Delta E^{m,\alpha}_{n,\beta}). \end{aligned} \tag{4.46}$$

For undoped systems at T= 0, $f_{m,-} = 1$ and $f_{m,+} = 0$ for $m > 0$, i.e., all conduction band states are empty and all valence bands states are occupied, while $f_{0,-} = f_{0,+} = 1/2$.

For positive circular polarized light,

$$R^{\oplus}_{mn} = \frac{4\pi e^2 v_F^2}{V\hbar\omega^2}E_0^2 b_m^2 b_n^2$$
$$\times (f_{n,\beta} - f_{m,\alpha})\delta_{m-1,n}\delta_{k,k'}\delta(\hbar\omega - \Delta E^{m,\alpha}_{n,\beta}). \tag{4.47}$$

The total transition rate $R^{\oplus}$ summed over all possible transitions is

$$\begin{aligned} R^{\oplus}_{mn} &= \frac{4}{V}\sum_{\substack{m,n\\ \alpha,\beta}}\sum_{k,k'}\frac{4\pi e^2 v_F^2}{\hbar\omega^2}E_0^2 b_m^2 b_n^2\left[\delta_{m-1,n}\,\delta_{k,k'}\right]^2 \\ &\qquad \times (f_{n,\beta} - f_{m,\alpha})\delta(\hbar\omega - \Delta E^{m,\alpha}_{n,\beta}) \\ &= \frac{4}{V}\sum_{\substack{n\geq 0\\ \alpha,\beta}}\sum_{k}\frac{2\pi e^2 v_F^2}{\hbar\omega^2}E_0^2 b_n^2 \\ &\qquad \times (f_{n,\beta} - f_{n+1,\alpha})\delta(\hbar\omega - \Delta E^{n+1,\alpha}_{n,\beta}). \end{aligned} \tag{4.48}$$

The factor of four comes from the two-fold spin degeneracy and the two-fold valley degeneracy. Since the Landau levels are shifted harmonic oscillators in the x direction centered about

$$x_0 = kl_B^2 \tag{4.49}$$

and since the oscillator center should be within the sample, following Roth [90], we require that

$$0 < x_0 < L_x \Rightarrow 0 < k < L_x/l_B^2. \tag{4.50}$$

This restricts the allowed values of k. Converting the sum over k into an integral

$$\sum_k \rightarrow \int_0^{k_{max}} \frac{L_y}{2\pi} dk = \frac{L_y L_x}{2\pi l_B^2}, \tag{4.51}$$

it follows that

$$\begin{aligned} R^{\oplus} &= \frac{4}{L_z} \sum_{\substack{n\geq 0 \\ \alpha,\beta}} \frac{e^2 v_F^2}{\hbar\omega^2 l_B^2} E_0^2 b_n^2 \\ &\times (f_{n,\beta} - f_{n+1,\alpha}) \delta(\hbar\omega - \Delta E_{n,\beta}^{n+1,\alpha}), \end{aligned} \tag{4.52}$$

where L_z is the thickness of the graphene layer. The total power loss per unit volume is

$$\begin{aligned} P_L^{\oplus} &= R^{\oplus}\hbar\omega = \frac{4}{L_z} \sum_{\substack{n\geq 0 \\ \alpha,\beta}} \frac{e^2 v_F^2}{\omega l_B^2} E_0^2 b_n^2 \\ &\times (f_{n,\beta} - f_{n+1,\alpha}) \delta(\hbar\omega - \Delta E_{n,\beta}^{n+1,\alpha}). \end{aligned} \tag{4.53}$$

The absorption coefficient, α_{abs}, is defined to be [91]

$$\begin{aligned} \alpha_{abs} &= \frac{\#\text{ of photons absorbed/unit volume} \times \text{second}}{\#\text{ of photons injected/unit area} \times \text{second}} \\ &= \frac{R}{S/\hbar\omega} = \frac{R\hbar\omega}{S}, \end{aligned} \tag{4.54}$$

where S is the magnitude of the average Poynting vector:

$$S = |\langle \mathbf{S}(\boldsymbol{r}, t)\rangle| = \frac{n_r c E_0^2}{8\pi}. \tag{4.55}$$

Therefore, for positive circularly polarized light,

$$\begin{aligned}\alpha_{abs}^{\oplus} &= 4 \sum_{\substack{n\geq 0 \\ \alpha,\beta}} \frac{8\pi e^2 v_F^2}{L_z \omega l_B^2 n_r c} b_n^2 \\ &\times (f_{n,\beta} - f_{n+1,\alpha}) \delta(\hbar\omega - \Delta E_{n,\beta}^{n+1,\alpha}).\end{aligned} \tag{4.56}$$

We will set $L_z = 1$ to get the *dimensionless* absorption per graphene layer. For cyclotron resonance, $\alpha = \beta$, and for positive circularly polarized light, the requirement that

$$\hbar\omega = \Delta E_{n,\beta}^{n+1,\beta} = \gamma\left(\beta\sqrt{n+1} - \beta\sqrt{n}\right) > 0 \tag{4.57}$$

restricts the cyclotron resonance transitions to the electron ($\beta = +$) Landau levels and yields:

$$\begin{aligned}\alpha_{abs}^{\oplus} &= \frac{16\pi e^2 v_F^2 \hbar}{n_r c l_B^2} \sum_{n\geq 0} \frac{2 b_n^2}{\gamma\left(\sqrt{n+1} - \sqrt{n}\right)} \\ &\times (f_{n,+} - f_{n+1,+}) \delta(\hbar\omega - \Delta E_{n,+}^{n+1,+}).\end{aligned} \tag{4.58}$$

If we account for scattering which results in linewidth broadening, we can replace the delta function by a Lorentzian:

$$\begin{aligned}\delta(\hbar\omega - \Delta E_{n,\beta}^{n+1,\alpha}) &\to \frac{1}{\pi} \frac{\hbar\tau^{-1}}{(\hbar\omega - \Delta E_{n,\beta}^{n+1,\alpha})^2 + (\hbar\tau^{-1})^2} \\ &= \frac{1}{\pi} \frac{\hbar\tau^{-1}}{(\hbar\omega - \gamma\alpha\sqrt{n+1} + \gamma\beta\sqrt{n})^2 + (\hbar\tau^{-1})^2},\end{aligned} \tag{4.59}$$

yielding the expression:

$$\alpha_{abs}^{\oplus} = \frac{16\pi e^2 v_F^2 \hbar}{n_r c l_B^2 \gamma^2} \sum_{n\geq 0} \frac{2b_n^2}{\left(\sqrt{n+1}-\sqrt{n}\right)} (f_{n,+} - f_{n+1,+}) \times \frac{\frac{\gamma\tau}{\pi\hbar}}{\frac{\gamma^2\tau^2}{\hbar^2}\left(\frac{\hbar\omega}{\gamma} - \sqrt{n+1} + \sqrt{n}\right)^2 + 1}. \tag{4.60}$$

This expression agrees with the results of Abergel and Fal'ko[18] (up to spin and valley degeneracy), who obtained these results using the Keldysh technique.

From Eq. (4.58), we see that the strength of the transitions depend upon $\sqrt{B}$. A factor of B comes from the $1/l_B^2$ term (which comes from the degeneracy of the Landau levels) and a factor of $1/\sqrt{B}$ comes from the $1/\omega$ dependence of Eq.(4.53) at the ω=$\omega_0\sqrt{n}$ resonance.

For cyclotron resonance ($\alpha = \beta$) with negatively circularly polarized light, the relation between energy of the photon and Landau levels

$$\hbar\omega = \Delta E_{n,\beta}^{n-1,\beta} = \gamma\left(\beta\sqrt{n-1} - \beta\sqrt{n}\right) > 0 \tag{4.61}$$

requires that $\beta = -$, i.e., only valence band transitions are allowed. One can repeat the calculation for the cyclotron resonance for negative circularly polarized light in a similar manner to obtain:

$$\alpha_{abs}^{-} = \frac{16\pi e^2 v_F^2 \hbar}{n_r c l_B^2} \sum_{n\geq 1} \frac{2b_{n-1}^2}{\gamma\left(\sqrt{n}-\sqrt{n-1}\right)} \times (f_{n,-} - f_{n-1,-})\delta(\hbar\omega - \Delta E_{n,-}^{n-1,-}), \tag{4.62}$$

To obtain the inter-band magneto-absorption (valence band to conduction band),

we use $\alpha \neq \beta$ and worry only about absorption (not emission) to get:

$$\alpha^{\oplus}_{abs} = \frac{16\pi e^2 v_F^2 \hbar}{n_r c l_B^2} \sum_{n\geq 1} \frac{2b_n^2}{\gamma\left(\sqrt{n+1}+\sqrt{n}\right)} \times (f_{n,-} - f_{n+1,+})\delta(\hbar\omega - \Delta E^{n+1,+}_{n,-}), \tag{4.63}$$

and

$$\alpha^{-}_{abs} = \frac{16\pi e^2 v_F^2 \hbar}{n_r c l_B^2} \sum_{n\geq 1} \frac{2b_{n-1}^2}{\gamma\left(\sqrt{n}+\sqrt{n-1}\right)} \times (f_{n,-} - f_{n-1,+})\delta(\hbar\omega - \Delta E^{n-1,+}_{n,-}). \tag{4.64}$$

Note that the usual $\Delta n = 0$ selection rule for the inter-band magneto-absorption now becomes $\Delta n = \pm 1$ depending on the circular polarization.

4.4 Previous Magneto-Optical Results

In this section, we review the previous experimental results on the magneto-optical properties of graphene. We begin with the work by M. L. Sadowski *et al.* and their investigation of magneto-spectroscopy of ultrathin epitaxial graphite layers to probe the dependence of the energy of electrons in graphene on their momentum [2]. Far-infrared transmission of the graphene samples in the Faraday geometry was measured at T =1.9 K as a function of magnetic field.

Figure 4.6(a) shows the relative transmission trace at 0.4 T with four distinct absorption lines in the spectra that are assigned A: $L_1 \rightarrow L_2$, B: $L_0 \rightarrow L_1$ ($L_{-1} \rightarrow L_0$), C: $L_{-2} \rightarrow L_1$ ($L_{-1} \rightarrow L_2$), D: $L_{-3} \rightarrow L_2$ ($L_{-2} \rightarrow L_3$). Figure 4.6(b) plots the observed transitions along with their assignments as a function of $\sqrt{B}$ and from the straight line fit to the data, they immediately conclude that the measured optical

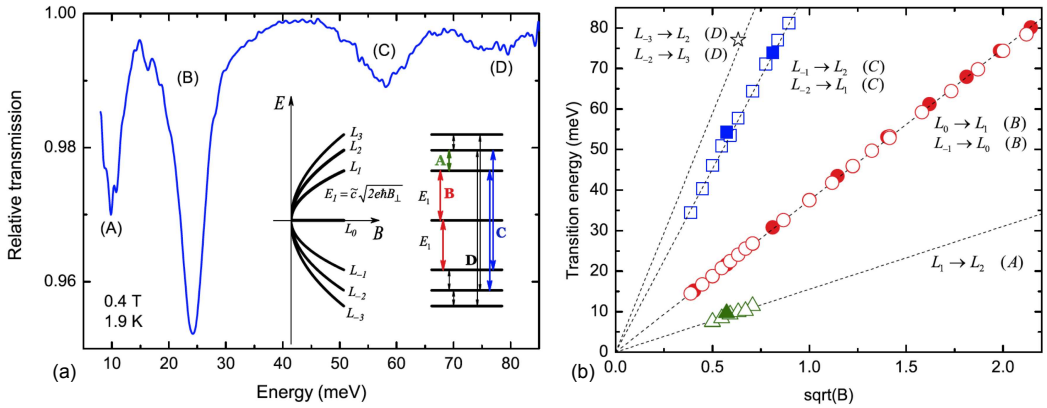

Figure 4.6 : (a)Relative transmission trace at 0.4 T and 1.9 K shows four distinct transitions with their possibly optical transitions in the insert. (b)The observed transitions as a function of the $\sqrt{B}$. The dashed lines are calculated using the same characteristic velocity [2].

excitation spectrum corresponds to that of relativistic Dirac fermions with cyclotron resonance like electron-hole transitions based on the model of noninteracting particles with linear dispersion, where $E = \mathrm{sgn}(n)v_F\sqrt{2\hbar|e|B|n|}$. Moreover, the straight-line fit for all transitions yield the same characteristic velocity of $v_F = 1.03\times10^6$m/s that has been confirmed in previous transport measurements [3, 4].

Similarly, Z. Jiang *et al.* reported IR studies on the LL transitions in graphene up to 18 T and confirmed the $\sqrt{B}$ behavior and deduced band velocity of $v_F = 1.1\times10^6$m/s [24]. Moreover, as they recorded IR transmission spectra at a fixed B at two different carrier concentrations of their graphene samples deposited onto lightly doped Si/SiO_2 substrates, they ultimately probed at two different inter-LL filling, i.e., ν=−2 and ν=−10. As shown in Figure 4.7(a), two LL resonances, T_1 and T_2 are observed for three different magnetic fields, and fitting the transmission minima to Lorentzians, they plotted transition energies of T_1 and T_2 as a function of $\sqrt{B}$ in

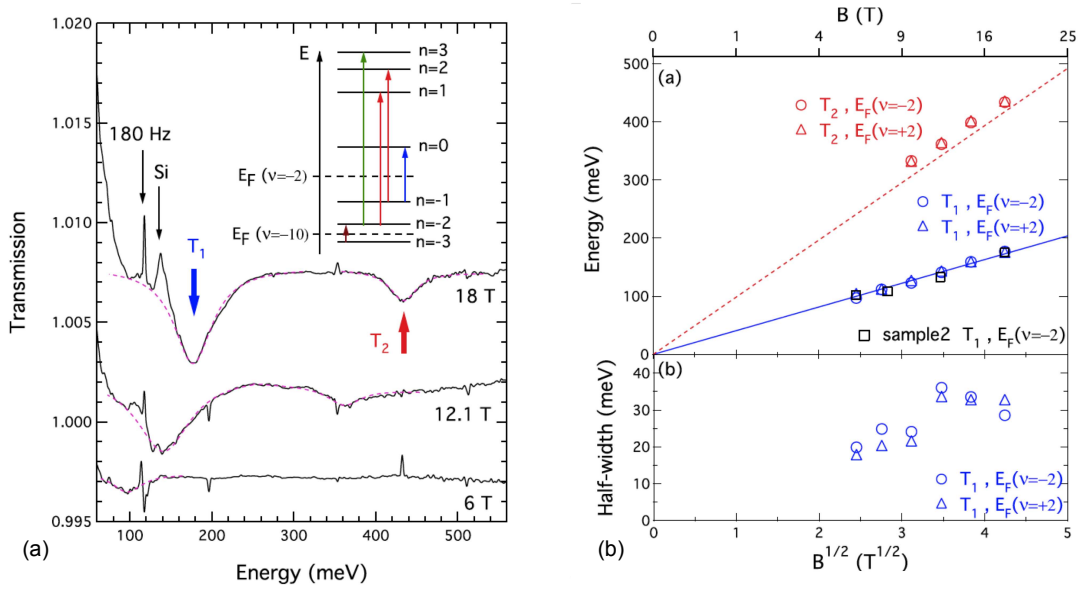

Figure 4.7 : (a) Normalized IR absorption spectra of holes in graphene at three different magnetic fields with two resonances denoted by T_1 and T_2. (b) Resonance energies vs $\sqrt{B}$ from holes. The solid line is a best $\sqrt{B}$ fit to the T_1 transition, while the dashed line is a scaling of the solid line by $\sqrt{2}+1$ [24].

Figure 4.7(b). The clear $\sqrt{B}$ dependence is confirmed. However, when individually fitting T_1 and T_2 to $\sqrt{B}$ fits, it results in differing values for the band velocity v_F deduced from different LLs. The discrepancy indicates a possible contribution from many-particle interactions to the LL transitions.

Discrepancies in the velocities for electron and hole bands were observed by Deacon *et al.* when they investigated CR detected through the photoconductive response from a multiply contacted monolayer sample of graphene [25]. Figure 4.8 shows sequences of the electron-like and hole-like transitions via the photoconductive response as a function of $\sqrt{B}$ with the carrier density scanned to maintain a particular filling factor. The resonances are fitted with Lorentzian lineshapes and are plotted as a

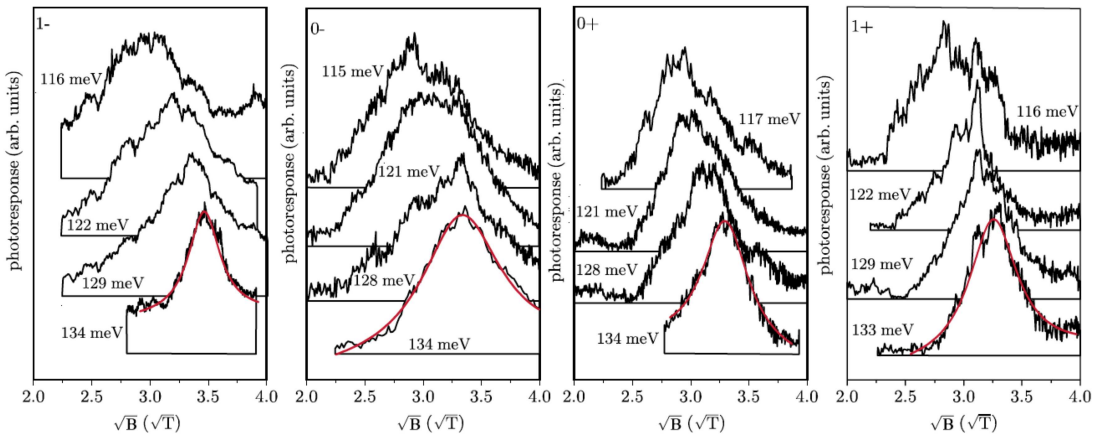

Figure 4.8 : Photoconductive repsonse as a function of $\sqrt{B}$ with carrier densities scanned to keep occupancies at the indicated v [25].

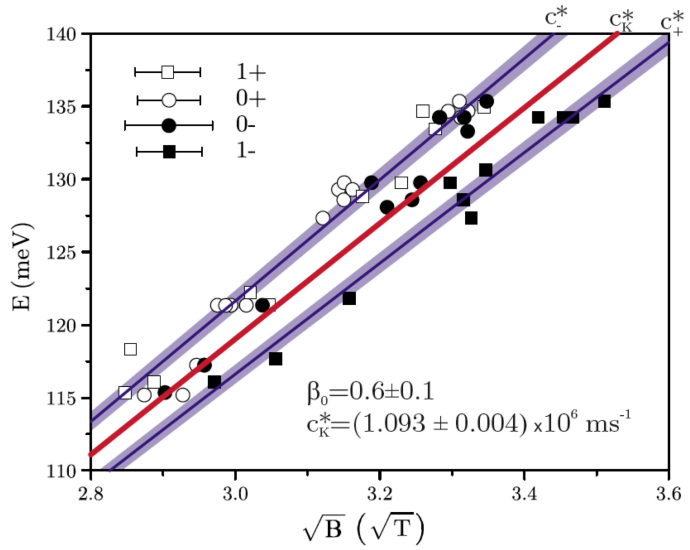

Figure 4.9 : Resonance positions as a function of $\sqrt{B}$, together with the uncertainity in the fitted value for the band velocities [25].

function of $\sqrt{B}$ in Figure 4.9. From the LL energy, a single value of the band velocity is expected, but Figure 4.9 shows otherwise. In particular, resonances measured for 1− and 1+ occupancies show the lowest and highest values for the velocity, which correspond to the hole-like and electron-like transitions. Calculating the band velocity through nearest-neighbor tight binding theory seems to give good agreement with the experimental value, but it does not accurately account for the magnitude of the asymmetry between the electron and hole velocities. Many-body corrections are suggested as a possibility for the magnitude of the asymmetry of the velocities, but the authors conclude that there is still considerable uncertainty in understanding the band structure of graphene.

Orlita *et al.* investigated multilayer epitaxial graphene using far-infrared transmission, shown in Figure 4.10, as a function of magnetic field at $T = 2$ K [37]. They identify four absorption lines (shown in the inset) and evaluate the band velocity to find good agreement with the single-particle theory. Furthermore, although the sample has over 100 layers, there are no transitions that are characteristic of bulk graphite. For the $L_{0(-1)} \rightarrow L_{1(0)}$ transitions, they observe no deviations from the $\sqrt{B}$ scaling even down to ∼40 mT, which allowed them to probe states in the vicinity of the Dirac point. Figure 4.10(c) shows the Lorentzian fitting results as a function of $\sqrt{B}$, where both the peak area and position show a linear increase with $\sqrt{B}$ and the linewidth begins evolving sublinearly as a function of $\sqrt{B}$ at ∼8 meV and 1 T. The authors discuss that short range scatters could cause a $\sqrt{B}$-broadening of the LLs, as suggested by Shon and Ando [92].

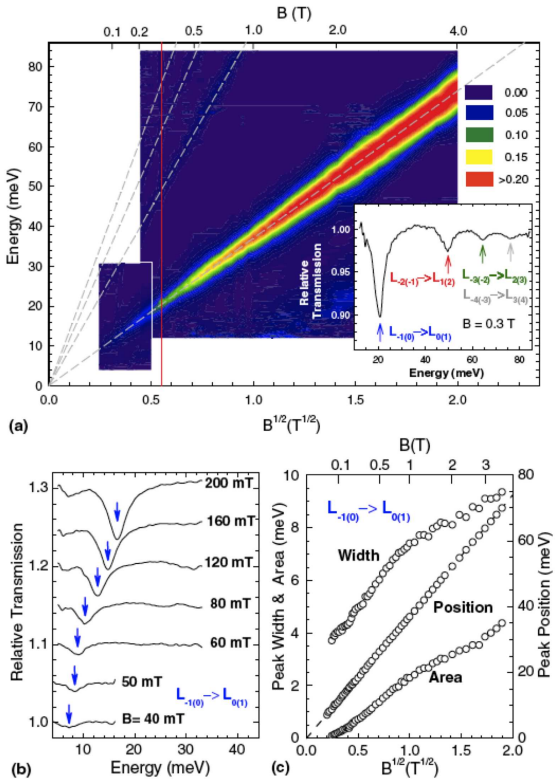

Figure 4.10 : (a) FIR transmission as a function of magnetic field at $T = 2$ K. (b) FIR transmission at low magnetic fields. (c) The peak area, position, and width for the $L_{0(-1)} \rightarrow L_{1(0)}$ [37].

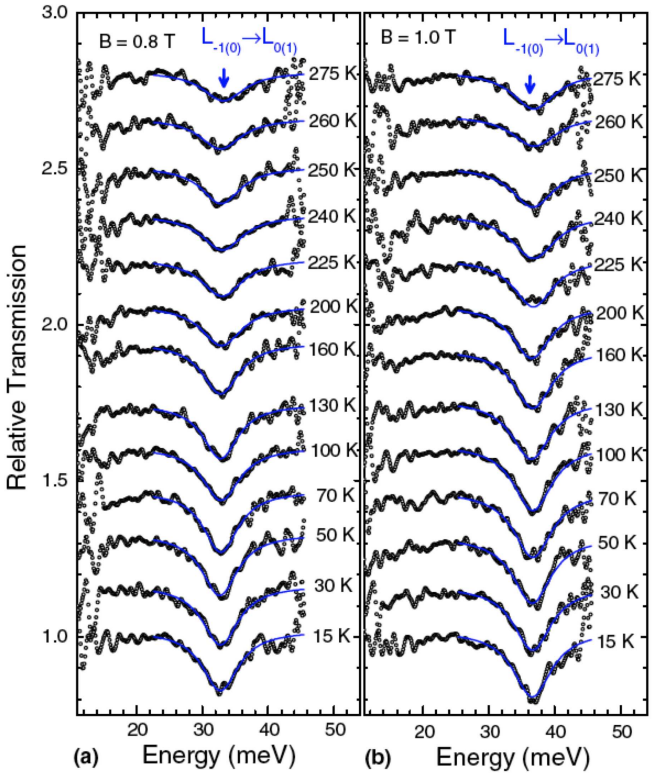

Figure 4.11 : Temperature dependence of the transmission spectra for $B = 0.8$ T and $B = 1.0$ T [37].

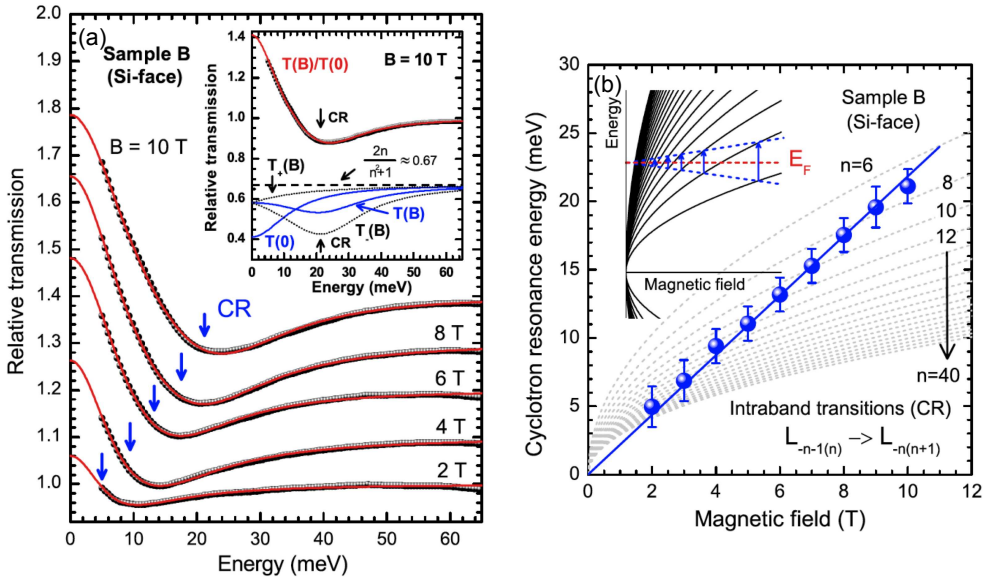

Figure 4.12 : (a) Transmission spectra at various magnetic fields in the quasiclassical regime (b) Position of the CR extracted from fitting the experimental curves that follow linear dependence in B [39].

Figure 4.11 plots the temperature dependence of the transmission spectra showing that well-defined LLs in graphene are still observed at room temperature and for magnetic fields as low as 1 T. Moreover, the resonance peak position is constant with temperature, which shows that the band velocity is temperature independent.

Witowski *et al.* investigated CR in highly doped multilayer epitaxial graphene using IR magneto-transmission to study the quasiclassical response of graphene, where CR-like response is expected to evolve linearly with applied magnetic field [39]. Their highly doped graphene sample was prepared on the Si-terminated surface of SiC, and the transmission spectra taken at various magnetic fields in the FIR is shown in Figure 4.12(a). Here, a magnetic field-induced transmission at low energies accompanied by a wide absorption minimum that moves linearly with increasing

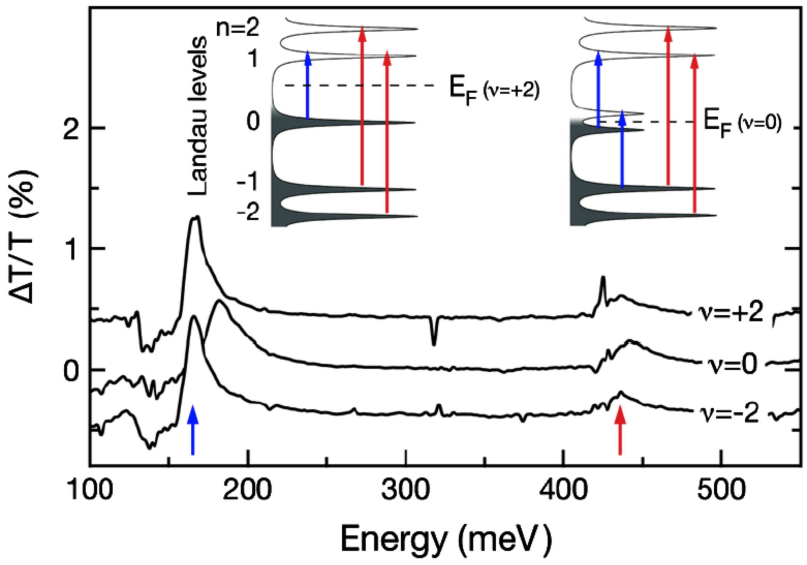

Figure 4.13 : Two CR peaks at $B = 18$ T with filling factor ν=$\pm$2, 0 indicate upshift in CR energy for ν=0 [35].

magnetic field was observed. As this sample is highly doped by charge transfer of the substrate, LLs around the Fermi level are not resolved with magnetic field of a few tesla and the system remains in the quasiclassical regime.

Figure 4.12(b) shows that the position of the CR moves linearly in magnetic field and for comparison, includes an inset depicting positions of the CR transitions between LLs with higher indicies that evolve linearly with magnetic field, despite the fact that individual LLs exactly follow the $\sqrt{B}$ dependence.

Finally, let us discuss the work of Henriksen *et al.*, where they investigated CR transitions to and from the $n = 0$ LL in graphene and observed an interaction-induced shift of the CR transition energy as a function of LL filling factor [35]. Figure 4.13 plots the CR data for filling factors $\nu = \pm 2$, 0 in monolayer graphene exfoliated from Kish graphite onto Si/SiO_2 wafer substrate, where, compared to the smaller

shift for the interband peak at 440 meV, the lower energy peaks at 165-180 meV show a strong upshift of $\sim$8% in energy at $\nu = 0$. The authors discuss possible origins for the observed CR shift at $\nu = 0$ that suggest the opening of an interaction-induced gap in the bulk of the graphene at $\nu = 0$, as depicted in the left and right insets of Figure 4.13.

Chapter 5

Experimental Procedures

5.1 Sample preparation

For this work, we measured cyclotron resonance on large-area graphene samples grown via chemical vapor deposition (CVD), provided by the Tour group at Rice University [89, 93]. To prepare the graphene sample, a 4 cm^2 copper foil was placed on a fused quartz tube furnace that was annealed to 1000°C for 30 mins with H_2 gas flow [93]. After annealing, the addition of CH_4 gas for 6-8 mins completed the growth period and the copper foil was allowed to cool to room temperature.

A poly (methyl methacrylate) (PMMA) film was then spin-coated onto the graphene-covered copper foil and was heated up to 60°C for 5 min to cure the PMMA film. Once cured, the PMMA/ graphene layer was separated from the copper foil by etching in a 1 M $CuCl_2$/6 M HCl aqueous solution and was placed on the surface of Milli-Q water to remove any water-soluable residues [93]. The PMMA/ graphene film was then transferred onto a thallium bromoiodide (KRS-5) substrate that is transparent at mid-infrared wavelengths (Figure 5.1). The PMMA film was finally dissolved away by soaking the substrate in acetone for 8 hours, leaving only the CVD-graphene sheets remaining on the KRS-5 substrate [93].

The scope of this work also involved annealing the graphene samples to investigate

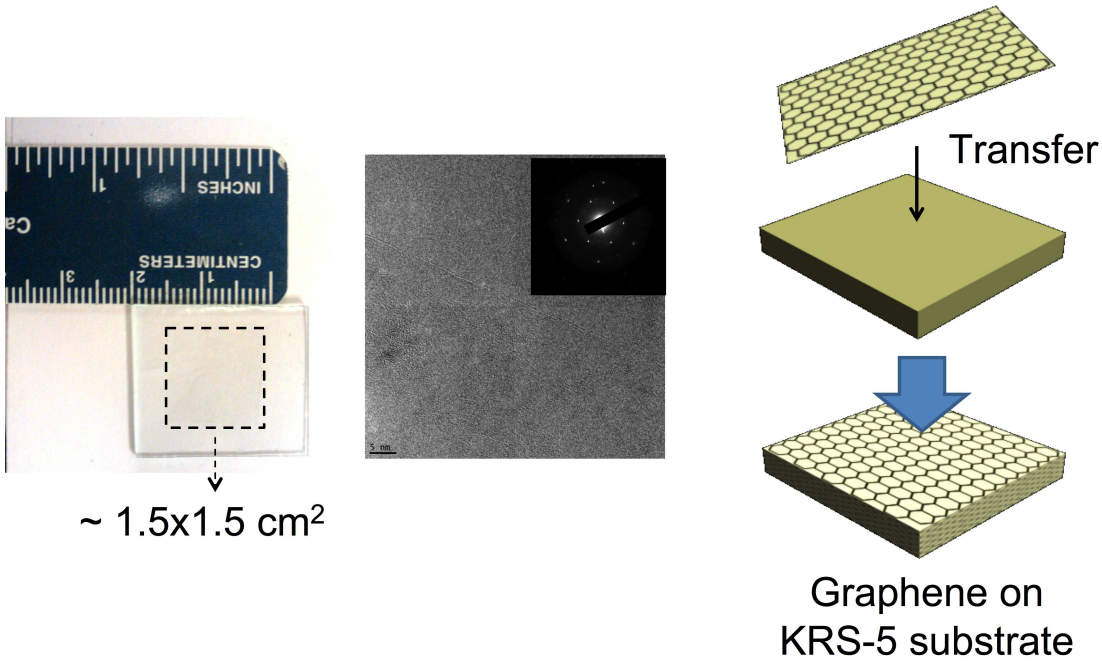

Figure 5.1 : CVD-grown large-area graphene and the transfer to a KRS-5 substrate. Courtesy of L. Ren

the role of accidental chemical doping through physisorption of H_2O and O_2. The experimental parameters for annealing graphene was 2 hours at 150°C and 10^{-6} mbar to remove any physisorbed molecules.

5.2 NHMFL single-turn coil

For all experimental details reported in this section, we refer to Mielke *et al.* and corresponding references [78, 94, 95]. The NHMFL-Los Alamos Single Turn Coil (STC) system was initially commissioned to investigate metallic plutonium and other actinides in extremely high magnetic fields. As a result, the STC system was designed differently from other megagauss facilities in order to safely study hazardous samples at megagauss fields.

Figure 5.2 : The NHMFL-Los Alamos Megagauss Facility [95].

The NHMFL-Los Alamos Megagauss facility is pictured in Figure 5.2. On the right side of the figure, the 300-T STC system includes a capacitor bank above a reinforced steel containment tank that houses the single turn coil and an air filtration intake unit to completely contain all blast debris after each shot.

Figure 5.3 shows a simplified circuitry schematic of the capacitor bank, which consists of 24 individually switched capacitors each with a 6-μF capacitance. Connected to a high voltage power supply (60 kV max operating voltage), standard operation of the STC to 170 T requires 35 kV energy storage capacitor charge. A triggering system for the 24 spark gap switches employs a charged cable type system (Figure 5.4), where 24 individual RG-8/U coaxial cables are charged to a nominal

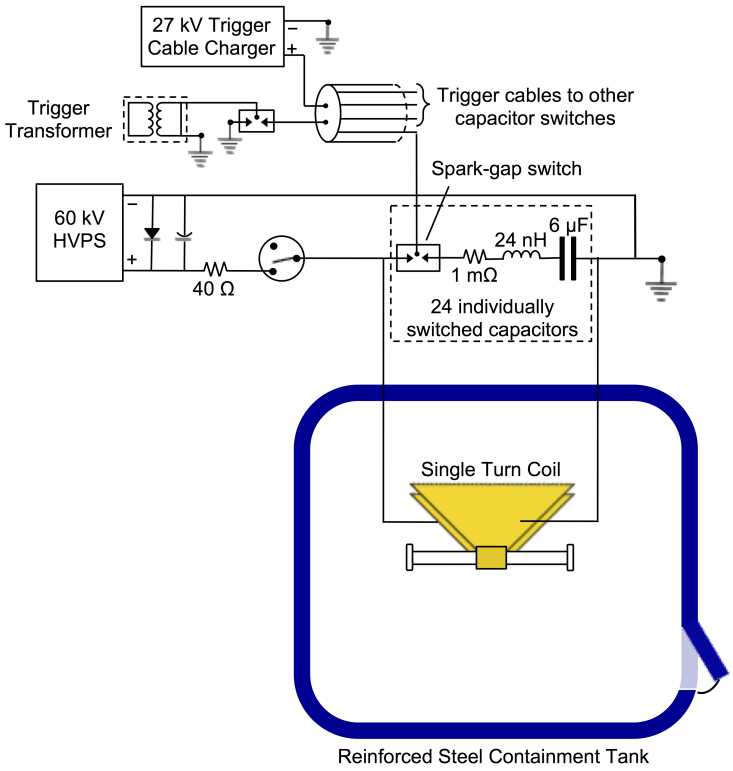

Figure 5.3 : Circuitry schematic of STC. A 60 kV high voltage power supply (HVPS) charges 24 capacitors and a 27 kV trigger system triggers the spark-gap switches to fire the capacitor bank into the single-turn coil.

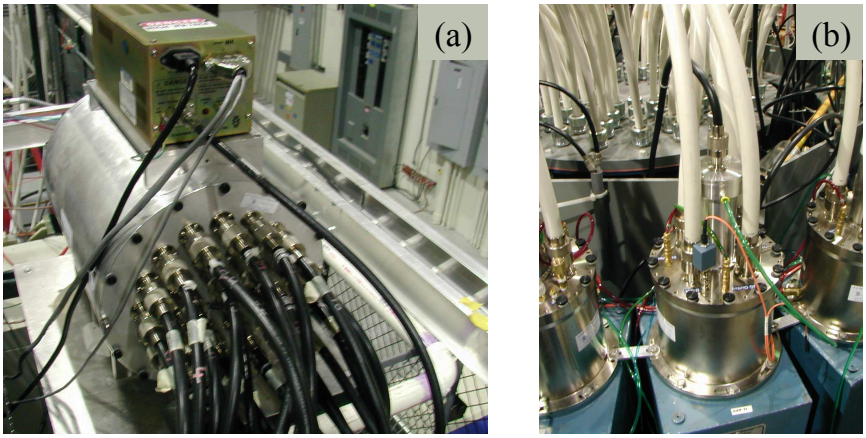

Figure 5.4 : (a) 24 trigger cables connected to 27 kV trigger power supply and transformer. (b) Trigger cable (black) inserted into the spark-gap of the capacitor. Four RG-1417 cables (white) are sent from each capacitor to the collector bus inside the containment tank. Courtesy of C. H. Mielke.

27 kV. Closing a single spark gap switch subsequently shorts each of these 6 m long trigger cables and causes the voltage to collapse to zero. As the voltage collapse is limited by the speed of light traveling in the polyethylene material of the cable, a 7-ns traveling trigger signal wave delivers -27 kV to the Molybdenum trigger pin in the spark gap. This fast voltage reversal results in a transient electric field that adds to the electric field sustained across the energy storage capacitor and the switch electrode, which causes the spark gap switch to break down with sub-ns simultaneity.

Figure 5.5(a) details a CAD drawing of the STC machine inside the containment tank. 96 coaxial pulsed cables (four RG-1417 from each switch) are connected to a 1.22 m wide, 50 mm thick aluminum collector bus, with a solid 4.75 mm thick chlorinated polyvinyl chloride (CPCV) dielectric sheet. The rear of the collector bus consists of a 4-nH snubber network as a precautionary fixture in the event of the

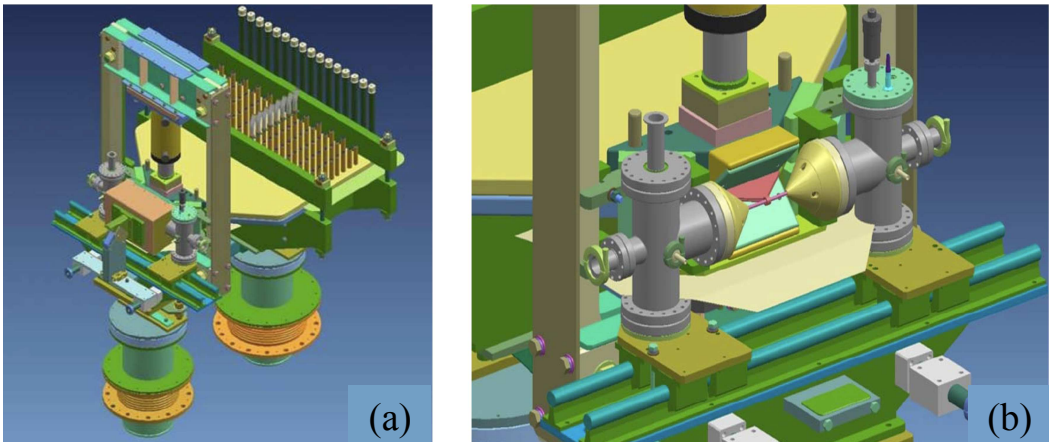

Figure 5.5 : (a) CAD drawing of collector bus with 96 cables attached to it. (b) STC mounting system with 100-ton hydraulic press to clamp the coil into the front assembly [95].

capacitor bank firing into an open circuit. As the collector bus tapers in width down to 0.23 m, the aluminum material of the collector bus transitions to a stiffer A36 steel nose-piece of the lower front-end assembly of the STC mounting system. As shown in Figure 5.5(b), an upper front-end assembly consisting of two interlocking A36 steel nose-pieces clamp the single-turn magnet coil (10 × 10 × 3.2 mm) via a 100-ton hydraulic press. For standard 170 T shots, nominally 50 tons is required, whereas lower field shots from 10 T to 20 T only require nominally 20 tons. A one time use 3.2 mm diameter Cu gasket is embedded in the interlocking nosepieces and establishes an electrical contact line with the coil. This Cu gasket must be replaced before each shot.

The coil is folded from a bow-tie shaped Cu plate, as shown in Figure 5.6. Three layers of mylar insulating sheets are placed inside the coil to avoid arcing between the coil plates during operation of the shot, which surrounds a fiber-glass tube that pro-

Figure 5.6 : STC coil folded from a bow-tie shaped Cu plate. Appropriate dies are used to shape the coil during the folding process. Courtesy of C. H. Mielke.

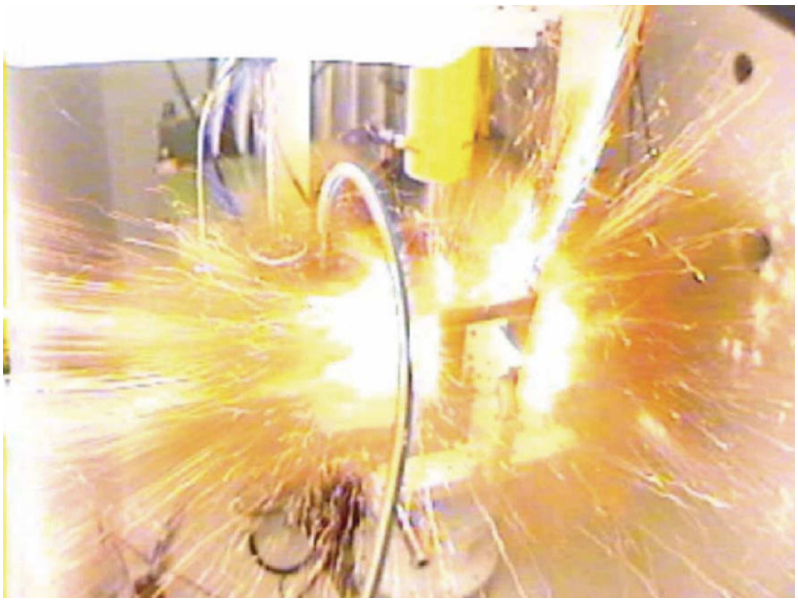

Figure 5.7 : Real-time movie still of arc blast that is deflected away via the flak deflection system from the sample during the experiment [95].

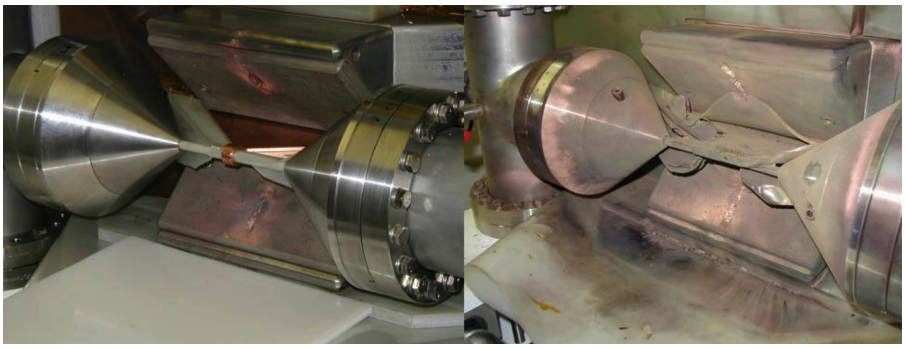

Figure 5.8 : The STC before and after a 35 kV, 175 T shot. Due to the radial nature of the explosion, the coil is destroyed while the sample and probe survive [94].

tects the pick-up coil and probe from any blast debris during the shot (Figure 5.11).

Before firing the STC system for experiments, a flak deflection system that surrounds the coil and probe fixture is mounted on the force axis of the coil to divert arc blasts and coil fragments away from the sample and probe. Figure 5.7 shows a real time movie still of a 170 T shot and Figure 5.8 demonstrates the integrity of the probe mounted inside the coil before and after the shot is fired.

For measurements in the STC, a pick-up coil mounted on a probe measures the magnetic field, as described in Section 3.3. Calibration of the pick-up coil is made by comparison to a standard coil that is accurately calibrated beforehand. For our CR measurements, the sensitivity of the standard coil with 3.7 mm^2 area is compared to the sensitivity of our probe's pick-up coil, resulting in a measured area of $\sim$ 1.35 mm^2 area. This area will be necessary for the data processing procedure described in Section 5.4. Figure 5.9 shows a typical field and dB/dt profile for our 35 kV, 2.3 MA shot, with a rise time of 2.44 μs to a maximum field of 175 T.

It should be mentioned here that the STC magnet system can also be utilized

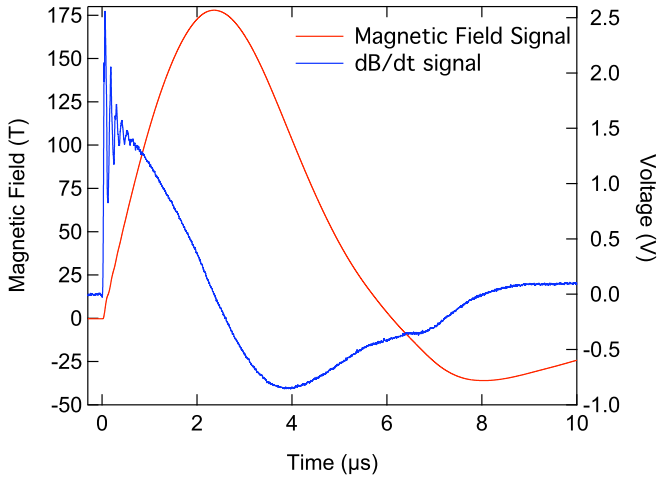

Figure 5.9 : Magnetic field and dB/dt profile for 35 kV, 175 T shot.

to access nondestructive pulsed fields up to 22 T. For such measurements, only two capacitor switches are connected instead of 24 switches, and it becomes necessary to enclose the coil inside a machined G-10 clamp that reinforces the coil from expanding outward during the shot. The G-10 clamp is an excellent solution that allows >100 consecutive low-field shots without compromising the integrity of the coil or requiring replacement of the coil.

5.3 CR optical setup

CO_2 lasers are the ideal radiation source for cyclotron resonance experiments in ultrahigh magnetic fields. At the NHMFL-Los Alamos, the continuous-wave, single-mode CO_2 laser source has an output power of ∼50 W and is tunable to many different wavelengths between 9.2 μm and 10.7 μm. To avoid damage to samples from heating by the laser, a 1:1.7 ZnSe wedge splitter reflects ∼24 W to a 50 Hz

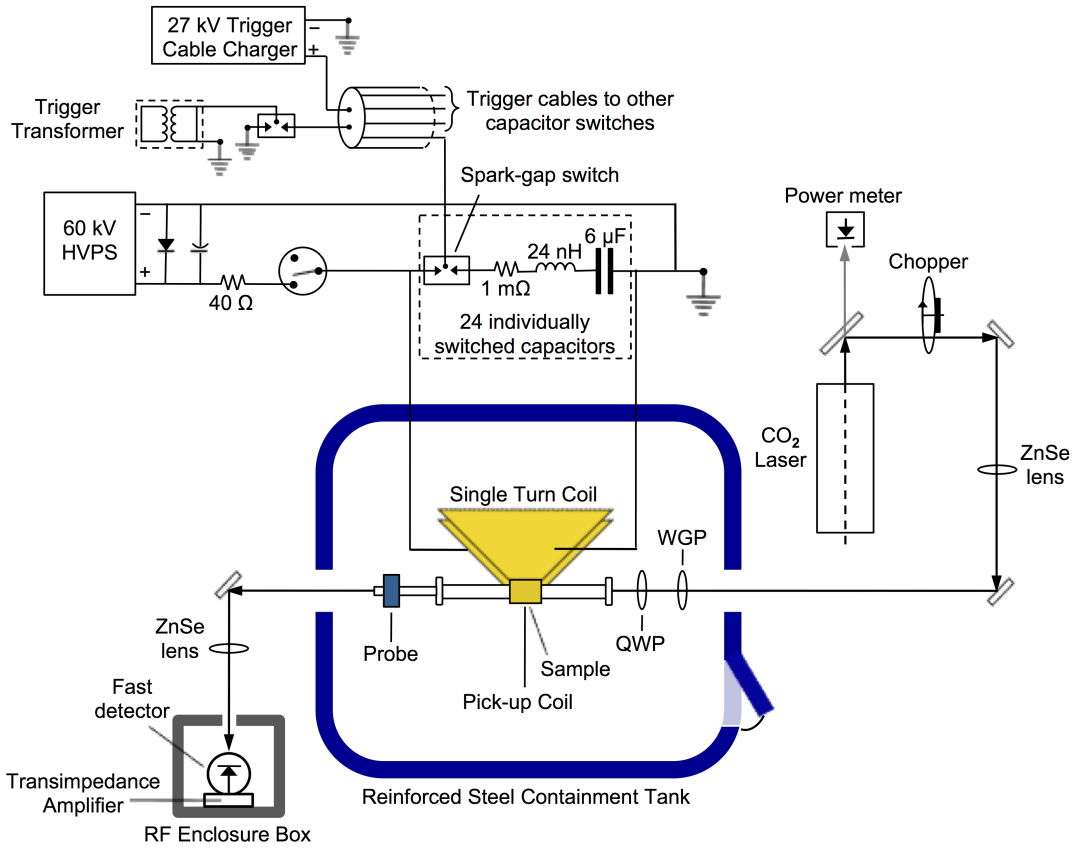

Figure 5.10 : Schematic of optical configuration for magneto-transmission in the NHMFL single-turn coil.

optical chopper with a duty cycle of 1%, which also plays an essential role in the triggering system for the STC (refer to Section 5.4). The remaining transmitted radiation through the wedge splitter is sent to a power meter for diagnostics of laser power stability. The optical schematic for magneto-tranmission in the NHMFL-STC is shown in Figure 5.10.

For magneto-optical measurements in the STC, in particular, CR experiments with smaller resonances that are difficult to resolve, and thus, improving the signal-to-noise ratio by increasing the detected signal and reducing the noise become very

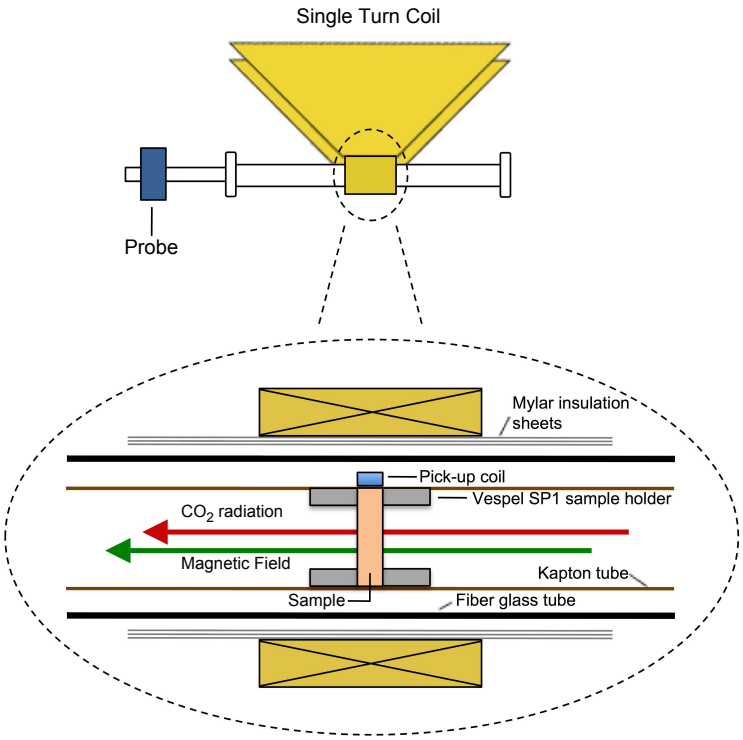

Figure 5.11 : Cross-sectional view of the optical probe with a Faraday configuration positioned inside the 10 mm single turn coil.

important. To improve the signal-to-noise ratio, care must be taken to overcome any difficulties arising from the limiting sample space inside the optical probe, as shown in Figure 5.11. With an inner diameter ranging between 2 mm and 4 mm available to focus the CO_2 light through the sample in the Faraday geometry (where light propagates parallel to the magnetic field), AR-coated ZnSe lenses are used to minimize reflection losses and to tightly focus the laser through the probe and into the detector. Figure 5.11 emphasizes a room-temperature probe for the purposes of our work. However, cryogenics can be incorporated into a continuous-flow cryostat probe for low temperature measurements in the STC [68].

For a Faraday configuration, the sample is placed inside a Vespel (unfilled polyimide-

based plastic) sample holder with a maximum aperture size of 4 mm for samples with a maximum diameter of 5 mm that can be accommodated in our optical probe. In addition to securely positioning the sample directly under the pick-up coil for accurate measurement of the magnetic flux density, the sample holder's smaller aperture size and choice of material attenuates any scattered laser that could bypass the sample and enter the detector. Therefore, taking into account the optical configuration and any beam divergence loss of the laser, the resulting laser power incident on the sample is $\sim$50 mW.

After passing the sample, the transmitted laser intensity is detected by a Kolmar Technologies mercury cadmium telluride (HgCdTe) detector with a spectral range of 2 - 11 μm. Coupled to a 30 MHz bandwidth low noise transimpedance amplifier that matches the impedance of the transient recorder and provides a 10^4 gain (refer to Section 5.4). This HgCdTe detector has $\sim$33 ns resolution, which corresponds to $\sim$1 - 2 T resolution in magnetic field. Both the detector and transimpedance amplifier are housed in a steel RF enclosure box to block any high frequency noise throughout the duration of the experiment.

For polarization-dependent CR measurements, the addition of a linear polarizer and quarter-wave plate before the sample converts linearly polarized CO_2 laser light to circularly polarized light (Figure 5.10). Figure 5.12 depicts the procedure for converting linearly polarized light to circularly polarized light. A ZnSe wire-grid polarizer transmits linearly polarized light to a net-zero order CdS quarter-wave plate with its fast (slow) axis oriented 45° to the linearly polarized axis. A second

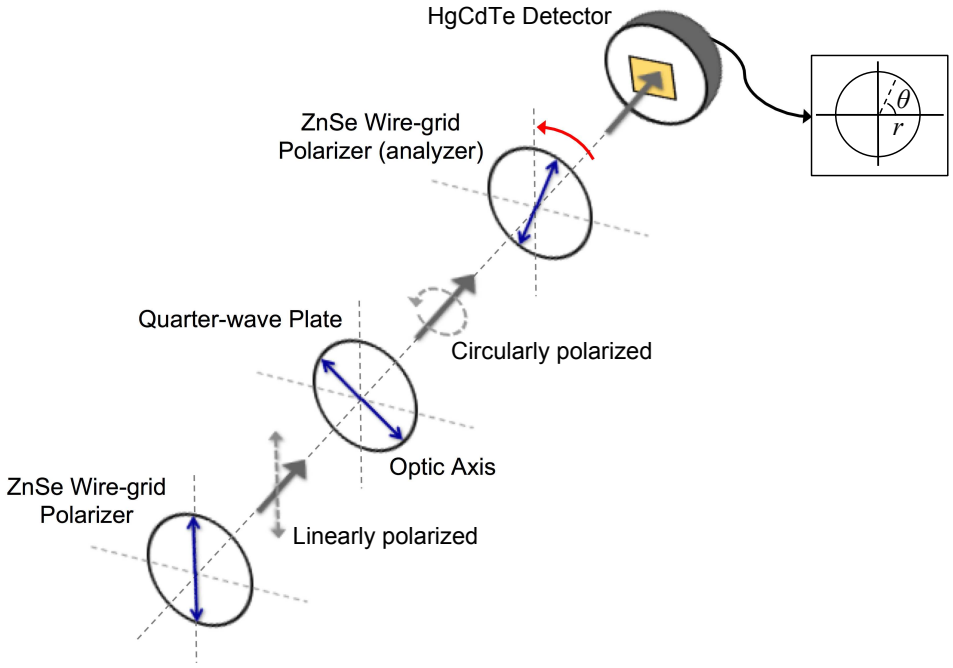

Figure 5.12 : Schematic of conversion from linear polarized light to circularly polarized light. WGP: wire-grid polarizer, QWP: quarter-wave plate.

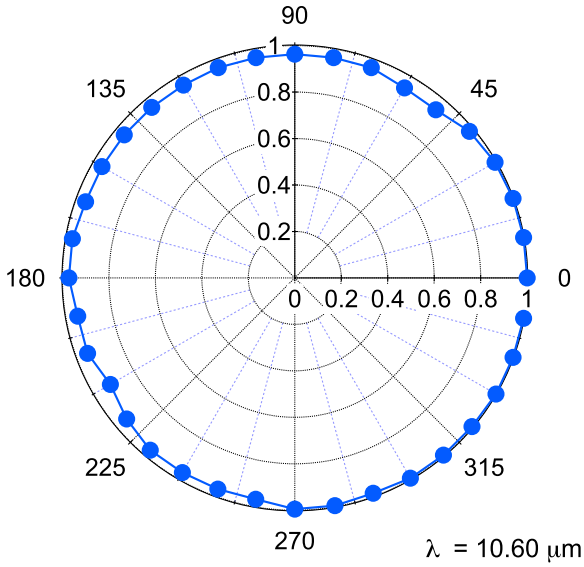

Figure 5.13 : Plot of ellipticity for a net-zero CdS quarter-wave plate at 10.6 μm. The output of the quarter-wave plate is circularly polarized.

ZnSe wire-grid polarizer is placed after the quarter-wave plate and behaves as an analyzer. As this wire-grid polarizer is rotated a full 360°, the transmitted laser intensity is detected with a HgCdTe detector. If the quarter-wave plate is oriented correctly for circularly polarized light, the detected intensity should not fluctuate as the second wire-grid polarizer is rotated. Figure 5.13 plots the ellipticity of our quarter-wave plate at 10.6 μm, showing a nearly perfect circular polarization.

5.4 Data acquisition and processing

We will now review the details for synchronization and operation of the STC magnet. Before operation of the STC, initial conditions must first be satisfied, with the coil carefully loaded and properly clamped with a 50-ton force and the CO_2 laser aligned through the sample and into the detector, as described in Sections 5.2-5.3. Once initial conditions are met, the correct timing sequence must be generated to synchronize the firing of the STC capacitors to the detection of magneto-transmission with a transient recorder. Figure 5.14 shows an extended one-line schematic describing all components necessary for triggering and firing the STC magnet.

In a grounded shielding room, we house our user-controlled trigger command that, when fired, sends a random initial fire command signal to a latch circuit that accepts input from both the user-controlled fire command and the chopper control. Once the latch circuit obtains the fire command signal, it waits for the condition of a second command, i.e., the rising edge of the chopper signal, and once both conditions are satisfied, the latch circuit generates a pulse output to a trigger delay

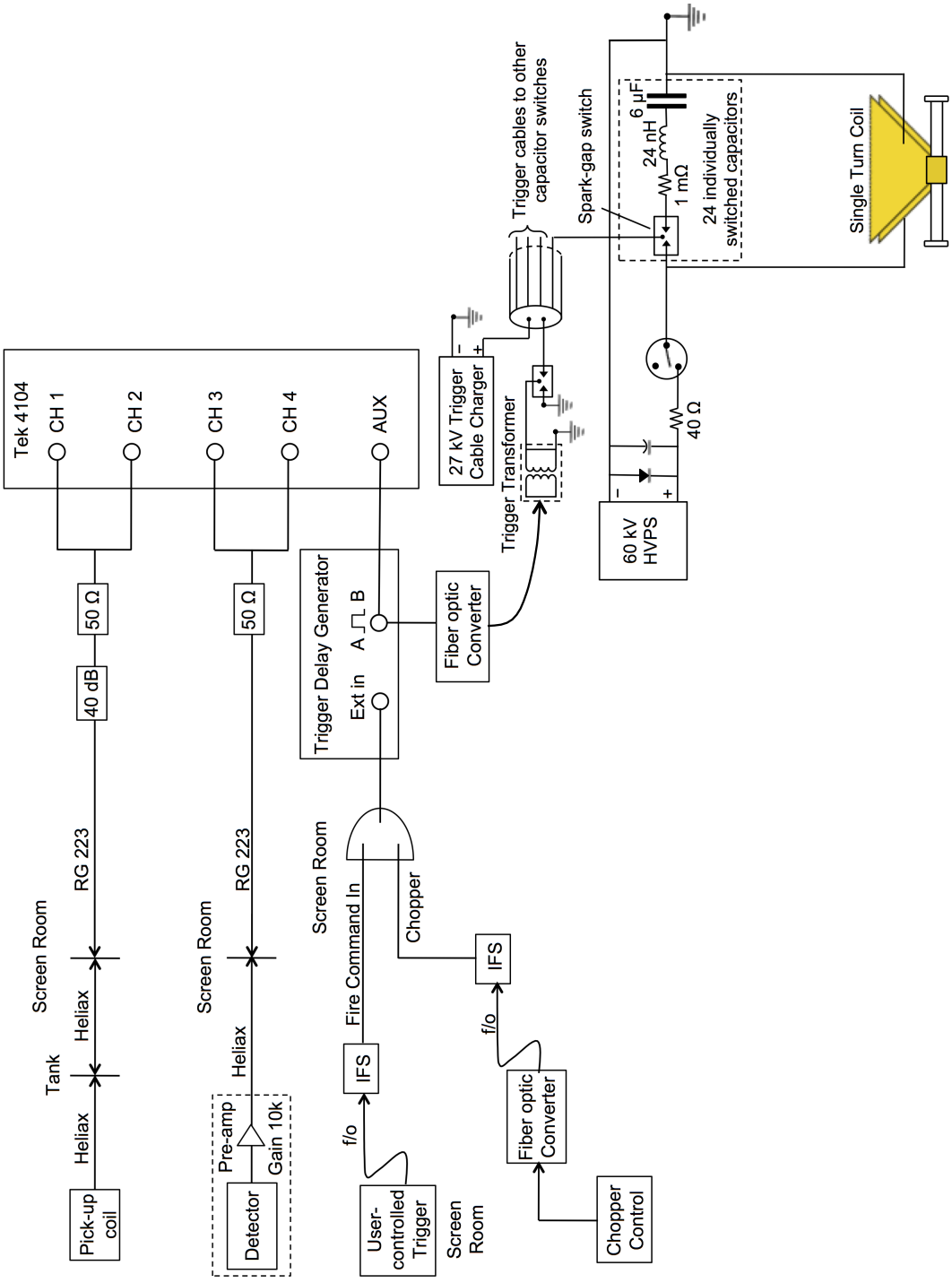

Figure 5.14 : Circuitry schematic of triggering system and operation of NHMFL STC magnet. f/o: fiber-optic cable, IFS: Integrated Fiber Systems (converts f/o to TTL signal).

generator (SRS DG535). The trigger delay generator allows us to accurately time the simultaneity of the signal from the detector to the firing of the 27 kV trigger generator system.

During pre-operation, with all high voltage power supplies off, this timing delay can be determined by unplugging the user-control trigger and using a flashlight that mimics the fire command in signal. The latch circuit waits for the "and" condition of our mimicked signal and the rising edge of the chopper signal. The trigger output pulse is sent to the trigger delay generator that fires the 27 kV trigger system. As this is pre-operation, our transient recorder simultaneously detects a burst of noise from the trigger system picked up by the pick-up coil in Channels 1 and 2, along with the transmitted laser intensity in Channels 3 and 4. Two channels with different voltage settings for both the pick-up coil signal and the detected laser intensity are used to ensure that all data is recorded without clipping or saturation of the data on the recorder. Any time delay between the detected noise and the laser signal is then adjusted via the trigger delay generator. This timing calibration is checked before every shot to ensure proper data acquisition of the voltage across the pick-up coil and the detected transmitted signal through the sample.

Once the correct timing delay is achieved, the transient recorder is triggered simultaneously with the firing of the 27 kV trigger generator system that fires the capacitor bank (refer to Section 5.2). Our transient recorder, a Tektronix DPO4104 oscilloscope with an 8-bit resolution and a 1-GHz sampling rate, reads out 10^6 data points. Figure 5.15(a) shows the raw signal and dB/dt trace for an 350 μm thick

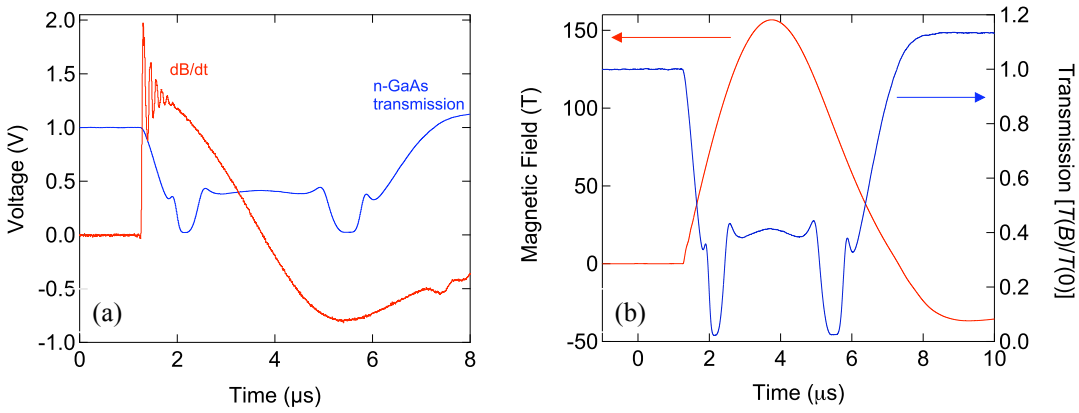

Figure 5.15 : (a) Raw signal and dB/dt trace read out from oscilloscope for n-GaAs sample. (b) Magneto-transmission and field profile in the time-domain for n-GaAs sample.

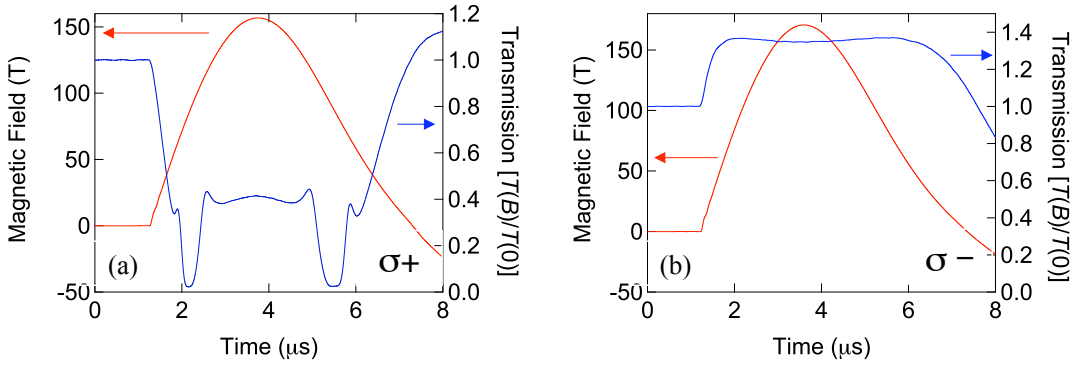

Figure 5.16 : (a) Electron-active CR for n-GaAs in the time-domain. (b) Hole-active CR for n-GaAs in the time-domain.

n-GaAs sample. Integrating the dB/dt trace and calibrating the field by

$$B = (100) \times \left(\frac{V_o}{A}\right) \times \left(\frac{50\ \Omega + R_B}{R_B}\right), \tag{5.1}$$

where ($\times 100$) accounts for the 40-dB attenuation, $A = 1.35$ mm^2 is the pick-up coil area, and $R_B = 4.0\ \Omega$ is the pick-up coil line resistance, we can now plot the magneto-transmission and the field profile in the time domain, as shown in Figure 5.15(b).

The goal of our measurements with n-GaAs was to determine the orientation of

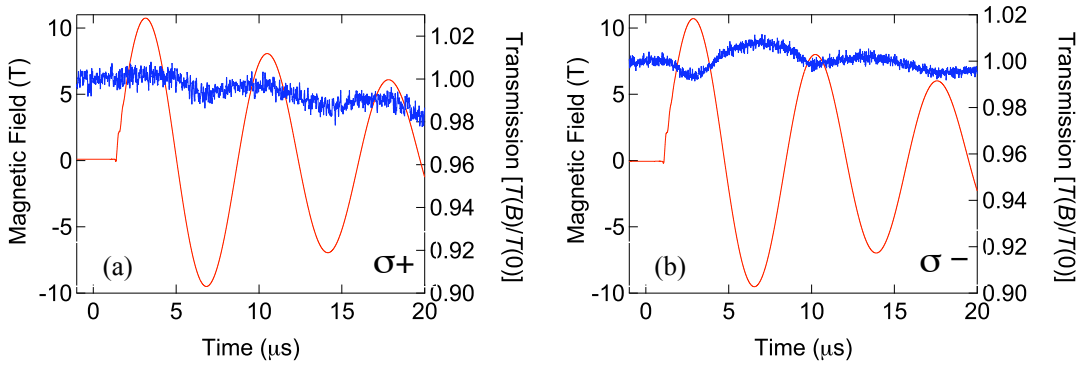

Figure 5.17 : Magneto-transmission of 10.67 μm light through a nominally-undoped CVD-grown graphene sample, during a 10 T magnet pulse. (a) Electron-active and (b) hole-active circular polarization are shown.

the quarter-wave plate (i.e., σ^+ or σ^-) such that we determine the correct orientation for electron-active CR or hole-active CR. Figure 5.16 compares electron-active and hole-active CR for n-GaAs. As is expected for n-GaAs, we only observe CR peaks for σ^+ orientation of the quarter-wave plate, which allows us to calibrate σ^+ as electron-active and σ^- as hole-active for our quarter-wave plate.

Extending this calibration to our work on graphene, we measured 10 T shots on nominally-undoped, CVD-grown graphene at room temperature with both σ^+ and σ^- orientations of the quarter-wave plate. Figure 5.17 shows our magneto-transmission results indicating that CVD-grown graphene is actually p-doped, where CR absorption peaks for positive peak fields (+10 T) occur with the hole-active orientation of the quarter-wave plate. In the next chapter, we fully describe results of circular polarization dependent CR measurements in graphene.

Chapter 6

Polarization-Dependent Cyclotron Resonance of Graphene at Ultrahigh Magnetic Fields

6.1 Polarization and Wavelength-dependence Results

Transmission measurements were performed at room temperature in the Faraday geometry using a continuous-wave, single-mode CO_2 laser that was tuned from 9.2 to 10.7 μm [89]. We utilized the combination of a linear polarizer and quarter-wave plate to switch between opposite circular polarizations (historically called "electron CR active" and "electron CR inactive"), and the transmission was detected with the mercury cadmium telluride detector sensitive in the 2-12 μm spectral range. The handedness of the circular polarization and direction of the magnetic field were cross-checked via electron CR of bulk n-type GaAs, as described in Section 5.3. Figure 6.1 reviews the experimental configuration we implemented with the STC magnet at the NHMFL-Los Alamos.

Figure 6.2 shows the magneto-transmission of both electron CR active and electron CR inactive circularly polarized light at 10.67 μm through a nominally-undoped graphene sample at room temperature. The magnetic field reaches a peak field of 170 T in less than 2.5 μs, with a total rise and fall time of $\sim$6 μs. Within this time duration, we observe clear CR absorption as transmission dips only for the

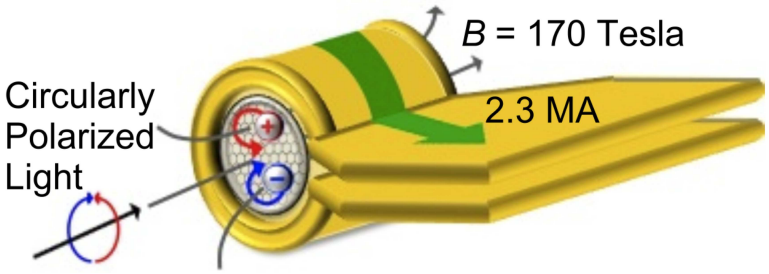

Figure 6.1 : (a) Experimental configuration for magneto-transmission using the STC magnet.

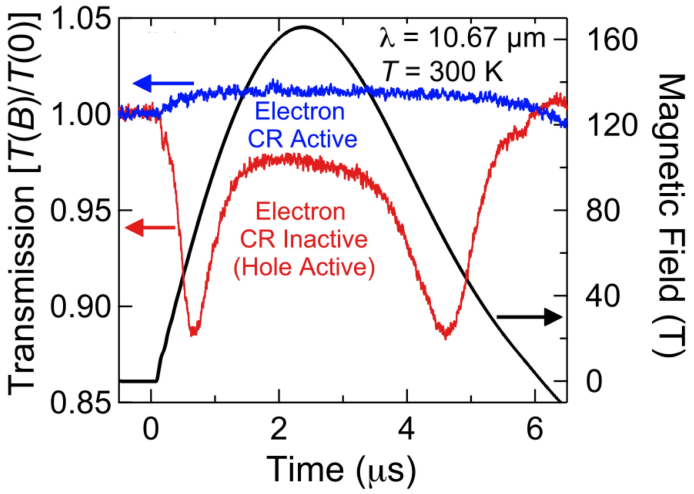

Figure 6.2 : Magneto-transmission of 10.67 μm light through a nominally-undoped CVD-grown graphene sample, during a 170 T magnet pulse. Data for both circular polarizations are shown. The pronounced CR absorption that appears for "electron CR *inactive*" polarization indicates that the graphene is p-type (hole doped).

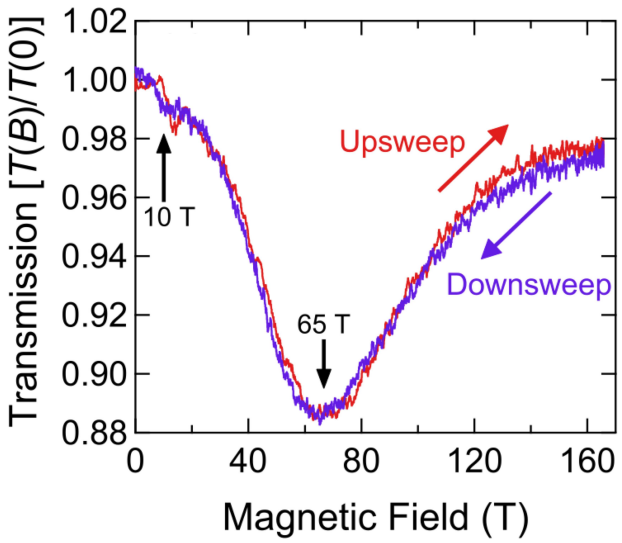

Figure 6.3 : Electron CR inactive transmission versus magnetic field shows two CR features at 10 T and 65 T, corresponding to $n = 0$ to $n = -1$ and $n = -1$ to $n = -2$ inter-LL transitions.

electron CR *inactive* polarization. Therefore, not only does this graphene sample have a nonzero density of charge carriers, these charge carriers are *holes*. This *p*-type doping is typical for as-grown, nominally-undoped graphene, most likely due to physisorption of molecules, such as H_2O and O_2, that causes the Fermi energy of undoped graphene to be shifted away from the Dirac point and into the valence band [93, 96].

The data actually reveal *two* CR features, one large absorption at ∼65 T and a smaller absorption at ∼10 T (see Fig. 6.3. We also notice the lack of any hysteresis of the transmission data between the upsweep and the downsweep of the magnetic field, which not only rules out any heating effects but also verifies the sufficient speed of the measurement system. From the linewidth of the larger CR feature, we can calculate the effective carrier scattering time, τ, to be ∼14 fs ($\omega_c\tau = B_c/\Delta B_c$), which

is typical for CVD-grown graphene [97].

Figure 6.4(a) compares magneto-transmission data using 9.22 and 10.67 μm radiation (134 and 116 meV photons, respectively). We again observe two CR absorptions for each wavelength, and we find that the resonance fields increase from 10 to 15 T and 65 to 80 T, respectively, with increasing photon energy. Using a Landau level fan diagram calculated for graphene, Fig. 6.4(b) shows the calculated $n = 0$ to $n = -1$ and $n = -1$ to $n = -2$ transitions at 9.22 μm (blue) and 10.67 μm (red). Comparing our measured CR features to the calculated inter-LL transition energies, we can assign the low-field (high-field) feature to the $n = 0$ to $n = -1$ ($n = -1$ to $n = -2$) transition.

Moreover, taking into account the measured integrated peak intensities from Fig. 6.4(a), we see a decrease in CR absorption with increasing photon energy due to a decrease in population of the $n = -1$ LL with increasing magnetic field. Because we do not observe any CR absorption corresponding to the $n = -2$ to $n = -3$ transition (expected at 103 and 135 T for these wavelengths, respectively), we can first conclude that the Fermi energy E_F must reside within the $n = -1$ LL at 65 T and must therefore have a zero-field value in the range between -140 to -400 meV. However, to more accurately determine the Fermi energy, we need to consider the degeneracy of each LL, which is $eB/2\pi\hbar$ ($\times$ 4 for valley and spin degeneracy), at the resonance fields 65 and 80 T. Calculating the ratio of the 65-T CR peak intensity to the 80-T CR peak intensity and using this ratio alongside the LL degeneracy, we can estimate the hole occupation within the $n = -1$ LL at 65 T and 80 T. We directly

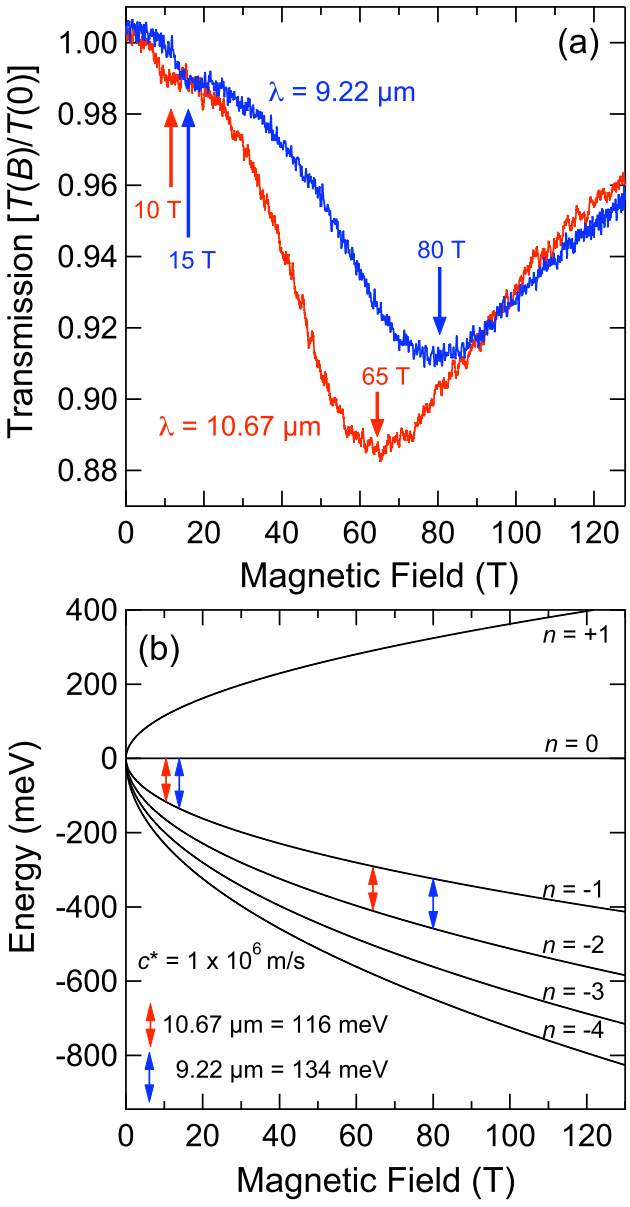

Figure 6.4 : (a) Wavelength-dependent electron-CR-inactive transmission traces versus magnetic field. Each trace exhibits two CR features (hole CR). (b) Landau level fan diagram with calculated LL transitions for 10.67 μm (red) and 9.22 μm (blue).

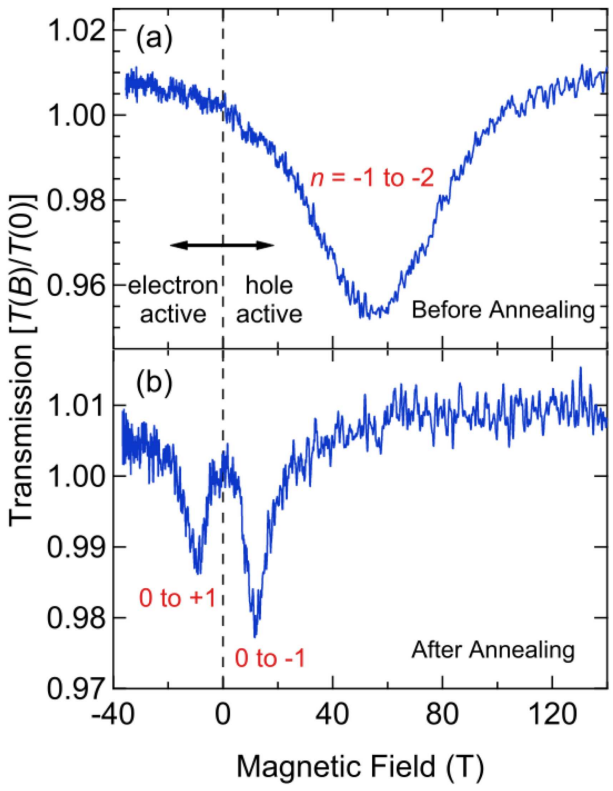

Figure 6.5 : (a) Electron CR inactive transmission at 10.6 μm before annealing, and (b) after annealing.

calculate the hole density of our sample, $n_h = 1.6 \times 10^{12}$ cm^{-2}, which translates to a zero-field Fermi energy, $E_F = \hbar v_F \sqrt{4\pi n_h} \approx -295$ meV.

6.2 Annealing Effects and the Magnetic Quantum Limit

This relatively large value of E_F that we obtained in Section 6.1 is due to accidental p-doping through physisorption of H_2O and O_2 and is typical for graphene but can be controlled if we can remove the physisorbed molecules. Figure 6.5 demonstrates that one can use thermal annealing to control the Fermi energy.

Here, we measured CR with electron CR inactive (that is, *hole* CR active)

polarization before annealing [Fig. 6.5(a)] and immediately after we annealed the sample for 2 hours at 150°C and 10^{-6} mbar to remove any physisorbed molecules [Fig. 6.5(b)]. As shown in Fig. 6.3(b), the majority of the doped holes are removed during the annealing process, and we now see two smaller CR peaks at +10 T and −10 T, corresponding to the $n = 0$ to $n = -1$ transition and the $n = 0$ to $n = +1$ transition, i.e., to hole *and* electron CR in the magnetic quantum limit. Note that, since the polarization is hole CR active for positive magnetic field, any resonance on the negative magnetic field side is due to electron CR (note that the field swings negative to about −40 T following a +170 T pulse, allowing both positive and negative fields to be examined in a single pulse). The emergence of the two 10 T peaks with opposite signs, and the absence of the ∼60 T peak (the $n = -1$ to $n = -2$ transition), unambiguously demonstrate that the Fermi energy now resides in the $n = 0$ LL — the magnetic quantum limit — at 10 T.

Furthermore, as the integrated hole CR absorption is stronger than the electron CR absorption [see Fig. 6.5(b)], the graphene sample is still slightly p-type and the intensity ratio between the two peaks provides information about the ratio of occupied versus unoccupied states within the $n = 0$ LL. More specifically, comparing the peak intensities, we calculate the ratio of occupied to unoccupied states within the $n = 0$ LL to be ∼1:1.5. We can then use this ratio and the LL degeneracy to calculate the hole density of our sample after annealing to be $n_h = 2.1 \times 10^{10}$ cm^{-2}. As a result, we can determine the zero-field Fermi energy after annealing to be $E_F = -34$ meV, again through $E_F = \hbar v_F \sqrt{4\pi n_h}$. Figure 6.6(a) shows the oscillations of the Fermi

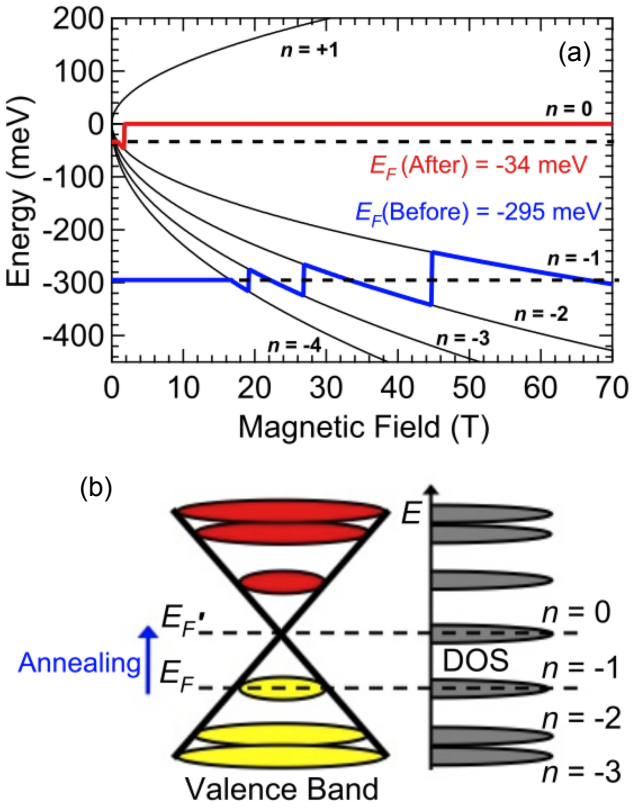

Figure 6.6 : (a) Landau fan diagram showing the Fermi energy oscillation with magnetic field for before (blue) and after (red) annealing, and (b) depicts that annealing moves the Fermi energy from −295 to −34 meV.

energy with increasing magnetic field for both before (blue) and after (red) annealing. As Fig. 6.6(b) depicts, before annealing the Fermi level sits within the $n = -1$ LL at 65 T and after annealing the Fermi energy now sits within the $n = 0$ LL at 10 T. The annealing process has successfully removed most of the physisorbed molecules that p-doped the graphene, leaving the system only slightly p-type. Qualitatively similar thermal effects were observed for other monolayer graphene samples that we investigated.

6.3 Discussion and Current Progress

We emphasize here that the simultaneous appearance of both hole *and* electron CR is an unusual phenomenon, made possible only via the unique electronic structure and Landau quantization of graphene. This phenomenon cannot occur in conventional materials containing only one carrier type. At $B = 0$, our graphene samples are still slightly p-type even after annealing, and they contain *only hole carriers*. However, as soon as a finite magnetic field is applied, a Landau level with exactly zero energy appears, i.e., the $n = 0$ Landau level (4-fold degenerate due to valley and spin). This level never moves with B in energy but simply grows in degeneracy. As long as the Fermi energy lies within this level, it is *partially filled*, containing both holes *and* electrons, allowing the observation of *both* electron and hole CR even at $T = 0$.

Detailed calculations confirm these results. In Section 4.3 of this thesis dissertation, we compute the CR absorption for both electron-active and hole-active circular polarizations. The results are given by Eqs. (4.49) and (4.53). The results show a

number of interesting and unusual features that we have discussed: i) The optical field Hamiltonian for graphene comes in through an $\boldsymbol{A} \cdot \boldsymbol{\sigma}$ term rather than the usual term $\mathbf{A} \cdot \mathbf{p}$; ii) the expressions show that even an *undoped* sample will show CR in contrast to conventional semiconductors where the sample must be doped; iii) if the Fermi energy lies in the $n = 0$ level, then CR is present for *both* electron-active and hole-active circular polarizations; and iv) if the Fermi level lies in the $n = 0$ level, the ratio of CR absorption between the electron-active and hole-active peaks allows one to accurately determine the Fermi level and carrier density.

In summary, we have measured cyclotron resonance in graphene at ultrahigh magnetic fields. From polarization and wavelength dependent measurements, we have shown unintentional chemical doping is strongly p-type by observing the $n = 0$ to $n = -1$ and $n = -1$ to $n = -2$ transitions in nominally-undoped graphene. Additionally, we demonstrated that annealing effectively removes p-doping from graphene, shifting the Fermi energy much closer to the Dirac point. This shift completely blocked the $n = -1$ to $n = -2$ hole cyclotron resonance transition and revealed the $n = 0$ to $n = +1$ electron cyclotron resonance transition. As a result, due to graphene's unique band structure, we simultaneously observed both hole and electron cyclotron resonance in the magnetic quantum limit, even with a p-type graphene sample. These high-field studies therefore allow for a clear identification of cyclotron resonance features in large-area graphene samples, and an accurate determination of their low carrier mobilities and fast scattering times.

Additional work on IR studies of graphene at ultra-high magnetic fields have

been extended to include the wavelength dependence of monolayer graphene in the magnetic quantum limit and on Bernal-stacked bilayer graphene. We will only briefly review the results of our current work for the scope of this thesis.

Similar sample preparation for both monolayer and bilayer graphene provided by the Tour group was implemented, as discussed in Section 5.1. However, we transferred the graphene samples to zinc selenide substrates instead of KRS-5 substrates, which is also transparent at mid-infrared wavelengths. Figure 6.7 shows the wavelength dependence of graphene after annealing the sample to remove any physisorbed molecules. We first note that we again observe both hole CR and electron CR for all three wavelengths, which further supports our work presented in this thesis dissertation. Secondly, we similarly observe the resonance fields increase with increasing photon energy and emphasize that the peak field positions are correctly assigned to the $n = 0$ to $n = -1$ transition and the $n = 0$ to $n = +1$ transition, i.e., to hole *and* electron CR in the magnetic quantum limit. We are now investigating the effects of wavelength dependence on the ratio of occupied to unoccupied states within the $n = 0$ LL.

Figure 6.8 shows our current work on bilayer graphene, before (top) and after (bottom) annealing. Unlike with monolayer graphene, we do not observe any obvious changes in the magneto-transmission with annealing, which we suspect is from the difficulty of annealing bilayer graphene to remove physisorbed molecules. We are currently analyzing the CR peaks to assign their corresponding LL transition.

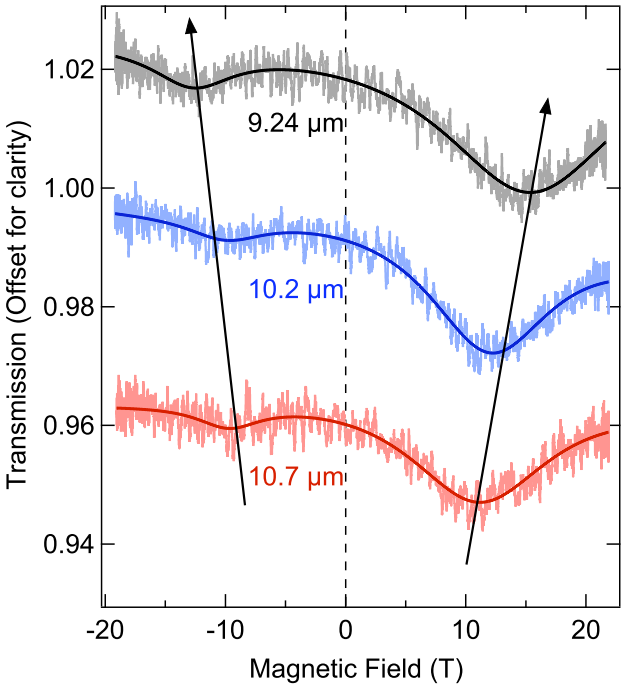

Figure 6.7 : Wavelength dependence of graphene after annealing.

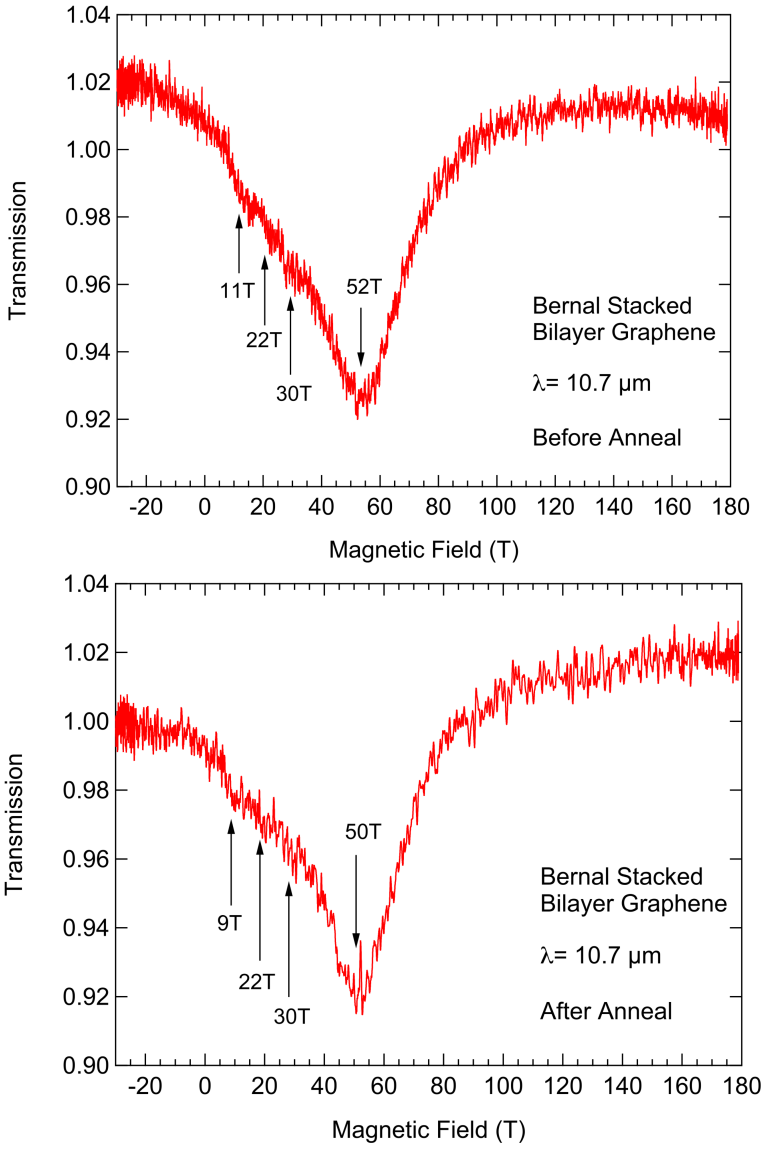

Figure 6.8 : Bernal-stacked bilayer graphene. (top) Electron CR inactive transmission at 10.6μm before annealing and (bottom) after annealing.

Chapter 7

Conclusion

In this thesis dissertation, we successfully measured CR in graphene at ultra-high magnetic fields with the single-turn coil technique. Circularly-polarized magneto-transmission of CO_2 laser light revealed a strong and unintentional p-type (hole) doping of these nominally-undoped graphene samples. A small CR feature at 10 T and a larger CR feature at 65 T corresponds to the $n = 0$ to $n = -1$ and $n = -1$ to $n = -2$ inter-LL transitions, respectively. Wavelength-dependent magneto-transmission data show a good agreement with calculated LL transitions, allowing the Fermi energy (E_F) of the sample to be determined (-295 meV). Moreover, we found that annealing the graphene samples in vacuum to remove physisorbed molecules shifts the Fermi energy markedly closer to the Dirac point ($E_F = -34$ meV). Due to graphene's unique Landau level structure, we show that in the magnetic quantum limit this allows both hole ($n = 0$ to $n = -1$) *and* electron ($n = 0$ to $n = +1$) CR to be observed *simultaneously*, even though the sample is still p-type. All of our experimental results were confirmed through our calculation of cyclotron resonance and interband magneto-absorption for graphene presented in Chapter 4. Finally, from our work presented, we confirm that high-field studies provide a powerful technique to clearly identify cyclotron resonance features in large-area graphene samples and to accurately determine their low carrier mobilities and fast scattering times, which

are important experimental parameters to understand for technologically important applications requiring large-area graphene films.

Bibliography

[1] P. R. Wallace, "The Band Theory of Graphite," Phys. Rev. **71**, 622 (1947).

[2] M. L. Sadowski, G. Martinez, M. Potemski, C. Berger, and W. A. de Heer, "Landau Level Spectroscopy of Ultrathin Graphite Layers," Phys. Rev. Lett. **97**, 266405 (2006).

[3] K. S. Novoselov, A. K. Geim, S. V. Morozov, D. Jiang, M. I. Katsnelson, I. V. Grigorieva, S. V. Dubonos, and A. A. Firsov, "Two-dimensional gas of massless Dirac fermions in graphene," Nature **438**, 197 (2005).

[4] Y. Zhang, Y.-W. Tan, H. L. Stormer, and P. Kim, "Experimental observation of the quantum Hall effect and Berry's phase in graphene," Nature **438**, 201 (2005).

[5] M. I. Katsnelson, K. S. Novoselov, and A. K. Geim, "Chiral tunnelling and the Klein paradox in graphene," Nat. Phys. **2**, 620 (2006).

[6] Y. Zhang, Z. Jiang, J. P. Small, M. S. Purewal, Y.-W. Tan, M. Fazlollahi, J. D. Chudow, J. A. Jaszczak, H. L. Stormer, and P. Kim, "Landau-Level Splitting in Graphene in High Magnetic Fields," Phys. Rev. Lett. **96**, 136806 (2006).

[7] Y. Zheng and T. Ando, "Hall conductivity of a two-dimensional graphite sys-

tem," Phys. Rev. B **65**, 245420 (2002).

[8] V. P. Gusynin and S. G. Sharapov, "Unconventional Integer Quantum Hall Effect in Graphene," Phys. Rev. Lett. **95**, 146801 (2005).

[9] N. M. R. Peres, F. Guinea, and A. H. Castro Neto, "Electronic properties of disordered two-dimensional carbon," Phys. Rev. B **73**, 125411 (2006).

[10] S. G. Sharapov, V. P. Gusynin, and H. Beck, "Magnetic oscillations in planar systems with the Dirac-like spectrum of quasiparticle excitations," Phys. Rev. B **69**, 075104 (2004).

[11] Y. Shkolnikov, S. Misra, N. Bishop, E. D. Poortere, and M. Shayegan, "Observation of Quantum Hall "Valley Skyrmions"," Phys. Rev. Lett. **95**, 066809 (2005).

[12] Y. Iye and G. Dresselhaus, "Non-Ohmic Transport in the Magnetic-Field-Induced Charge-Density-Wave Phase of Graphite," Phys. Rev. Lett. **54**, 1182 (1985).

[13] D. V. Khveshchenko, "Magnetic-Field-Induced Insulating Behavior in Highly Oriented Pyrolitic Graphite," Phys. Rev. Lett. **87**, 206401 (2001).

[14] T. Ando, Y. Zheng, and H. Suzuura, "Dynamical Conductivity and Zero-Mode Anomaly in Honeycomb Lattices," J. Phys. Soc. Jpn. **71**, 1318 (2002).

[15] V. P. Gusynin and S. G. Sharapov, "Transport of Dirac quasiparticles in graphene: Hall and optical conductivities," Phys. Rev. B **73**, 245411 (2006).

[16] V. P. Gusynin, S. G. Sharapov, and J. P. Carbotte, "Unusual Microwave Response of Dirac Quasiparticles in Graphene," Phys. Rev. Lett. **96**, 256802 (2006).

[17] A. Iyengar, J. Wang, H. A. Fertig, and L. Brey, "Excitations from filled Landau levels in graphene," Phys. Rev. B **75**, 125430 (2007).

[18] D. S. L. Abergel and V. I. Fal'ko, "Optical and magneto-optical far-infrared properties of bilayer graphene," Phys. Rev. B **75**, 155430 (2007).

[19] J. Milton Pereira, F. M. Peeters, and P. Vasilopoulos, "Landau levels and oscillator strength in a biased bilayer of graphene," Phys. Rev. B **76**, 115419 (2007).

[20] V. P. Gusynin, S. G. Sharapov, and J. P. Carbotte, "Anomalous Absorption Line in the Magneto-Optical Response of Graphene," Phys. Rev. Lett. **98**, 157402 (2007).

[21] M. Koshino and T. Ando, "Magneto-optical properties of multilayer graphene," Phys. Rev. B **77**, 115313 (2008).

[22] Y. Barlas, R. Côté, K. Nomura, and A. H. MacDonald, "Intra-Landau-Level Cyclotron Resonance in Bilayer Graphene," Phys. Rev. Lett. **101**, 097601 (2008).

[23] S. A. Mikhailov, "Nonlinear cyclotron resonance of a massless quasiparticle in graphene," Phys. Rev. B **79**, 241309 (2009).

[24] Z. Jiang, E. A. Henriksen, L. C. Tung, Y.-J. Wang, M. E. Schwartz, M. Y. Han, P. Kim, and H. L. Stormer, "Infrared Spectroscopy of Landau Levels of

Graphene," Phys. Rev. Lett. **98**, 197403 (2007).

[25] R. S. Deacon, K.-C. Chuang, R. J. Nicholas, K. S. Novoselov, and A. K. Geim, "Cyclotron resonance study of the electron and hole velocity in graphene monolayers," Phys. Rev. B **76**, 081406 (2007).

[26] W. Kohn, "Cyclotron Resonance and de Haas-van Alphen Oscillations of an Interacting Electron Gas," Phys. Rev. **123**, 1242 (1961).

[27] N. Miura, *Physics of Semiconductors in High Magnetic Fields* (Oxford University Press, New York, 2008), chap. Cyclotron Resonance and Far-Infrared Spectroscopy.

[28] M. Besson, E. Gornik, C. M. Engelhardt, and G. Weimann, "Cyclotron resonance of electrons in the Wigner solid regime," Semicond. Sci. and Technol. **7**, 1274 (1992).

[29] G. M. Summers, R. J. Warburton, J. G. Michels, R. J. Nicholas, J. J. Harris, and C. T. Foxon, "New phases of the 2D electron system in the ultra-quantum limit observed by cyclotron resonances," Phys. Rev. Lett. **70**, 2150 (1993).

[30] N. R. Cooper and J. T. Chalker, "Theory of spin-split cyclotron resonance in the extreme quantum limit," Phys. Rev. Lett. **72**, 2057 (1994).

[31] K. Asano and T. Ando, "Effects of Electron-Electron Interactions on Spin-Split Cyclotron Resonance," J. Phys. Soc. Jpn. **65**, 1191 (1996).

[32] I. Crassee, J. Levallois, A. L. Walter, M. Ostler, A. Bostwick, E. Rotenberg, T. Seyller, D. van der Marel, and A. B. Kuzmenko, "Giant Faraday rotation in single- and multilayer graphene," Nat. Phys. **7**, 48 (2010).

[33] I. Crassee, J. Levallois, D. van der Marel, A. L. Walter, T. Seyller, and A. B. Kuzmenko, "Multicomponent magneto-optical conductivity of multilayer graphene on SiC," Phys. Rev. B **84**, 035103 (2011).

[34] E. A. Henriksen, Z. Jiang, L.-C. Tung, M. E. Schwartz, M. Takita, Y.-J. Wang, P. Kim, and H. L. Stormer, "Cyclotron Resonance in Bilayer Graphene," Phys. Rev. Lett. **100**, 087403 (2008).

[35] E. A. Henriksen, P. Cadden-Zimansky, Z. Jiang, Z. Q. Li, L.-C. Tung, M. E. Schwartz, M. Takita, Y.-J. Wang, P. Kim, and H. L. Stormer, "Interaction-Induced Shift of the Cyclotron Resonance of Graphene Using Infrared Spectroscopy," Phys. Rev. Lett. **104**, 067404 (2010).

[36] P. Neugebauer, M. Orlita, C. Faugeras, A.-L. Barra, and M. Potemski, "How Perfect Can Graphene Be?" Phys. Rev. Lett. **103**, 136403 (2009).

[37] M. Orlita, C. Faugeras, P. Plochocka, P. Neugebauer, G. Martinez, D. K. Maude, A.-L. Barra, M. Sprinkle, C. Berger, W. A. de Heer, and M. Potemski, "Approaching the Dirac Point in High-Mobility Multilayer Epitaxial Graphene," Phys. Rev. Lett. **101**, 267601 (2008).

[38] M. Orlita, C. Faugeras, R. Grill, A. Wysmolek, W. Strupinski, C. Berger, W. A.

de Heer, G. Martinez, and M. Potemski, "Carrier Scattering from Dynamical Magnetoconductivity in Quasineutral Epitaxial Graphene," Phys. Rev. Lett. **107**, 216603 (2011).

[39] A. M. Witowski, M. Orlita, R. Stępniewski, A. Wysmolek, J. M. Baranowski, W. Strupiński, C. Faugeras, G. Martinez, and M. Potemski, "Quasiclassical cyclotron resonance of Dirac fermions in highly doped graphene," Phys. Rev. B **82**, 165305 (2010).

[40] J. Kono, "Cyclotron Resonance," in *Methods in Materials Research* (Wiley, New York, 2001), p. Unit 9b.2.

[41] J. Kono and N. Miura, "Cyclotron Resonance in High Magnetic Fields," in *High Magnetic Fields: Science and Technology Vol. 3* (World Scientific, 2006), pp. 61–90.

[42] N. Miura, *Physics of Semiconductors in High Magnetic Fields* (Oxford University Press, New York, 2008), chap. Electronic States in High Magnetic Fields.

[43] R. G. Takwale and P. S. Puranik, *Introduction to Classical Mechanics* (Tata McGraw-Hill Education, New Delhi, 1980).

[44] C. Cohen-Tannoudji, B. Diu, and F. Laloe, *Quantum Mechanics Vol. 2* (John Wiley & Sons Ltd., Singapore, 2005).

[45] L. D. Landau and E. M. Lifshitz, *Quantum mechanics: non-relativistic theory*, vol. 3 of *Course of Theoretical Physics* (Butterworth-Heinemann, Oxford, 1977).

[46] J. Singleton, *Band Theory and Electronic Properties of Solids* (Oxford University Press, New York, 2001).

[47] S. Blundell, *Magnetism in Condensed Matter* (Oxford University Press, New York, 2001).

[48] N. W. Ashcroft and N. D. Mermin, *Solid State Physics* (Holt, Rhinehart, and Winston, New York, 1976).

[49] P. Y. Yu and M. Cardona, *Fundamentals of Semiconductors: Physics And Materials Properties*, Advanced texts in physics (Springer, Berlin, 2005).

[50] J. Kono, *Ultra-high Field Cyclotron Resonance in Low Mobility Semiconductors*, Master's thesis, University of Tokyo (1992).

[51] H. J. Schneider-Muntau and Y. Nakagawa, "Steady State Resistive and Hybrid Magnets," in *High Magnetic Fields: Science and Technology. Vol 1, Magnet Technology and Experimental Techniques*, edited by F. Herlach and N. Miura (World Scientific, Singapore, 2003).

[52] American Magnetics Inc., Accessed on 9 February 2012, *Characteristics of Superconducting Magnets* (http://www.americanmagnetics.com/charactr.php).

[53] K. Coyne, *Magnets from Mini to Mighty*, Accessed on 9 February 2012 (http://www.magnet.fsu.edu/education/tutorials/magnetacademy/ magnets/fullarticle.html).

[54] H. Jones, "Superconducting Magnets," in *High Magnetic Fields: Science and Technology. Vol 1, Magnet Technology and Experimental Techniques*, edited by F. Herlach and N. Miura (World Scientific, Singapore, 2003).

[55] National Institute for Materials Science, Accessed on 9 February 2012, *Superconducting Magnet Generates World's Highest Magnetic Field at 24T* (http://www.nims.go.jp/eng/news/press/2011/09/p201109070.html).

[56] F. Bitter, "The Design of Powerful Electromagnets Part I. The Use of Iron," Rev. Sci. Instrum. **7**, 479 (1936).

[57] F. Bitter, "The Design of Powerful Electromagnets Part II. The Magnetizing Coil," Rev. Sci. Instrum. **7**, 482 (1936).

[58] F. Bitter, "The Design of Powerful Electromagnets Part III. The Use of Iron," Rev. Sci. Instrum. **8**, 318 (1937).

[59] F. Bitter, "The Design of Powerful Electromagnets Part IV. The New Magnet Laboratory at M. I. T." Rev. Sci. Instrum. **10**, 373 (1939).

[60] F. Herlach and N. Miura, "Introduction with Survey of Magnet Laboratories," in *High Magnetic Fields: Science and Technology. Vol 1, Magnet Technology and Experimental Techniques*, edited by F. Herlach and N. Miura (World Scientific, Singapore, 2003).

[61] B. D. Cullity and C. D. Graham, *Introduction to Magnetic Materials* (John Wiley & Sons Ltd, Hoboken, New Jersey, 2009).

[62] National High Magnetic Field Laboratory, Accessed on 9 February 2012, *Mag Lab Reclaims World Record for Highest Field Resistive Magnet* (http://www.magnet.fsu.edu/mediacenter/news/pressreleases/2010/2010january-36t.html).

[63] M. Bird, "Resistive magnet technology for hybrid inserts," Superconductor Science and Technology **17**, R19 (2004).

[64] F. Herlach and N. Miura, "Nondestructive Compact Pulsed Magnets," in *High Magnetic Fields: Science and Technology. Vol 1, Magnet Technology and Experimental Techniques*, edited by F. Herlach and N. Miura (World Scientific, Singapore, 2003).

[65] S. Hansel, *Hysteresis in Optical Megagauss Spectroscopy*, Ph.D. thesis, Humboldt-Universitat zu Berlin (2006).

[66] M. Barczewski, *The Single-Turn Coil Technique: Installation and Application to IR Magnetospectroscopy on HgSe:Fe Layer Structures*, Ph.D. thesis, Humboldt-Universitat zu Berlin (1999).

[67] F. Herlach, R. Boegarts, J. Vanacken, and L. V. Bockstal, "Long duration pulsed magnetic fields: Achievements and challenges," Physica B **201**, 5 (1994).

[68] N. Miura, *Physics of Semiconductors in High Magnetic Fields* (Oxford University Press, New York, 2008), chap. Experimental Techniques for High Magnetic Fields.

[69] S. Foner, "68.4-T-long pulse magnet: Test of high strength microcomposite Cu/Nb conductor," Appl. Phys. Lett. **49**, 982 (1986).

[70] Y. Sakai, K. Inoue, T. Asano, H. Wada, and H. Maeda, "Development of high-strength, high-conductivity Cu-Ag alloys for high-field pulsed magnet use," Appl. Phys. Lett. **59**, 2965 (1991).

[71] K. Kindo, "100T magnet developed in Osaka," Physica B **294**, 585 (2001).

[72] F. Herlach, R. Bogaerts, I. Deckers, G. Heremans, L. Li, G. Pitsi, J. Vanacken, L. V. Bockstal, and A. V. Esch, "The K.U. Leuven pulsed high magnetic field facility," Physica B **201**, 542 (1994).

[73] M. Motokawa, H. Nojiri, and Y. Tokunaga, "An idea for the easy construction of a high field magnet," Physica B **155**, 96 (1989).

[74] S. Takeyama, H. Ochimizu, S. Sasaki, and N. Miura, "55 T long pulse magnet reinforced by ice and woven-glass cloths," Measurement Science and Technology **3**, 662 (1992).

[75] K. Rosseel, A. Lagutin, F. Herlach, W. Boon, Y. Bruynseraede, and J. V. Humbeeck, "Magnet and wire technology at the K.U.Leuven Pulsed Field laboratory," IEEE Transactions on Applied Superconductivity **12**, 707 (2002).

[76] G. S. Boebinger, A. H. Lacerda, H. J. Schneider-Muntau, and N. Sullivan, "The National High Magnetic Field Laboratory's pulsed magnetic field facility in Los Alamos," Physica B **294**, 512 (2001).

[77] L. J. Campbell and J. B. Schillig, "Controlled Waveform Magnets," in *High Magnetic Fields: Science and Technology. Vol 1, Magnet Technology and Experimental Techniques*, edited by F. Herlach and N. Miura (World Scientific, Singapore, 2003).

[78] C.H. Mielke, *Private Communication* (2012).

[79] N. Miura and F. Herlach, "Generation of Megagauss Fields," in *High Magnetic Fields: Science and Technology. Vol 1, Magnet Technology and Experimental Techniques*, edited by F. Herlach and N. Miura (World Scientific, Singapore, 2003).

[80] F. Herlach, H. Knoepfel, and R. Luppi, *Proc. Conf. on Megagauss Magnetic Field Generation by Explosives and Related Experiments*, Frescati, Italy, EURATOM, Brussels p. 287 (1966).

[81] A. I. Pavlovskii, *Megagauss Fields and Pulsed Power Systems- Proc. 5th Int. Conf. on Megagauss Magnetic FIeld Generation and Related Topics*, Novosibirsk, Russia p. 139 (1989).

[82] V. Titov and G. Shvetsov, *Megagauss Fields and Pulsed Power Systems- Proc. 5th Int. Conf. on Megagauss Magnetic FIeld Generation and Related Topics*, Novosibirsk, Russia p. 139 (1989).

[83] N. Miura, T. Goto, K. Nakao, S. Takeyama, T. Sakakibara, T. Haruyama, and T. Kikuchi, "Production of Ultra-high Magnetic FIelds and their Applications

to Solid State Physics," Physica B **155**, 23 (1989).

[84] Y. H. Matsuda, F. Herlach, S. Ikeda, and N. Miura, "Generation of 600 T by electromagnetic flux compression with improved implosion symmetry," Rev. Sci. Instrum. **73**, 4288 (2002).

[85] A. Jorio, M. S. Dresselhaus, R. Saito, and G. Dresselhaus, *Raman Spectroscopy in Graphene Related Systems* (Wiley-VCH Verlag GmbH & Co. KGaA, Singapore, 2011).

[86] R. Saito, G. Dresselhaus, and M. S. Dresselhaus, *Physical properties of carbon nanotubes* (World Scientific, Singapore, 2003).

[87] M. Orlita and M. Potemski, "Dirac electronic states in graphene systems: optical spectroscopy studies," Semicond. Sci. and Technol. **25**, 063001 (2010).

[88] Z. Lenarcic, "Landau Levels in Graphene," Seminar paper at Univeristy of Ljubljani, Slovenia (December 2010).

[89] L. G. Booshehri, C. H. Mielke, D. G. Rickel, S. A. Crooker, Q. Zhang, L. Ren, E. H. Hároz, A. Rustagi, C. J. Stanton, Z. Jin, Z. Sun, Z. Yan, J. M. Tour, and J. Kono, "Circular-Polarization Dependent Cyclotron Resonance in Large-Area Graphene in Ultrahigh Magnetic Fields," Phys. Rev. B p. in press (2012).

[90] L. M. Roth, B. Lax, and S. Zwerdling, "Theory of Optical Magneto-Absorption Effects in Semiconductors," Phys. Rev. **114**, 90 (1959).

[91] S. L. Chuang, *Physics of Optoelectronic Devices* (Wiley, New York, 1995).

[92] N. H. Shon and T. Ando, "Quantum Transport in Two-Dimensional Graphite System," J. Phys. Soc. Jpn. **67**, 2421 (1998).

[93] Z. Jin, J. Yao, C. Kittrell, and J. M. Tour, "Large-Scale Growth and Characterizations of Nitrogen-Doped Monolayer Graphene Sheets," ACS Nano **5**, 4112 (2011).

[94] C. H. Mielke and R. D. McDonald, "Single Turn Multi-Megagauss System at the NHMFL-LOS Alamos to study plutonium," in *2006 IEEE International Conference on Megagauss Magnetic Field Generation and Related Topics* (2006), vol. 5, pp. 227–231.

[95] C. H. Mielke and B. Mircea, "Experimental and Numerical Studies of Megagauss Magnetic-Field Generation at LANL-NHMFL," IEEE Transactions on Plasma Science **38**, 1739 (2010).

[96] F. Schedin, A. K. Geim, S. V. Morozov, E. W. Hill, P. Blake, M. I. Katsnelson, and K. S. Novoselov, "Detection of individual gas molecules adsorbed on graphene," Nat. Mater. **6**, 652 (2007).

[97] Y.-W. Tan, Y. Zhang, K. Bolotin, Y. Zhao, S. Adam, E. H. Hwang, S. D. Sarma, H. L. Stormer, and P. Kim, "Measurement of Scattering Rate and Minimum Conductivity in Graphene," Phys. Rev. Lett. **99**, 246803 (2007).